

ISSN 0973-3302

THE JOURNAL OF ACOUSTICAL SOCIETY OF INDIA

Volume 46

Number 3-4

July-December 2019



A Quarterly Publication of the ASI
<https://acoustics.org.in>



ASI

The Journal of Acoustical Society of India

The Refereed Journal of the Acoustical Society of India (JASI)

CHIEF EDITOR:

B. Chakraborty

CSIR-National Institute of Oceanography

Dona Paula,

Goa-403 004

Tel: +91.832.2450.318

Fax: +91.832.2450.602

E-mail: bishwajit@nio.org

ASSOCIATE SCIENTIFIC EDITOR:

A R Mohanty

Mechanical Engg. Department

Indian Institute of Technology

Kharagpur-721302, India

Tel. : +91-3222-282944

E-mail : amohantyemch.iitkgp.ernet.in

Editorial Office:

MANAGING EDITOR

Mahavir Singh

ASSISTANT EDITORS:

Yudhisther Kumar

Devraj Singh

Kirti Soni

ASI Secretariat,

C/o Acoustics and Vibration Metrology

CSIR-National Physical Laboratory

Dr. KS Krishnan Road

New Delhi 110 012

Tel: +91.11. 4560.8317

Fax: +91.11.4560.9310

E-mail: asisecretariat.india@gmail.com

The Journal of Acoustical Society of India is a refereed journal of the Acoustical Society of India (ASI). The ASI is a non-profit national society founded in 31st July, 1971. The primary objective of the society is to advance the science of acoustics by creating an organization that is responsive to the needs of scientists and engineers concerned with acoustics problems all around the world.

Manuscripts of articles, technical notes and letter to the editor should be submitted to the Chief Editor. Copies of articles on specific topics listed above should also be submitted to the respective Associate Scientific Editor. Manuscripts are refereed by at least two referees and are reviewed by Publication Committee (all editors) before acceptance. On acceptance, revised articles with the text and figures scanned as separate files on a diskette should be submitted to the Editor by express mail. Manuscripts of articles must be prepared in strict accordance with the author instructions.

All information concerning subscription, new books, journals, conferences, etc. should be submitted to Chief Editor:

*B. Chakraborty, CSIR - National Institute of Oceanography, Dona Paula, Goa-403 004,
Tel: +91.832.2450.318, Fax: +91.832.2450.602, e-mail: bishwajit@nio.org*

Annual subscription price including mail postage is Rs. 2500/= for institutions, companies and libraries and Rs. 2500/= for individuals who are not ASI members. The Journal of Acoustical Society of India will be sent to ASI members free of any extra charge. Requests for specimen copies and claims for missing issues as well as address changes should be sent to the Editorial Office:

ASI Secretariat, C/o Acoustics and Vibration Metrology, CSIR-National Physical Laboratory, Dr. KS Krishnan Road, New Delhi 110 012, Tel: +91.11.4560.8317, Fax: +91.11.4560.9310, e-mail: asisecretariat.india@gmail.com

The journal and all articles and illustrations published herein are protected by copyright. No part of this journal may be translated, reproduced, stored in a retrieval system, or transmitted, in any form or by any means, electronic, mechanical, photocopying, microfilming, recording or otherwise, without written permission of the publisher.

Copyright © 2019, Acoustical Society of India

ISSN 0973-3302

Printed at Alpha Printers, WZ-35/C, Naraina, Near Ring Road, New Delhi-110028 Tel.: 9810804196. JASI is sent to ASI members free of charge.

B. CHAKRABORTY
Chief Editor
MAHAVIR SINGH
Managing Editor
A R MOHANTY
Associate Scientific Editor

Yudhishter Kumar Yadav
Devraj Singh
Kirti Soni
Assistant Editors

EDITORIAL BOARD

M L Munjal
IISc Bangalore, India
Michael Vorländer
ITA Aachen, Germany
S Narayanan
IIT Chennai, India
V R SINGH
PDM EI New Delhi-NCR, India
R J M Craik
HWU Edinburg, UK
Trevor R T Nightingale
NRC Ottawa, Canada
N Tandon
IIT Delhi, India
J H Rindel
Odeon A/S, Denmark
G V Anand
IISC Bangalore, India
Gopu R. Potty
University of Rhode Island, USA
S S Agrawal
KIIT Gurgaon, India
Yukio Kagawa
NU Chiba, Japan
D D Ebenezer
NPOL Kochi, India
Sonoko Kuwano
OU Osaka, Japan
Mahavir Singh
CSIR-NPL, New Delhi, India
A R Mohanty
IIT Kharagpur, India
Manell E Zakharia
ENSAM Paris, France
Arun Kumar
IIT Delhi, India
Ajish K Abraham
IISH Mysore, India
S V Ranganayakulu
GNI Hyderabad, India



The Journal of Acoustical Society of India

A quarterly publication of the Acoustical Society of India

Volume 46, Number 3-4, July-October 2019

ARTICLES

- Low frequency noise reduction using helmholtz resonator embedded acoust meta-materials**
Jhalu Gorain and Chandramouli Padmanabhan 87
- A simplified two load transfer matrix approach for the characterization of acoustic elements with and without mean flow**
N.K. Jha, Swapna Singh and R.N. Hota 98
- Performance evaluation and comparison of measured sound insertion loss of corrugated plates**
S.S. Pathan and D.N. Manik 113
- Acoustical properties of jute felt sintered with cotton shoddy**
Manish Raj, Shahab Fatima and Naresh Tandon 125
- Impulsive type acoustic source localization using time delay measurements**
A.R. Mohanty and Chinmayi Mahapatra 132
- A simplified model for predicting breakout noise from a rectangular duct**
Yoganandh M., Nagaraja Jade and B. Venkatesham 145
- Structure Borne Noise – Structural excitation by turbo charger while noise radiation by vehicle components**
Bhushan Singh Gautam 151

INFORMATION

Information for Authors

Inside back cover

GUEST EDITORS' NOTE

Prof. D. N. Manik (IIT-Bombay) and I have the pleasure to present this Special Issue on Noise and Vibration. Comprising seven papers, this special issue of the Journal of the Acoustical Society of India, includes contributions from IIT-Madras, IIT (ISM)-Dhanbad, IIT-Bombay, IIT-Kharagpur, IIT-Hyderabad and Guru Ghesidas Central University, Bilaspur.

In the first paper, a new idea, using an array of miniature Helmholtz resonators in a poro-elastic medium as a unit cell of a periodic acoustic meta-material, is proposed. The idea of miniature Helmholtz resonators is realized using disposable medical syringes. Thus, the material developed is light in weight and holds promise for use in aerospace applications such as payload fairing and airplane fuselage.

The approach proposed in the second paper is an alternative method to characterize acoustic properties, directly relating the incident and reflected wave amplitudes on either side of the specimen. The amplitudes of the traveling waves in the impedance tube are related through a transfer matrix in this approach. All the acoustic parameters needed to characterize the test specimen are shown to be expressible in terms of those wave amplitude transfer matrix elements.

In the third paper, sound insertion loss was measured for a set of corrugated plates comprising of triangular prismatic cavities, formed between the flat surface of plates and inverted 'V' shaped stiffeners. Similar experiments were performed for another set of corrugated plates in which acoustic cavities were avoided, and sound insulation performance of both the set of corrugated plates was compared.

The study in the fourth paper focuses on highlighting the acoustical properties of the waste jute fibers sintered with cotton shoddy. The felts are characterized for their physical parameters and acoustical properties like diameter, density, porosity, tortuosity, airflow resistivity, characteristic lengths, etc. Theoretical results are obtained using Miki model which is later validated with the experimental results obtained.

The fifth paper presents various positioning algorithms based on the Time Difference of Arrival (TDOA) for impulsive type acoustic source localization in both reverberant indoor and free-field outdoor environments. By solving the linear set of equations, a unique solution (source positions and source range) is obtained for both 2D and 3D space. To check the effectiveness and accuracy of each positioning algorithm, the experiments are conducted in different environments.

A simplified model is proposed in the sixth paper to predict total radiation efficiency of the duct using modal radiation efficiency of a simple plate mode. Major contributing mode for sound radiation in the duct is the breathing mode, i.e., dominant symmetric mode on duct's four walls. Modal radiation efficiency of the equivalent simple plate mode (4, 1) is used for the TTL calculations. It is observed that within the cut-on frequency, predicted results from the proposed simple model are in reasonable agreement with the literature data.

Structural vibrations are generated in a turbocharger due to various rotor modes and imbalance present in rotating assembly (rotor-bearing system) which are further transferred to vehicle components through different transfer paths. Along the vibration transfer path, this excitation may be radiated as noise by some sensitive vehicle components in specific frequency ranges. This behavior is captured and analyzed in the seventh paper using acoustic source localization techniques by means of a commercially available tool that implements beam forming technique and acoustic holography.

Thus, this Special Issue of JASI gives the reader a fairly good idea of the research work going on in the area of passive noise control in India.

Dr. M.L. Munjal

Professor (Emeritus) & INSA Honorary Scientist
(Guest Editor)

The reviewers of this issue :

1. Prof. M.L. Munjal
2. Prof. D.N. Manik
3. Prof. S. Narayanan

Low frequency noise reduction using helmholtz resonator embedded acoust meta-materials

Jhalu Gorain and Chandramouli Padmanabhan

*Department of Mechanical Engineering, Indian Institute of Technology Madras,
Chennai-600036, India
e-mail: jhalugorain@gmail.com*

[Received: 11-12-2019; Revised: 03-03-2020; Accepted: 17-03-2020]

ABSTRACT

Noise attenuation at low frequencies is one of the major challenges in industry. A new idea, using an array of miniature Helmholtz resonators in a poro-elastic medium, as a unit cell of a periodic acoustic meta-material, is proposed. The challenge is to keep the size small yet to make it work at low frequencies. The idea of miniature Helmholtz resonators is realized using disposable medical syringes. These resonators are embedded in a 20 mm thick PU foam and its absorption coefficient is determined using an impedance tube. An array of such resonators with different combinations is shown to enhance low frequency absorption, from 250-500 Hz. After this, the HR embedded meta-material is tested in a cylindrical cavity for its acoustic performance. It is shown that a 13 dB reduction at 262 Hz and 9 dB at 532 Hz can be achieved. The material developed is light in weight and holds promise for use in aerospace applications such as payload fairing and airplane fuselage, where there is a need for enhanced low frequency noise reduction with minimum increase in system weight.

1. INTRODUCTION

For the past few decades, noise attenuation at low frequency has been one of the major challenges. A low frequency wave is associated with a longer wave length which makes its manipulation difficult. A wave of longer wavelength cannot be captured easily using conventional and existing noise control treatments. Among the existing treatments, the most widely used is the micro-perforated panel (MPP)^[1,2] absorbers. To make MPP more effective, the idea of different backed air cavity depths^[3] and cavity partitions^[4,5] have been explored. Another solution is the use of the Helmholtz resonator^[5, 6] (HR) with modifications such as degenerate resonators^[7], resonant patches^[8] and multiple orifices^[9] to improve low frequency noise reduction. Recently, the concept of multiple orifices with intrusions^[10] has been proposed to reduce low frequency sound of a rectangular cavity. Generally, as the frequency goes down the design of MPP becomes difficult while the required size of HR becomes bigger. These solutions have typically been effective in narrow frequency bands around targeted frequencies.

Researchers have proposed the idea of double porosity material^[11] to improve the low frequency performance. The concept of mass inclusion in the poro-elastic materials^[12,13] has also been introduced as a possible solution. The embedded masses combined with porous material form an array of spring-mass-damper systems and improve the acoustic performance. Since the material is a combination of porous

media and embedded masses therefore, it is termed as a heterogeneous (HG) blanket. The embedded masses as resonators at different locations in a particular pattern inside the porous media became more effective than earlier acoustic treatments. For further improvement in absorption capability, the proposed HG blanket has been investigated with various embedded masses such as steel balls, Styrofoam balls and hollow aluminum balls^[14]. These again do not yield broad band low frequency noise reduction.

In recent years the idea of acoustic metamaterials (AMM) seems to hold promise to mitigate low frequency noise. The first AMM, sonic crystal^[15], has been demonstrated using lead balls covered with silicone rubber. The author who proposed the HG blanket explored the absorption coefficient using mass embedded and MPP based AMMs^[16]. At around the same time, the effect of a resonant inclusion in a porous material was investigated using TMM and P-TMM based analytical modelling approach^[17]. Apart from the porous media based AMM, honeycomb based AMM^[18], membrane and plate-type^[19] AMMs and meta-surfaces^[20] coupled with HRs have been developed and their effectiveness demonstrated through experiments. Recently, active metamaterial and meta-surface^[21, 22], are also reported as yet another class of metamaterial. But all of them are heavier because of either larger thickness of porous media or larger dimensions of HR/included masses and perform only over a limited low frequency range.

In this paper, the concept of a mini HR and its ability to improve sound absorption will first be demonstrated. The use of these mini resonators with slightly different resonant frequencies (detuning) is then shown to broaden the range of low frequencies over which significant absorption can be achieved. While the first two objectives will be carried out using an impedance tube, the new meta-material proposed (array of HRs in poro-elastic foam) is tested in a cylindrical cavity to demonstrate its effectiveness in a more practical situation.

2. MINIATURE HR AND ITS DETUNING

2.1 Syringe : A miniature HR

Several HR designs have been proposed and are being used in practice but most of them are bigger in size and offer narrow band sound absorption at low frequencies. To reduce its size and to get an enhanced absorption capability over a broader frequency range, the idea of miniature HR is proposed by using disposable medical syringes of different sizes.

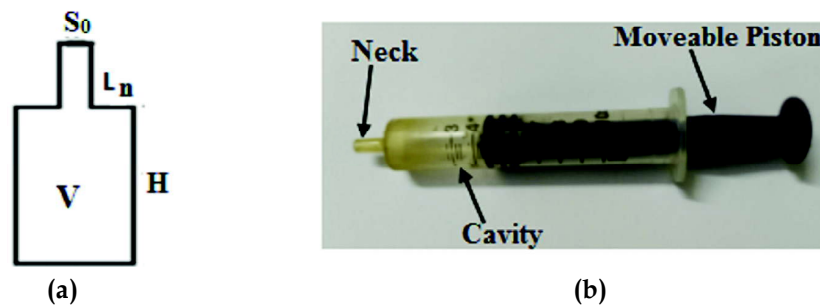


Fig. 1. (a) Schematic of a HR (b) 10 cc syringe.

The ready-made medical syringe, shown in Fig. 1 (b), is very similar to a HR. Its compact design makes it smaller than other existing HRs. The dimensions and geometry details of medical syringes considered in this study are given in Table 1.

Syringes are similar to a conventional HR with an additional advantage of variable cavity depth which can be achieved by using moveable piston. To predict the impedance of a conventional HR Komkin *et al.*^[23] proposed an analytical impedance model incorporating thermal and viscous losses:

$$Z = \frac{S}{S_0} \left[R_e + j \left(\omega M_e - \frac{C_e}{\omega} \right) / \rho_0 c S_0 \right] \quad (1)$$

Table 1. Different types of geometries of HR.

Syringe Size (cc)	Geometry Type	Cavity Diameter (mm)	Cavity Length (mm)	Neck Diameter (mm)	Neck Length (mm)	Targeted Frequency (Hz)
10	G1	14	24	2	9	480
10	G2	14	58	2	9	350
10	G3	14	86	2	9	265
10	G4	14	73	2	9	300

where S and S_0 are cross-sectional areas of the cavity and the neck respectively; R_e is the resistance and expressed as $R_e = (R_v + R_\chi)$, with R_v viscous losses and R_χ thermal resistance (see Ref.[23] for detailed explanations of R_v and R_χ); ω is the angular frequency; M_e is the effective lumped mass of the air inside the neck and is calculated as $M_e = \rho_0 S_0 (L_n + \delta)$, with L_n the neck length and δ the end correction factor proposed by Ingard (Ref.[6]); C_e is the compliance due to the cavity of HR/syringe and calculated as $C_e = \rho_0 c^2 S_0^2 / V$, with ρ_0 the air density (1.21 kg/m³), c is the speed of sound in air (343 m/s) and V volume of the cavity.

From the normalized impedance (Z) of HR, the absorption coefficient, $\alpha(f)$, can be determined as follows:

$$\alpha(f) = 1 - \left| \frac{Z-1}{Z+1} \right|^2 \tag{2}$$

2.2 Experiment set up and sample details

A series of tests were conducted in a 6 inch impedance tube designed and developed as per ISO standards (ISO 10534-2) at IIT Madras[24]. In all the tests, white noise, produced by the speaker, is used as an input while sound pressure is measured using two ¼ inch pressure microphones. Standard procedure of measurements have been followed in all cases. The auto and cross spectral densities from the microphone measurements are acquired and data is processed to obtain the absorption coefficients using two microphone method[25].

To demonstrate the concept of miniature HR and to investigate its effect on absorption coefficient, resonator sets with different number of syringes were first investigated. An array of such syringes embedded into foam was also tested in the impedance tube. In each case, the type of sample tested and its description are given in Table 2.

Table 2. Different samples tested in impedance tube.

Sample Type	Sample Description
S1	1 syringe of type G4 at the centre of the sample holder
S2	9 syringes of type G4 placed 1 at the centre and 8 along the circumference of R55 mm
S3	9 syringes, 3 G1 type, 3 G2 type and 3 G3 type with 1 at the centre and 8 along circumference of R55 mm of a base plate
S4	9 syringes, 3 G1 type, 3 G2 type and 3 G3 type, embedded in 20 mm PU foam at the same location as in case 3

*See Table 1 for explanation of syringe types G1-G4.

It is also worth mentioning that the base plate, shown in Fig. 2 (c), in all the cases is attached to the tube using m-seal. The plate has 9 through holes, a schematic view of which is shown in Fig. 2 (b), where

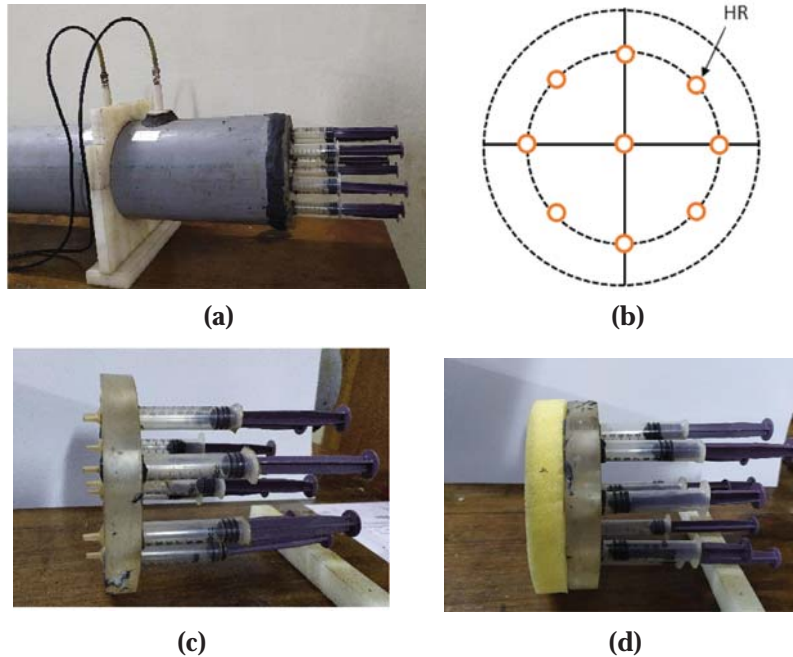


Fig. 2. (a) Sample holder portion of impedance tube (b) HR placement in base plate (c) Sample S2 (d) Sample S4.

syringes have been placed. The foam is placed in front of the neck flush into the tube. It is placed in such a way that it ensures that there is no air gap between the base plate and foam.

2.3 Results and Discussions

2.3.1 Single and an array of same type of HRs

For validating the concept of miniature HR sample S1 and S2 are tested in the impedance tube. The solid lines, shown in Fig. 3 and Fig. 4, are experimental absorption curves of S1 and S2 whereas the dashed lines represent analytical prediction curves of HRs tuned at 300 Hz. The analytical absorption coefficient is calculated using Eqs. (1) and (2). Refer to Ref.^[23] for expressions for resistance, inertia and compliance terms and their detailed derivations. The amplitude of the absorption curves of S2, shown in Fig. 4, have increased around 300 Hz as expected. The increased amplitude in Fig. 4 indicates that as the number of HRs increase the overall absorption coefficient also increases.

The experimental results of samples S1 and S2 agree well with the analytical solutions. The small discrepancies in both the plots are due to tube absorption (PVC material) and this is shown in each plot.

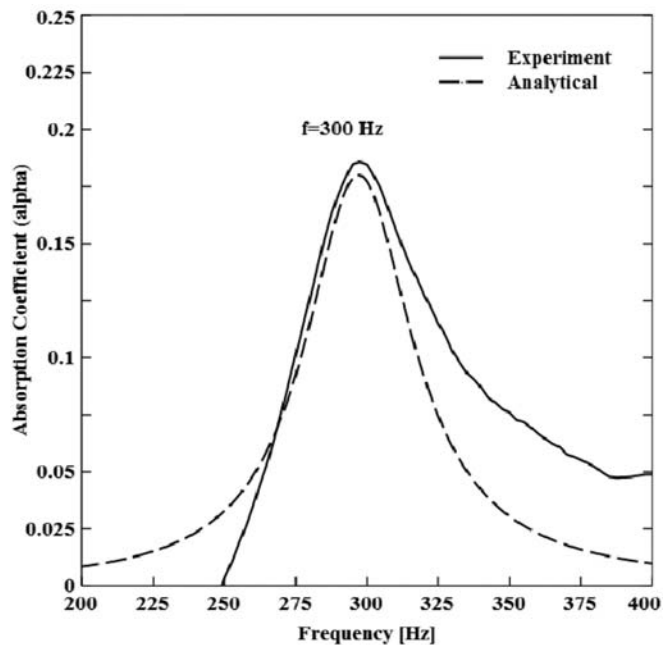


Fig. 3. Absorption coefficient of sample S1.

From these initial investigations, it is quite clear that the disposable medical syringe or its equivalent geometry can be used as a compact and miniature HR. A single syringe may not be very effective but an array of them does provide enhanced absorption at the targeted frequency.

2.3.2 An array of multiple type HRs

To get a broader bandwidth of absorption capability, the idea of detuning of HR was investigated experimentally by using a combination of syringes of same diameter but different cavity lengths. The sample S3 is prepared as described in the Table 2 and tested in an impedance tube. The investigation was done with different combinations of 9 syringes and absorption plot was obtained from the processed data. The absorption plot, shown in Fig. 5, has three peaks at the targeted frequencies. The absorption peaks at each targeted frequency are smaller than the peak absorption due to an array of same type of HRs as shown in Fig. 4. However, the absorption coefficient has now been enhanced over a wider frequency range.

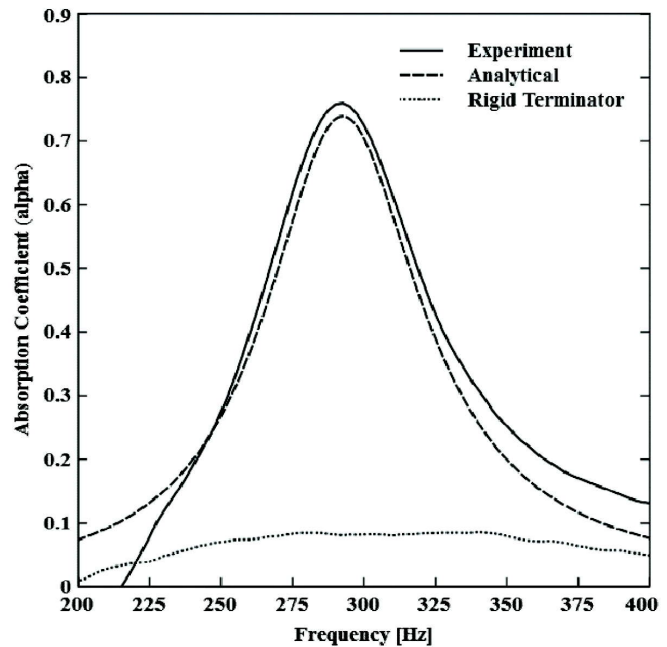


Fig. 4. Absorption coefficient of sample S2.

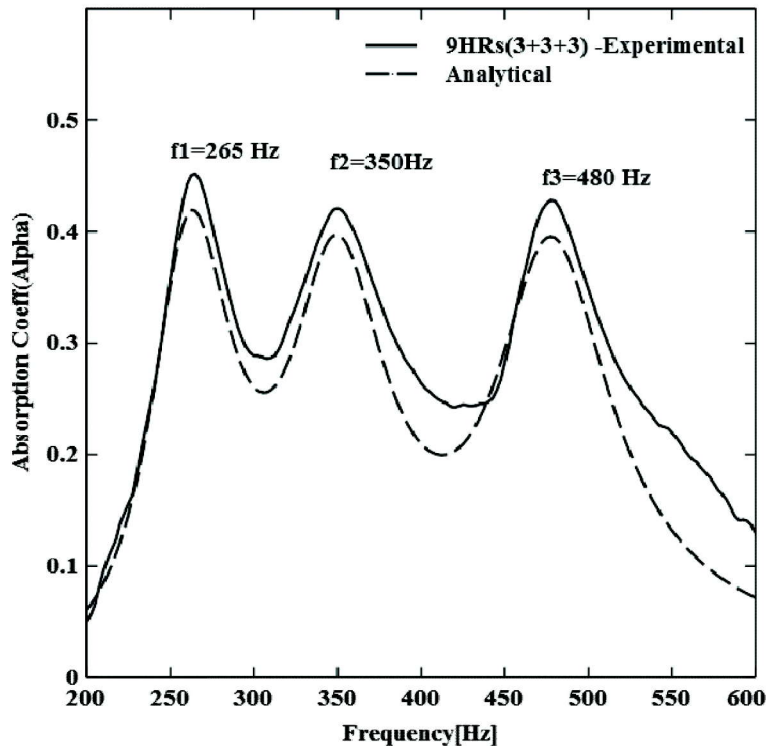


Fig. 5. Absorption coefficient of sample S3.

2.3.3 Array of HRs embedded into a foam: AMM

Poro-elastic materials are usually not effective for low frequency noise reduction. Hence, a new acoustic metamaterial is proposed using Helmholtz resonators and poro-elastic materials. A unit cell of the new acoustic material was prepared by using PU foam as a poro-elastic material and 10 cc syringes of different lengths as a miniature Helmholtz resonator. The surface impedance of the foam is determined by the equivalent liquid-fluid model and is given by:

$$Z_{foam} = \frac{jZ_c}{\phi \tan \tan(k_c L)} \quad (3)$$

$$Z_c = \sqrt{\rho K}; k_c = \omega \sqrt{\frac{\rho}{K}} \quad (4)$$

Where ϕ is the porosity, ρ effective density of fluid and K bulk modulus of the fluid.

The effective density, ρ and bulk modulus, K are given by the Johnson-Champoux-Allard-Lafarge (JCAL) model. Refs.^[26, 27] provide a detailed derivation of the effective density and the bulk modulus. Other unknown parameters used in the liquid-fluid model are estimated using inverse acoustical characterization method^[28]. The total impedance of the proposed AMM, shown in Fig. 2(d), is the combined effect of the HR impedance, calculated from Eq. (1) and foam impedance, calculated from Eq. (3).

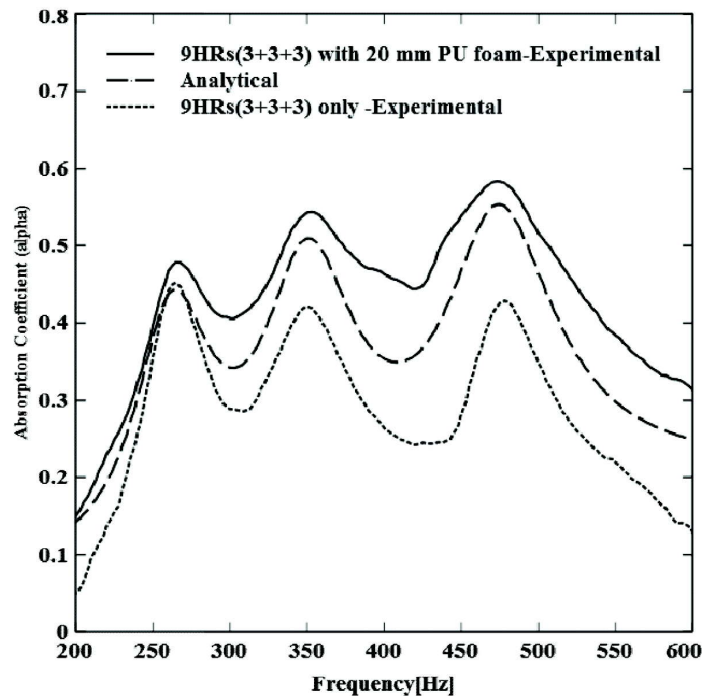


Fig. 6. Absorption coefficient of sample S4.

The total weight of the newly developed acoustic metamaterial unit cell has a weight of only 28 gm. The absorptive performance of 20 mm foam alone is quite low over the chosen band. At 265 Hz the combined effect of foam and HR is similar to S4 but at 350 Hz and beyond its effect is visible. Also the dip between the peaks are also reduced which is good from an absorption view point. More importantly, below 500 Hz, the new metamaterial has shown greater broad band absorption capability when compared with earlier ideas^[16]. The developed metamaterial is light in weight and also cheaper in cost. Hence the newly designed HR embedded acoustic metamaterial will be very useful for aerospace applications such as payload fairing and airplane fuselage.

3. DEMONSTRATION OF NEW AMM IN A CAVITY

3.1 Experiment set up and sample preparation

For checking the effectiveness of the proposed novel material a demonstration was conducted using a cylindrical cavity. The cavity, as shown in Fig. 7(a), is made of mild steel (MS) of thickness 3 mm, diameter 600 mm and height 660 mm. The bottom and the top ends are covered by MS and Acrylic plates respectively. Both the plates are bolted with the cavity and leakage is arrested by using proper sealing material. The speaker of 6 inch diaphragm is fixed at the center of the bottom plate whereas the developed material is applied at the bottom of the top acrylic plate of thickness 12 mm. A quarter inch condenser type microphone is fixed with the help of a holder at a distance of 150 mm from the top. The microphone is connected to a four channels Data Acquisition System whereas the speaker is connected to a power amplifier.

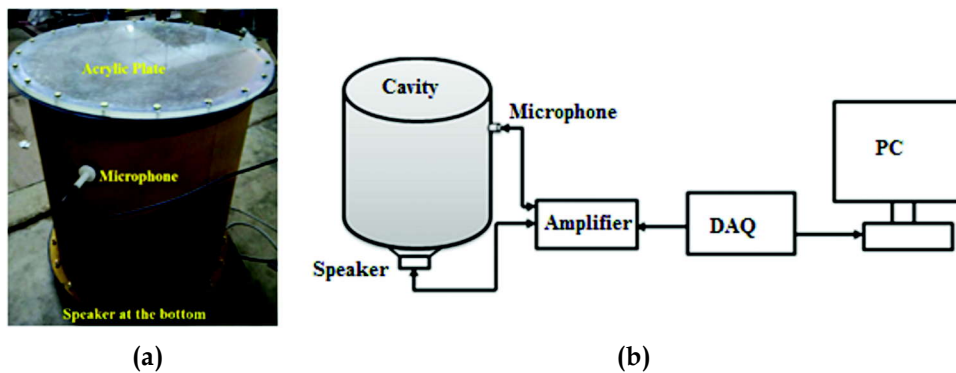


Fig. 7. (a) Cylindrical cavity, (b) Schematic diagram of cavity test.

Syringes, flush inside the cavity, are mounted on the drilled hole in the acrylic sheet at three different radii: 8, 16 and 24 cm. The number of HR placed circumferentially and equally spaced at these three radii are 8, 12 and 20 respectively. The schematic of placement of HR inside the cavity is shown in Fig. 8(b).

A series of experiments were conducted with four different conditions as follow : Cavity with only acrylic plate, Acrylic plate with 20 mm PU foam of density 16 kg/m^3 , Acrylic plate with HRs alone and Acrylic plate with new AMM (Foam+ HR). The typical dimensions of HRs for the first axial mode 262 Hz are the same as mentioned in Table 1. For case 3 and 4, a total of 36 HRs are placed in the acrylic plate at three different radii as shown in Fig. 8. The number of HR placed at the periphery of circle of radius 8 cm, 16 cm and 24 cm are 8, 12 and 20 respectively. All the three samples are shown in Fig. 8(a).

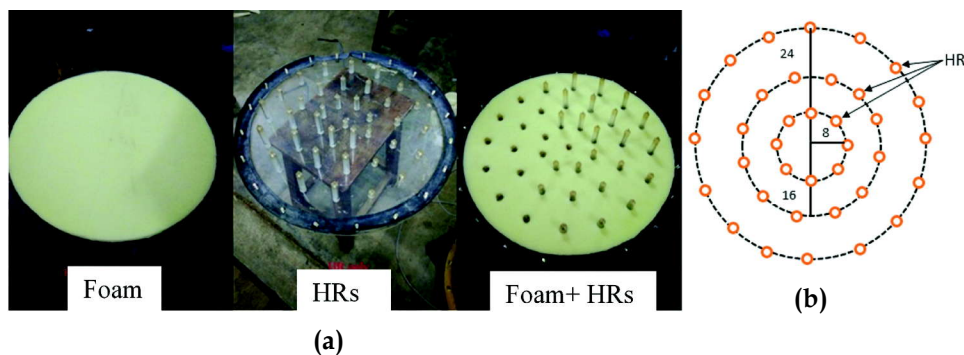


Fig. 8. (a) Acrylic plates in different test conditions, (b) Schematic of HR placement.

The first set up was done with acrylic plate only and subsequently other three. A white noise excitation with intensity 0.8 RMS V was given as an input and sound pressure level was recorded.

3.2 Results and Discussions

The sound pressure level plot clearly indicates that foam, shown by red dotted line in Fig. 9, has no effect at 265 Hz which is expected whereas the HRs, shown by solid line, reduces the SPL significantly at 265 Hz. A total of 14 dB reduction is recorded at 265 Hz. Apart from this, a good reduction in SPL by new AMM, shown by red dotted line, at radial modes 360 Hz and 435 Hz was also observed.

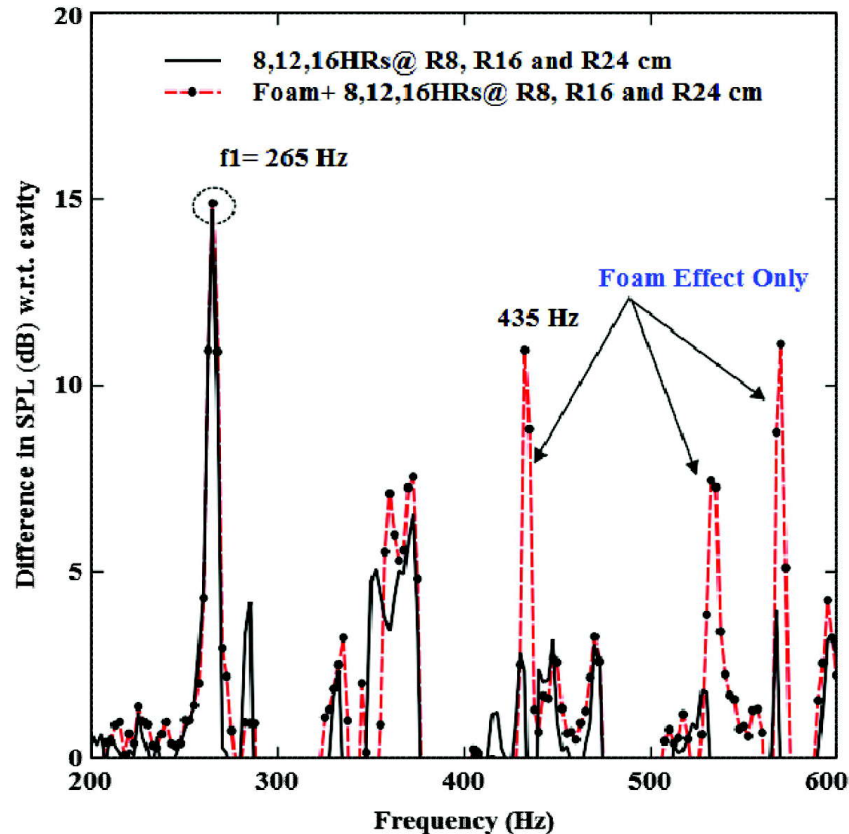


Fig. 9. SPL (dB) difference with respect to the cavity alone for HRs tuned to 265 Hz.

The same set of experiment was repeated using the newly developed HRs embedded AMM for the second mode. Similarly, at 532 Hz a total of 14-15 dB reduction in SPL, as shown in Fig. 10 by black line with dot, is observed due to the combined effect of foam and resonators. Merely a difference of 2-3 dB was found in between 24 and 36 HRs as shown in by red and green curves in Fig. 10; so once a certain number of HRs are reached the sound reduction achieved saturation.

For investigating the effect of the HR embedded AMM over a range of 200-550 Hz, a combination of different dimensions of HRs were placed at 3 different places. A combination of 18+18 HRs for targeted frequencies 265 Hz and 532 Hz was used. The places of HRs interchanged among three different radii and investigated their effectiveness to get an optimal configuration. The red dotted line in Fig. 11 shows 10 dB and 13 dB reduction in SPL at frequencies 265 Hz and 532 Hz respectively. Apart from axial modes, due to foam a good reduction, as shown by dotted line in Fig. 11, is also found at mid-range of the targeted band.

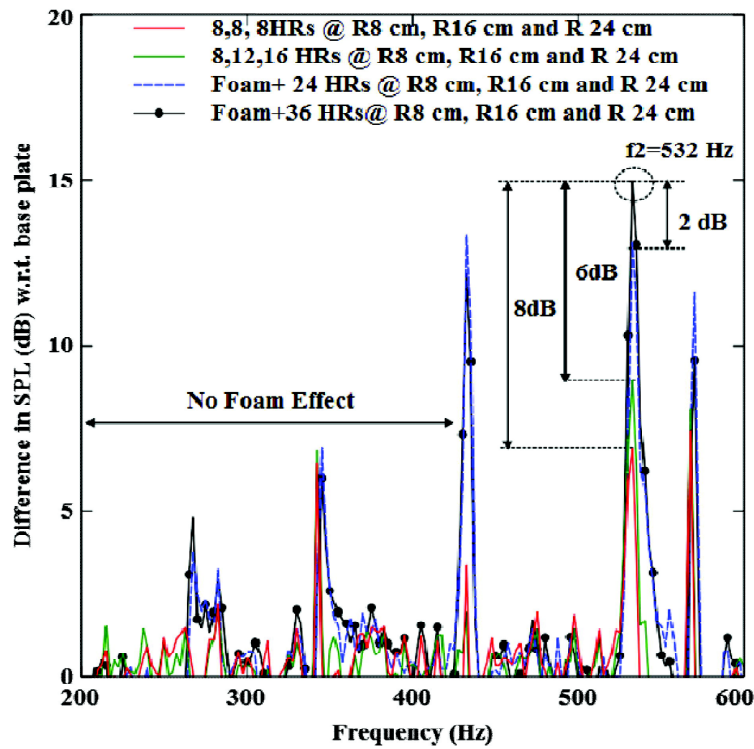


Fig. 10. SPL (dB) difference with respect to the cavity alone for HRs tuned to 532 Hz.

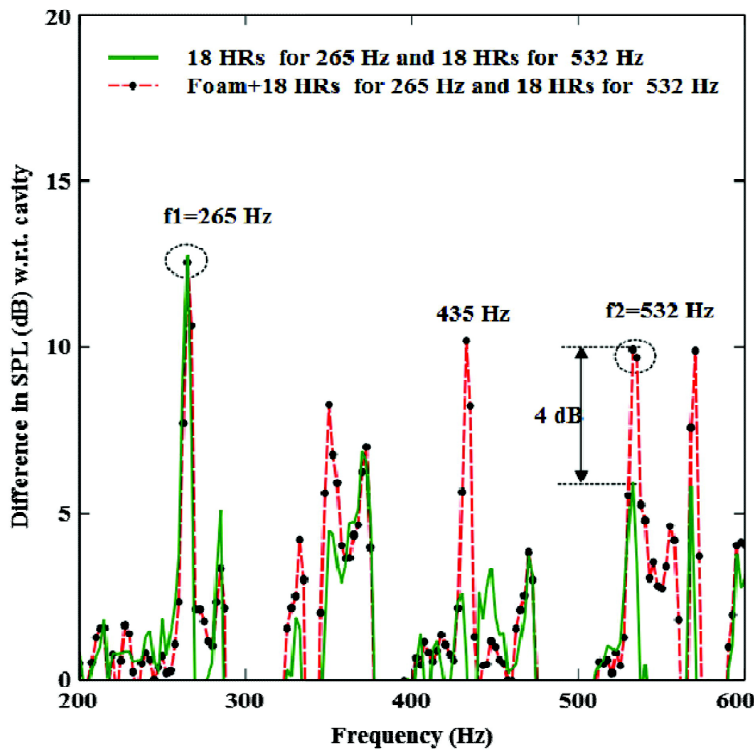


Fig. 11. Reduction of SPL (dB) w.r.t. the cavity at different cases for 265 Hz and 532 Hz.

4. CONCLUSION

The problems pertaining to existing treatments for mitigating low frequency noise were addressed and a new idea of HR embedded AMM has been demonstrated. The concept of syringe as small resonators holds promise in providing broadband absorption at the targeted low frequency range, 200 Hz-550 Hz. These HRs can also be tuned to frequencies below 200 Hz with the help of moveable piston of syringe. These experimental investigations will provide the insights for developing and optimizing detuned HR embedded AMM. The cavity experimental investigations have shown that small HR embedded acoustic metamaterial can significantly reduce the sound pressure levels at all targeted frequencies. It offers a broader absorption band and it is light in weight compared to previously suggested metamaterials.

6. REFERENCES

- [1] D.Y. Maa, 1975. Theory and design of micro-perforated-panel sound absorbing construction, *Sci. Sinica*, **18**(1), 55-71.
- [2] D.Y. Maa, 1998. Potential of micro perforated panel absorber, *J. Acoust. Soc. Am.*, **104**(5), 2861-2866.
- [3] C. Wang and L. Huang, 2011. On the acoustic properties of parallel arrangement of multiple micro-perforated panel absorbers with different cavity depths, *J. Acoust. Soc. Am.*, **130**(1), 208-218.
- [4] D. Herrin and J. Liu, 2011. Properties and applications of micro perforated panels, *J. Sound Vib.*, **7**, 6-9.
- [5] M. Yairi, K. Sakagami, K. Takebayashi and M. Morimoto, 2011. Excess sound absorption at normal incidence by two micro perforated panel absorbers with different impedance, *Acoust. Sci. Tech.*, **32**(5), 194-200.
- [6] U. Ingard, 1953. On the theory and design of acoustic resonators, *J. Acoust. Soc. Am.*, **25**(6), 1037-1061.
- [7] C. Cai and C.M. Mak, 2018. Noise attenuation capacity of a Helmholtz resonator, *Adv. Eng. Soft.*, **116**, 60-66.
- [8] M. Yang, C. Meng, C. Fu, Y. Li, Z. Yang and P. Sheng, 2015. Sub wave length total acoustic absorption with degenerate resonators, *Appl. Phys. Lett.*, **107**(10), 104104-5.
- [9] M. Farooqui, T. Elnady and W. Akl, 2016. Validation of low frequency noise attenuation using locally resonant patches, *TJ. Acoust. Soc. Am.*, **139**(6), 3267-3276.
- [10] C.V. Reddi and C. Padmanabhan, 2015. Design relation and end correction formula for multi-orifice Helmholtz resonators with intrusions, *Proc. IMechE Part C: J. Mech. Eng. Sci.*, **230**(6), 939-947.
- [11] F.C. Sgard, X. Olny, N. Atalla and F. Castel, 2005. On the use of perforationsto improve the sound absorption of porous materials, *Appl. Acoust.*, **66**(6), 625-651.
- [12] M.R.F. Kidner, C.R. Fuller and B. Gardner, 2006. Increase in transmission loss of single panels by addition of mass inclusions to a poro-elastic layer: Experimental investigation, *J. Sound Vib.*, **294**(3), 466-472.
- [13] C.R. Fuller and R.L. Harne, 2009. Advanced passive treatment of low frequency sound and vibration, *Proc. Acoustics*, 2009, Adelaide, Australia, 3-25 November, (2009).
- [14] A.C. Slagle and C.R. Fuller, 2015. Low frequency noise reduction using poro-elastic acoustic metamaterials, *21st AIAA/CEAS Aero Acoust. Con.*, 3113, 2015, 22-26 June, Dallas, TX.
- [15] P. Sheng, X.X. Zhang, Z. Liu and C.T. Chan, 2003. Locally resonant sonic materials, *Physica B*. **338**, 201-205.
- [16] C.R. Fuller and G. Mathur, 2017. Poro-elastic acoustic metamaterials. Inter-Noise, 2017, Hang Kong, August 27-30, China.

- [17] C. Lagarrigue, J.P. Groby, V. Tournat, O. Dazel and O. Umnova, 2013. Absorption of sound by porous layers with embedded periodic arrays of resonant inclusions, *J. Acoust. Soc. Am.*, **134**(6), 4670-4680.
- [18] S. Sugie, J. Yoshimura and T. Iwase, 2009. Effect of inserting a Helmholtz resonator on sound insulation in a double-leaf partition cavity, *Acoust. Sci. Tech.*, **30**(5), 317-326.
- [19] T.-Y. Huang, C. Shen and Y. Jing, 2016. Membrane- and plate-type acoustic metamaterials, *J. Acoust. Soc. Am.*, **139**(6), 3240-3250.
- [20] J. Li, W. Wang, Y. Xie, B.I. Popa and S.A. Cummer, 2016. A sound absorbing metasurface with coupled resonators, *Appl. Phys. Lett.*, **109**(9), 91908-4.
- [21] Y. Wu, M. Yang and P. Sheng, 2018. Perspective: acoustic metamaterials in transition, *J. Appl. Phys.*, **123**(9), 90901-7.
- [22] G. Ma, X. Fan, P. Sheng and M. Fink, 2018. Shaping reverberating sound fields with an actively tunable metasurface, *Proc. National Academy Sci.*, **115**(26), 6638-6643.
- [23] A.I. Komkin, M.A. Mironov and A.I. Bykov, 2017. Sound Absorption by a Helmholtz Resonator, *Acoust. Phys.*, **63**(4), 356-363.
- [24] ISO 10534-2, 1998. Acoustics-Determination of sound absorption coefficient and impedance in impedance tubes-Part 2: Transfer function method, International Standardization Organization.
- [25] A.F. Seybert, 2005. Two sensor methods for the measurement of sound intensity and acoustic properties in ducts, *J. Acoust. Soc. Am.*, **83**(6), 2233-2239.
- [26] Y. Champoux and J.F. Allard, 1991. Dynamic tortuosity and bulk modulus in air saturated porous media, *J. Appl. Phys.*, **70**(4), 1975-1979.
- [27] J. Allard and N. Atalla, 2009. Propagation of sound in porous media: Modelling sound absorbing materials 2e, *John Wiley & Sons*, p. 90.
- [28] P. Bansod and A. Mohanty, 2016. Inverse acoustical characterization of natural jute sound absorbing material by the particle swarm optimization method, *Appl. Acoust.*, **112**, 41-52.

A simplified two load transfer matrix approach for the characterization of acoustic elements with and without mean flow

N.K. Jha, Swapna Singh and R.N. Hota *

*Department of Mechanical Engineering, Indian Institute of Technology
(Indian School of Mines), Dhanbad, Jharkhand 826004, India
e-mail: rnhota@iitism.ac.in*

[Received: 29-10-2020; Revised: 15-03-2020; Accepted: 17-03-2020]

ABSTRACT

The ASTM Two-Load method is a widely applied standard method to calculate the acoustic properties of the materials. This method uses a transfer matrix approach and characterizes the acoustic properties based on the decomposition of the standing wave pattern. A simplification to this standard method has been proposed in the present work. The proposed approach is an alternative method to characterize acoustic properties, directly relating the incident and reflected wave amplitudes on either side of the specimen. The amplitudes of the travelling waves in the impedance tube are related through a transfer matrix in this approach. All the acoustic parameters needed to characterize the test specimen are shown to be expressible in terms of those wave amplitude transfer matrix elements. The calculation steps followed in the proposed method is shown to be much less than the standard method. A comparison is carried out between the simplified method and the standard ASTM method. The proposed method provides results that agree well with the standard method. This simplified method also accounts for the mean flow and the effect of end conditions, which makes it more realistic and closer to the practical problems.

1. INTRODUCTION

For the purpose of noise-control, acoustical elements like mufflers^[1], sound-absorbing materials and perforated liners^[2] are widely applied. The acoustic performance of such elements can be estimated by several parameters that mainly include impedance, transmission loss, and absorption coefficient. There are several existing measurement techniques for their estimation such as standing wave ratio (SWR) method, steady-state random excitation technique, and transfer matrix method (one-load, two-load, and two-source method). Melling^[3] described a technique, called two microphone standing wave ratio (SWR) method in the past which later became obsolete as it included traversing microphone, discrete frequency measurements, and a constant experimental condition for over a considerable amount of time. Yaniv^[4] measured the characteristic impedance by employing two microphones and two types of cavities, known as two-cavity method. Later, the two microphone steady-state random excitation technique was introduced^[5-7] by expressing the acoustic quantities in terms of auto and cross-spectral densities. To and Doige^[8,9] introduced transient testing techniques by utilizing the pressure measurements of four

microphones to get the transfer matrix parameters. Lung and Doige^[10] extended this transient testing technique for the direct measurements of four-pole parameters (matrix parameters) by employing two different loads (end conditions), and four microphones to solve four equations. Their approach is popularly regarded as Two-Load method. They pointed out the strict requirement of loads not to be identical over the range of frequency, that if the two loads are very similar, the results will be unstable. The Two-Load method can also be applied in the presence of mean flow and do not possess the strict requirement of the anechoic termination. This method gained wide popularity as it can be applied in the presence of mean flow and also the elements need not to be geometrically symmetric. However, for a geometrically symmetrical element, the four-microphone one-load standard method can also be applied using a single termination and with the concept of reciprocity^[11]. Munjal and Doige^[12] introduced the two-source method for the estimation of four-pole parameters by placing two sound sources before and after the element for two successive measurements. In a recent work, Bonfiglio and Pompoli^[13] directly related the complex amplitudes of the travelling waves (decomposed standing waves) through a transfer matrix. However, their work used a single measurement technique for a homogeneous element. Their work was also limited to getting only transmission loss and without any mean flow considerations. Though the two-source method is widely accepted, the Two-Load method is convenient to employ as the source does not have to be moved and also all type of loads can be employed. Researchers found the Two-Load method to be more reliable and practical among other existing methods. This method has been standardized in ASTM E2611-09¹¹. However, application of the Two-Load Method follows a relatively complicated and lengthy procedure in the author's viewpoint. It is important to note that authors do not point out any discrepancy in the standard method. Also, the authors do not intend to modify the standard method. It is in this context that an investigation is carried out to simplify the standard Two-Load method. This results in a new simplified method which is based on the work reported by Bonfiglio and Pompoli^[13] and utilization of the formulation of the standard ASTM test procedure. The present simplified method directly relates the complex wave amplitudes on both sides of the acoustic element through transfer matrix elements. It is shown that all the parameters of acoustic elements characterization are expressible in terms of these transfer matrix elements. Two different end conditions (loads) have been used to get the value of four matrix elements. The present method uses the same pressure measurements as used by the Two-Load method. The work reported by Bonfiglio and Pompoli^[13] is limited to calculating TL without accounting for the end-conditions other than the anechoic termination. Apart from this, the effect of mean flow has also not been considered in their formulation. The present method is an extension of their work which includes the convective (flow) terms in the formulation taking all types of end conditions into consideration. This method can be applied for the calculation of any acoustic parameter needed for the characterization of acoustic elements. Like the ASTM method ASTM E2611-09, its application also includes the presence of mean flows. The acoustic parameters, *viz.* transmission loss and absorption coefficient are calculated and plotted for the two methods.

This paper is structured as follows. In section 2, the existing Two-Load method and the proposed method are described. The experimental measurement procedure is described in section 3. The ASTM Two-Load method is considered for the validation of the proposed simplified method. Finally, Section 4 presents the results of the experimental measurements. The acoustical elements compact acoustic filter and bias flow perforated liner are considered to demonstrate the capability of the present method.

NOMENCLATURE

\bar{u}_u, \bar{u}_d	upstream and downstream mean flow velocity
A_u, A_d	upstream and downstream area of cross-section
A_L	liner cross-sectional area
\bar{v}_h	steady bias flow velocity through each hole
k_u^\pm, k_d^\pm	upstream and downstream travelling wave numbers
k	wave number
L	liner length

C	speed of sound
L_d	length of downstream impedance tube
R_d	downstream reflection coefficient
M	flow Mach number
A, B, C, D	complex wave amplitudes
T	transmission coefficient
R	reflection coefficient
X	axial coordinate

Greek letters

ω	angular frequency
σ	porosity
α	absorption coefficient
Δ	determinant of coefficient matrix
ρ	density

Subscript

u, d	upstream, downstream
g, b	grazing flow, bias flow
h	liner hole
T, R	transmission and reflection coefficient
L	liner
C	aero acoustic variables
N	normal incidence

Superscript

\pm	forward and backward travelling waves
-------	---------------------------------------

2. MATHEMATICAL MODELLING

2.1 ASTM Two-Load Method

The standard 'Two-Load Method'^[11] is used to characterize the bias flow perforated liners and the compact acoustic filter. The standard Two-Load method available in ref.^[11] doesn't account the effect of

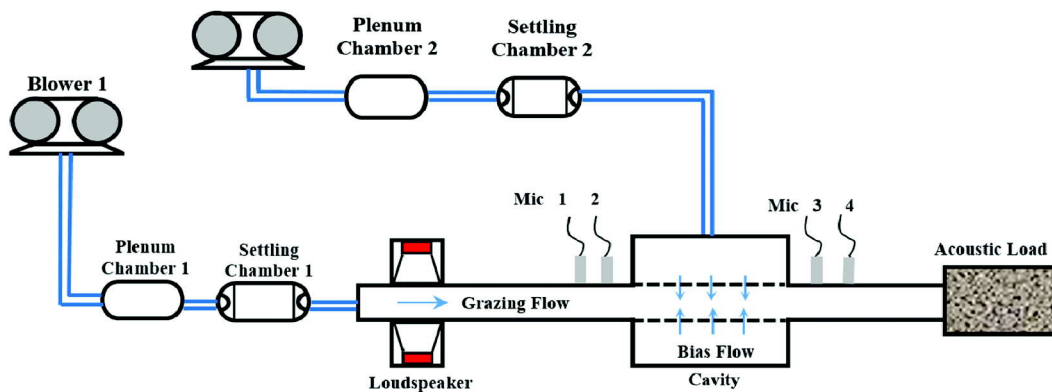


Fig. 1. Schematic of the measurement setup

A simplified two load transfer matrix approach for the characterization of acoustic elements mean flow

mean flow. However, the Modified Two-Load method considering the effect of flow can be found in Das *et al.*[14] and Jha *et al.*[15]. Figure 1 shows the schematic of the measurement setup. There is an impedance tube with loudspeakers as sound source connected at one end and the test element mounted in between, followed by acoustic loads at another end. Four microphones, two on both side of the test section are flush mounted to the circumference of the tube. Sound sources are mounted at certain locations upstream to get plane waves in the impedance tube.

The propagation of these plane waves results in a standing wave pattern, which is measured at four locations simultaneously with the help of microphones and decomposed into forward and backward travelling wave components[11]. These decomposed wave components are further used to get the transfer matrix elements. The transfer matrix (four-pole parameter representation) relates the acoustic pressure and particle velocities on either side of the test specimen.

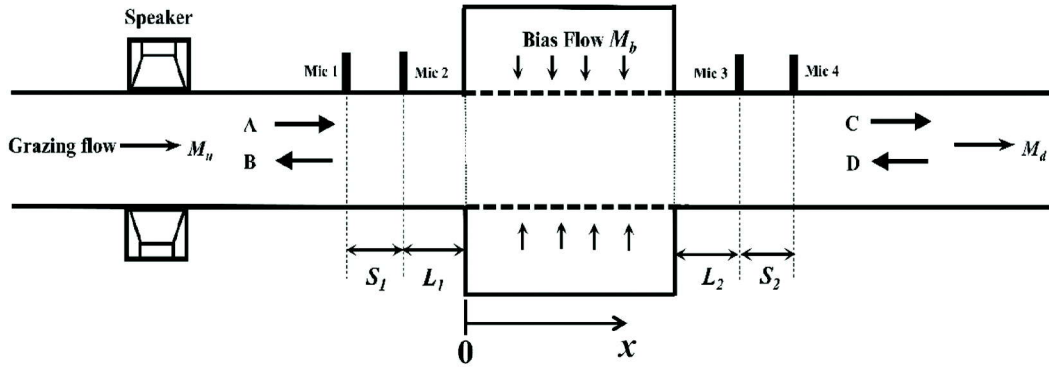


Fig. 2. Schematic of the impedance tube

It is considered that the wave fields in the upstream and downstream sections of the impedance tube can be well estimated by the superposition of plane waves in the positive and negative directions. In the impedance tube, pressure P_1 to P_4 at four axial measurement locations *i.e.* x_1 to x_4 may be represented by the superposition of forward and backward travelling plane waves, in the upstream and downstream sections, given as :

$$P_1 = Ae^{-ik_u^+x_1} + Be^{ik_u^-x_1} \quad (1a)$$

$$P_2 = Ae^{-ik_u^+x_2} + Be^{ik_u^-x_2} \quad (1b)$$

$$P_3 = Ce^{-ik_d^+x_3} + De^{ik_d^-x_3} \quad (1c)$$

$$P_4 = Ce^{-ik_d^+x_4} + De^{ik_d^-x_4} \quad (1d)$$

Where $x_1 = -(L_1 + S_1)$, $x_2 = -L_1$, $x_3 = L_2$, $x_4 = L_2 + S_2$. The notations L_1 , L_2 , S_1 and S_2 are used for the axial positions of the microphone as shown in Fig. 2. A steady grazing flow of Mach number $M_g = \bar{u}_u/c$ is present upstream of the lined section and a steady bias flow of Mach number $M_b = \bar{v}_h/c$ through the liner holes. The Mach numbers upstream and downstream of the tube can be written as :

$$M_u = M_g \quad (2)$$

$$M_d = M_g \cdot A_u/A_d + M_b \cdot \sigma \cdot A_L/A_d \quad (3)$$

As there is a presence of flow through the impedance tube, the convective terms are incorporated in the wave numbers. The wave numbers (upstream and downstream) with convective effects for the forward and backward travelling waves can be written as:

$$k_u^\pm = k/(1 \pm M_u), \quad k_d^\pm = k/(1 \pm M_d) \quad (4)$$

where, $k = \omega/c$. The acoustic wave fields in the impedance tube are decomposed into forward and backward travelling waves on either side of the acoustic element. The wave field amplitudes A , B , C and D are obtained using transfer functions H_{11} , H_{21} , H_{31} and H_{41} given as^[11] :

$$\begin{bmatrix} A \\ B \\ C \\ D \end{bmatrix} = \begin{bmatrix} e^{-ik_0^+x_1} & e^{ik_0^+x_1} & 0 & 0 \\ e^{-ik_0^+x_2} & e^{ik_0^+x_2} & 0 & 0 \\ 0 & 0 & e^{-ik_d^+x_3} & e^{ik_d^+x_3} \\ 0 & 0 & e^{-ik_d^+x_4} & e^{ik_d^+x_4} \end{bmatrix}^{-1} \times \begin{bmatrix} H_{11} \\ H_{21} \\ H_{31} \\ H_{41} \end{bmatrix} \quad (5)$$

The acoustic pressure and particle velocity at $x = 0$ and d can be written as :

$$p_0 = A + B, u_0 = (A - B)/\rho c, p_d = C + D, u_d = (C - D)/\rho c \quad (6a,b,c,d)$$

For the acoustic load 'a', Eqs. 6(a)-6(d) can be written as :

$$p_{0a} = A_a + B_a, u_{0a} = (A_a - B_a)/\rho c, p_{da} = C_a + D_a, u_{da} = (C_a - D_a)/\rho c \quad (7a,b,c,d)$$

For the acoustic load 'b', Eqs. 6(a)-6(d) can be written as :

$$p_{0b} = A_b + B_b, u_{0b} = (A_b - B_b)/\rho c, p_{db} = C_b + D_b, u_{db} = (C_b - D_b)/\rho c \quad (8a,b,c,d)$$

The subscripts '0' and 'd' represent axial coordinates at $x = 0$ and $x = d$, respectively, where, d is length of the acoustic element. The normal incidence plane wave reflection and transmission coefficients R_n and T_n and the downstream reflection (R_d) at $x = d$ can be written as :

$$R_n = B/A, T_n = C/A, R_d = D/C \quad (9a,b,c)$$

For the acoustic load 'b', Eqs. 6(a)-6(d) can be written as :

$$B = R_n, C = T_n, D = R_d T_n \quad (10a,b,c)$$

Now, Eqs. 6(a)-6(d) can be written in terms of R_n , T_n and R_d using Eqs. 10(a)-10(c) as :

$$p_0 = 1 + R_n, u_0 = (1 - R_n)/\rho c, p_d = T_n(1 + R_d), u_d = T_n(1 - R_d)/\rho c \quad (11a,b,c,d)$$

The acoustic pressure and particle velocity at upstream and downstream end of the acoustic element can be related through the transfer matrix as :

$$\begin{bmatrix} p_0 \\ u_0 \end{bmatrix} = \begin{bmatrix} T_{11} & T_{12} \\ T_{21} & T_{22} \end{bmatrix} \begin{bmatrix} p_d \\ u_d \end{bmatrix} \quad (12)$$

For the loads 'a' and 'b', the above equation can be written as :

$$\begin{bmatrix} p_{0a} & p_{da} \\ u_{0a} & u_{da} \end{bmatrix} = \begin{bmatrix} T_{11} & T_{12} \\ T_{21} & T_{22} \end{bmatrix} \begin{bmatrix} p_{0b} & p_{db} \\ u_{0b} & u_{db} \end{bmatrix} \quad (13)$$

The solution of this equation will give the expressions for the transfer matrix elements as :

$$T_{11} = \frac{p_{0a}u_{db} - p_{0b}u_{da}}{p_{da}u_{db} - p_{db}u_{da}} \quad (14a)$$

$$T_{12} = \frac{p_{0b}p_{da} - p_{0a}p_{db}}{p_{da}u_{db} - p_{db}u_{da}} \quad (14b)$$

$$T_{21} = \frac{u_{0a}u_{db} - u_{0b}u_{da}}{p_{da}u_{db} - p_{db}u_{da}} \quad (14c)$$

$$T_{22} = \frac{p_{da}u_{0b} - p_{db}u_{0a}}{p_{da}u_{db} - p_{db}u_{da}} \quad (14d)$$

A simplified two load transfer matrix approach for the characterization of acoustic elements mean flow

Substitution of Eqs. 11(a)-11(d) in the matrix formulation (Eq. 12) leads to,

$$\begin{bmatrix} 1 + R_n \\ (1 - R_n)/\rho c \end{bmatrix} = \begin{bmatrix} T_{11} & T_{12} \\ T_{21} & T_{22} \end{bmatrix} T_n \begin{bmatrix} (1 + R_d) \\ (1 - R_d)/\rho c \end{bmatrix} \quad (15)$$

The simplification of the above equation results in

$$\begin{bmatrix} 1 \\ 1/\rho c \end{bmatrix} = \begin{bmatrix} -1 & T_{11}(1 + R_d) + T_{12}(1 - R_d)/\rho c \\ 1/\rho c & T_{21}(1 + R_d) + T_{22}(1 - R_d)/\rho c \end{bmatrix} \begin{bmatrix} R_n \\ T_n \end{bmatrix} \quad (16)$$

From the above equation, the expressions for R_n and T_n can be obtained by solving the set of linear equations given as :

$$R_n = \Delta_R \Delta^{-1} \text{ and } T_n = \Delta_T \Delta^{-1} \quad (17)$$

where,

$$\Delta_R = \begin{vmatrix} 1 & T_{11}(1 + R_d) + \frac{T_{12}}{\rho c}(1 - R_d) \\ \frac{1}{\rho c} & T_{21}(1 + R_d) + \frac{T_{22}}{\rho c}(1 - R_d) \end{vmatrix}$$

$$\Delta_T = \begin{vmatrix} -1 & 1 \\ \frac{1}{\rho c} & \frac{1}{\rho c} \end{vmatrix}$$

and

$$\Delta = \begin{vmatrix} -1 & T_{11}(1 + R_d) + \frac{T_{12}}{\rho c}(1 - R_d) \\ \frac{1}{\rho c} & T_{21}(1 + R_d) + \frac{T_{22}}{\rho c}(1 - R_d) \end{vmatrix}$$

The transfer matrix elements T_{11} , T_{12} , T_{21} and T_{22} in Eqs. 14(a)-14(d) are determined using the pressure and velocity values, measured by the microphones for two different loads 'a' and 'b'. The aero acoustic variables A_c , B_c , C_c and D_c with respect to the wave amplitudes A , B , C and D can be represented as :

$$A_c = A(1 + M_u), B_c = B(1 - M_u), C_c = C(1 + M_d), D_c = D(1 - M_d) \quad (18a,b,c,d)$$

$$D = R_d C \text{ with } R_d = -e^{-iL_d(k_i^+ + k_i^-)} \quad (19)$$

where, R_d is the downstream reflection coefficient with flow for open termination. The aero acoustic variables in the Eqs. 18(a)-18(d) along with the Eqs. 10(a)-10(c) can be further written as :

$$A_c = (1 + M_u), B_c = R_n(1 - M_u), C_c = T_n(1 + M_d), D_c = R_d T_n(1 - M_d) \quad (20a,b,c,d)$$

2.1.1 Absorption coefficient

It is the ratio of absorbed to the incident acoustic energy. The substitution of A_c , B_c , C_c and D_c from Eqs. 20(a)-20(d) in the definition of absorption coefficient (α) results in the following expression^[15] :

$$\alpha = 1 - \frac{|B_c|^2 + |C_c|^2}{|A_c|^2 + |D_c|^2} = 1 - \frac{|R_n(1 - M_u)|^2 + |T_n(1 + M_d)|^2}{|(1 + M_u)|^2 + |T_n R_d(1 - M_d)|^2} \quad (21)$$

In the absence of mean flow $M_u = M_d = 0$, the absorption coefficient is given by :

$$\alpha = 1 - \frac{|R_n|^2 + |T_n|^2}{1 + |T_n R_d|^2} \quad (22)$$

The aero acoustic reflection coefficient with flow is given by :

$$R_c = \frac{B_c}{A_c} = R_n \frac{(1 - M_u)}{(1 + M_u)} \quad (23)$$

For the hard-backed termination ($R_d = 1$), the absorption coefficient^[11] is given by

$$\alpha = 1 - |R_c|^2 \quad (24)$$

2.1.2 Transmission loss

The transmission loss is the difference between the sound power that is incident on an acoustic element and that transmitted downstream. For its calculation, an anechoic termination at the downstream end is strictly required^[1, 11]. For the anechoic termination, the downstream reflection coefficient will be equal to zero ($R_d = 0$). The aero acoustic transmission loss is given by :

$$TL_c = 20 \log_{10} \left| \frac{1}{T_c} \right| \quad (25)$$

and the aero acoustic transmission coefficient is given as :

$$T_c = \frac{C_c}{A_c} = T_n \frac{(1 + M_d)}{(1 + M_u)} \quad (26)$$

Now using Eq. (26), aero acoustic transmission loss in the presence of flow can be written as :

$$TL_c = 20 \log_{10} \left| \frac{(1 + M_u)}{T_n(1 + M_d)} \right| \quad (27)$$

In the absence of mean flow ($M_u = M_d = 0$), the aero acoustic transmission loss will be reduced to :

$$TL_c = 20 \log_{10} \left| \frac{1}{T_n} \right| \quad (28)$$

The above expression will be also applicable when the upstream and downstream flow Mach numbers become equal in the absence of a lateral flow entering into the test section. Though the procedure of Two-Load method with the flow is available in the literature it is reproduced in the present work as the steps are to be utilized to simplify it.

2.2 The Simplified Method

This method employs the very same acquired values of pressure as measured by microphones for the standard Two-Load method. For the two different end terminations (loads) 'a' and 'b', the forward and backward travelling wave amplitudes on either side of the specimen A, B, C and D can be related by transfer matrix elements^[13] α , β , γ and δ as follows :

$$\begin{bmatrix} A \\ B \end{bmatrix}_a = \begin{bmatrix} \alpha & \beta \\ \gamma & \delta \end{bmatrix} \begin{bmatrix} C \\ D \end{bmatrix}_a \quad (29a)$$

and

$$\begin{bmatrix} A \\ B \end{bmatrix}_b = \begin{bmatrix} \alpha & \beta \\ \gamma & \delta \end{bmatrix} \begin{bmatrix} C \\ D \end{bmatrix}_b \quad (29b)$$

On solving the above two equations, the transfer matrix elements for wave amplitudes can be written as :

$$\alpha = \frac{A_a D_b - A_b D_a}{C_a D_b - C_b D_a} \quad (30a)$$

$$\beta = \frac{A_b C_a - A_a C_b}{C_a D_b - C_b D_a} \quad (30b)$$

$$\gamma = \frac{B_a D_b - B_b D_a}{C_a D_b - C_b D_a} \quad (30c)$$

$$\delta = \frac{B_b C_a - B_a C_b}{C_a D_b - C_b D_a} \quad (30d)$$

A simplified two load transfer matrix approach for the characterization of acoustic elements mean flow

The solution (R_n and T_n) of Eq. (16) using crammer's rule for a system of linear equations is already represented in Eq. (17). However, the solution can also be represented by solving Eq. (16) as:

$$T_n = \frac{2\rho c}{(1-R_d)(T_{12}+T_{22}\rho c) + \rho c(1+R_d)(T_{11}+T_{21}\rho c)} \quad (31a)$$

$$R_n = \frac{(1-R_d)(T_{12}-T_{22}\rho c) + \rho c(1+R_d)(T_{11}-T_{21}\rho c)}{(1-R_d)(T_{12}+T_{22}\rho c) + \rho c(1+R_d)(T_{11}+T_{21}\rho c)} \quad (31b)$$

Substituting the transfer matrix elements T_{11} , T_{12} , T_{21} and T_{22} from Eqs.14(a)-14(d) in the above equations and thereafter using Eqs. 7(a)-7(d) and Eqs. 8(a)-8(d), results in the normal incidence transmission and reflection coefficient as :

$$T_n = \frac{C_a D_b - C_b D_a}{(A_a D_b - A_b D_a) + (A_b C_a - A_a C_b) R_d} \quad (32a)$$

$$R_n = \frac{(B_a D_b - B_b D_a) + (B_b C_a - B_a C_b) R_d}{(A_a D_b - A_b D_a) + (A_b C_a - A_a C_b) R_d} \quad (32b)$$

On dividing numerator and denominator of Eqs. 32(a) and 32(b) by $C_a D_b - C_b D_a$ and then expressing in terms of the wave amplitude transfer matrix elements using Eqs. 30(a)-30(d) results in:

$$T_n = \frac{1}{\alpha + \beta R_d} \quad (33a)$$

$$R_n = \frac{\gamma + \delta R_d}{\alpha + \beta R_d} \quad (33b)$$

Eqs. 33(a) and 33(b) are the simplified forms of the normal incidence transmission and reflection coefficients. The derived expression for the normal incidence transmission coefficient is different from what deduced by Bonfiglio and Pompoli^[13]. They considered only anechoic-backed termination in their work and also, no term was considered to take into account the effects of downstream duct dimensions. Apart from that, the effect of flow in their formulation was also not investigated. The term R_d in the denominator of Eqs. 33(a) and 33(b) includes the effect of downstream duct length. Substitution of R_d as zero in the Eq. 33(a) for anechoic-backed termination converts it into the expression as derived by Bonfiglio and Pompoli^[13]. As the convective effects are included in the wave numbers, the present simplified method is also applicable in the presence of mean flow.

2.2.1 Absorption coefficient

Now, the simplified expressions for R_n and T_n can be substituted in the expression presented in Eq. (21) to get the absorption coefficient for open-ended and anechoic-backed termination. The absorption coefficient mainly requires R_n , T_n and flow values. The flow values are constant in the respective studies and now other values have the simplified form, which finally simplifies the calculation of absorption coefficient. The calculation of absorption coefficient was not discussed in the work of Bonfiglio and Pompoli^[13]. For the hard-backed end condition ($R_d = 1$), the absorption coefficient^[11] is given in the Eq. (24). The simplified form of the normal incidence reflection coefficient R_n in terms of wave amplitude transfer matrix elements for hard-backed termination can be written by substituting in Eq. 33(b) as :

$$R_n = \frac{\gamma + \delta}{\alpha + \beta} \quad (34)$$

2.2.2 Transmission loss

The substitution of $R_d = 0$ for anechoic termination in Eq. 33(a) results in :

$$T_n = \frac{1}{\alpha} \quad (35)$$

With the use of Eq. (35), Eq. (27) and Eq. (28), the aero acoustic transmission loss with and without flow can be expressed as :

$$TL_c = 20 \log_{10} \left| \frac{\alpha(1 + M_u)}{(1 + M_d)} \right| \quad (36)$$

$$TL_c = 20 \log_{10} |\alpha| \quad (37)$$

The use of wave amplitude transfer matrix elements in the simplified method shortens the procedure of the Two-Load method. All the desired acoustic parameters are shown to be expressible in terms of the wave amplitude transfer matrix elements. The transmission loss requires mainly the term $T_{n'}$, which has a simplified form now and thus finally simplifies its calculation. The wave amplitude transfer matrix elements in Eq. 30(a)-30(d) require A, B, C and D for the two loads ' a ' and ' b ', whose values can be obtained at the very early steps of the Two-Load method procedure.

3. EXPERIMENTAL MEASUREMENTS

Figure 1 depicts the layout of the experimental setup. It comprises of an impedance tube (upstream and downstream section) and a perforated lined section in the middle which is to be tested in the presence of both grazing flow and bias flow. To supply bias and grazing flow in the lined section, blowers are attached to the cavity and to the upstream part of the tube, respectively. The differential pressure gauges are employed to measure the flow rates of grazing and bias flow. Both the flow are controlled by the flow control valves connected in the respective path lines. Loudspeakers along with the amplifiers are placed at the specific locations to produce the SPL of 110-140 dB in the frequency range 400-2500 Hz. The loudspeakers excite sine sweep signals at a sweep rate of 25 Hz/s. The frequency step of 2 Hz is used for the measurements. The pressure-field ¼" microphones are mounted before and after the lined-section at desired locations. These microphones have a sensitivity of 1.6 mV/Pa with frequency ranging up to 70 kHz and are calibrated using a calibrator of calibration pressure 114 dB at 1000 Hz frequency. A data acquisition unit (B&K 3160-A-042) is connected to the amplifier and all the microphones to excite signals and measure pressure data, respectively. The dimension of the impedance tube are mentioned in Table 1. For the estimation of the acoustic parameters, the downstream duct length (L_d) is taken as 0.1 m with open ended-termination. The acoustic parameters absorption coefficient and transmission loss are used to get the behaviour of the test elements (liner and compact acoustic filter). The lined section placed in the middle of upstream and downstream section of the impedance tube as shown in Fig. 2 can be replaced by any other acoustic element under investigation.

Table 1. Impedance tube geometric details

Parameter	Length (mm)	Diameter (mm)
Upstream Tube	1500	80
Liner	200	80
Cavity	200	150
Downstream Tube	500	80

Figure 2 depicts the schematic of the test section of the measurement setup. The test setup as shown in Fig. 1, is similar to that investigated by Jha *et al.*[15]. In the schematic, the microphones are shown to be mounted closer to the lined-section, however, the measurements were also conducted by shifting them at a relatively distant location. The variation thus observed were negligible for practical purposes. Further, another acoustic element 'compact acoustic filter' is also considered to get transmission loss in order to further demonstrate the capability of the simplified model. There may be the cases when there is no any bias flow. For such cases the compact acoustic filter is considered as an example and mounted in between

A simplified two load transfer matrix approach for the characterization of acoustic elements mean flow

the upstream and downstream section of another impedance tube of diameter 40 mm. Figure 3 presents the front view of the compact acoustic filter, geometric details of which can be found in the ref. [16].

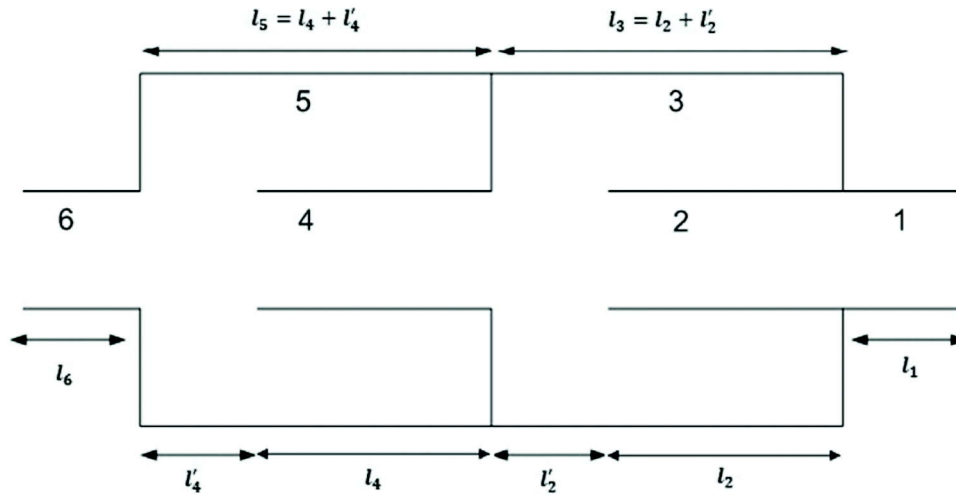


Fig. 3. Schematic of the compact acoustic filter¹⁶

4. RESULTS

This section presents the results of acoustic parameters plotted using the standard Two-Load method and the present simplified method. The comparative results are plotted for different end-terminations to demonstrate the capabilities of the present method. The results are presented for two different acoustic elements bias flow perforated liner and a compact acoustic filter which is made up of two cavities.

4.1 Perforated liner

Figures (4)-(6) show the absorption coefficient of a liner measured by the existing Two-Load method and the present simplified method. Measurements are conducted at different flow conditions considering different end termination conditions.

4.1.1 Absorption coefficient

Figure (4) and (5) show the measured absorption coefficient considering an open-ended termination in the presence and absence of mean flow, respectively. For the calculation of absorption coefficient, Eq. (21) is used. Figure 4 shows the absorption coefficient of liner in the presence of combined grazing-bias flow with open-ended termination. Bias flow contributes to the broadband sound absorption over the entire range of frequency. However, the absorption minima or trough is the result of standing wave formation at the frequency corresponding to the combined length of the lined-section and the downstream duct. In the absence of bias and grazing flow, absorption is lower and maxima are there at discrete frequencies as shown in Fig. 5.

In the case of hard-backed termination, the absorption coefficient is calculated and shown in Fig. 6. For this end-condition, Eq. (24) is used to calculate the absorption coefficient. The normal incidence reflection coefficients in the Eq. (17) for standard method and Eq. (34) for the simplified method, are used to get the absorption coefficient for the hard-backed termination. The absorption curve has minima and maxima at discrete frequencies.

4.1.2 Transmission loss

For the liner, without and with mean flow, the transmission loss is calculated and shown in Figs. (7) and (8), respectively. For the calculation of transmission loss, an anechoic termination is considered as

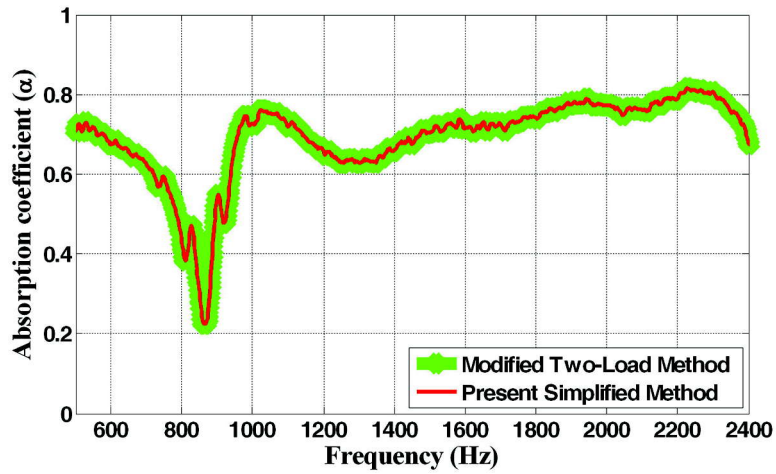


Fig. 4. Measured absorption coefficient of the liner at $M_g = 0.05$, $M_b = 0.1$, thickness = 1.6 mm, hole diameter = 3.2 mm, porosity = 2.4% with open-ended termination

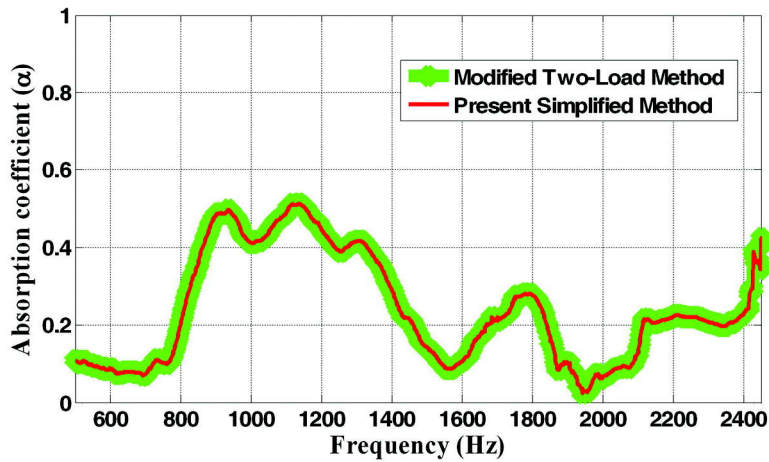


Fig. 5. Measured absorption coefficient of the liner at $M_g = 0.0$, $M_b = 0.0$, thickness = 1.6 mm, hole diameter = 3.2 mm, porosity = 2.4% with open-ended termination

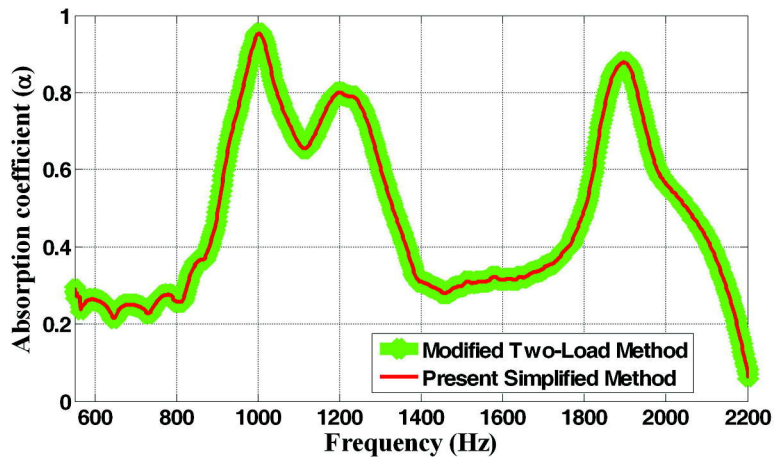


Fig. 6. Measured absorption coefficient of the liner at $M_g = 0.0$ and $M_b = 0.0$ thickness = 1.6 mm, hole diameter = 3.2 mm, porosity = 2.4% with hard-backed termination

the necessary requirement. Figure 7 shows the transmission loss of a liner without flow. The local and global maxima for transmission loss are there at discrete frequencies. With flow, the transmission loss curve is observed to be raised broadband as shown in Fig. 8. Also, the maxima is observed to be raised.

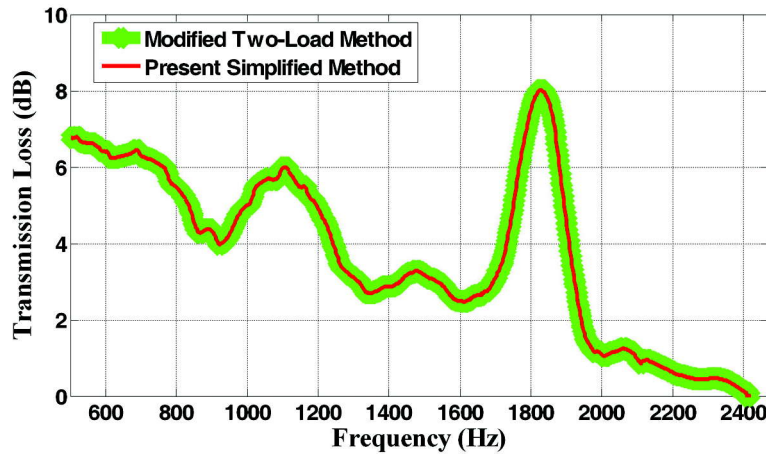


Fig. 7. Measured Transmission loss of a liner of porosity = 3%, hole diameter = 5 mm, thickness = 2 mm at $M_g = M_b = 0$ for anechoic termination

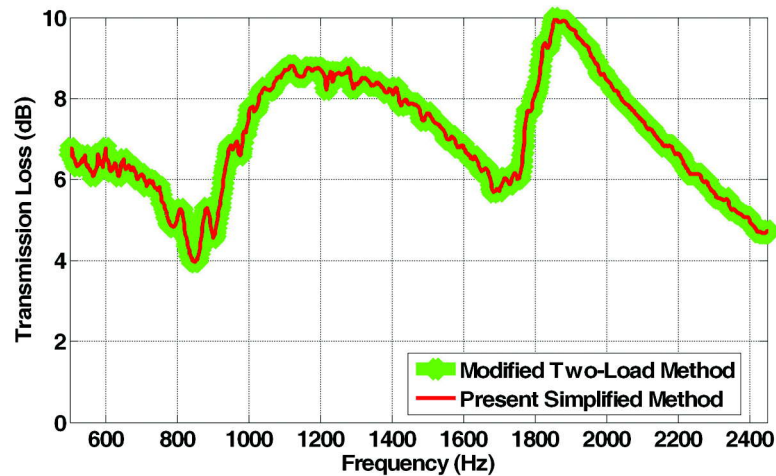


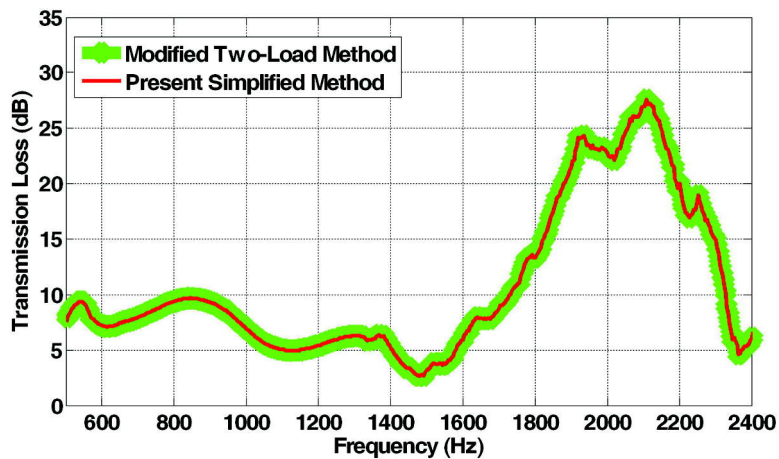
Fig. 8. Measured Transmission loss of a liner of porosity = 3%, hole diameter = 5 mm, thickness = 2 mm at $M_g = 0.05$ $M_b = 0.1$ for anechoic termination

4.2 Compact acoustic filter

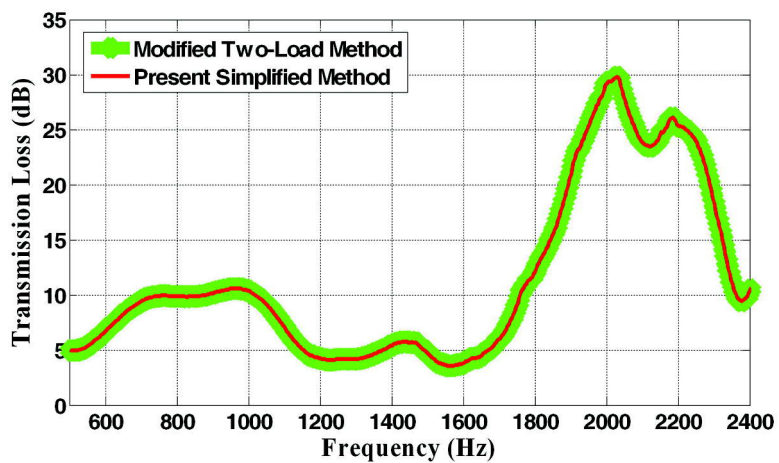
4.2.1 Transmission loss

The transmission loss of compact acoustic filter is calculated and compared using both the method as shown in Figs. 9(a) and 9(b) for with and without flow, respectively. The schematic of the filter investigated is presented in Fig. 3. The transmission loss for with and without mean flow has peaks, which corresponds to the presence of cavity in the filter. The frequency of maximum transmission loss has its dependence on the cavity length.

In Figs. (8) and (9), Eqs. (27) and (28) are used to calculate the transmission loss for the Two-Load method, while Eqs. (36) and (37) are used for the present simplified method. The acoustic parameters absorption coefficient and transmission loss of a perforated liner are calculated with and without mean



(a)



(b)

Fig. 9. Measured Transmission loss of muffler (a) $M_g = 0.06$, (b) $M_g = 0.0$ with anechoic termination

flow, while only the transmission loss is calculated for compact acoustic filter. All the plots for the comparison of absorption coefficient and transmission loss show no variation and coincide for the entire frequency range of investigation in both the methods. The pressure measurements used for the simplified method are the same as acquired for the standard Two-Load method. All the types of end condition have been considered and parameters are plotted with those conditions. The calculation of the absorption coefficient can be done for all the types of end conditions, while transmission loss is calculated for anechoic termination only.

5. CONCLUSION

In this paper, a method is presented which is based on the simplification of the standard Two-Load method. It directly relates the complex wave amplitudes of the measured pressure at four microphone locations through a transfer matrix. The acoustic parameters are shown to be expressible in terms of the transfer matrix elements. Due to the direct relationship between pressure and wave amplitudes, this method becomes less complicated than the standard Two-Load method and involves lesser number of steps to calculate the parameters in comparison to the standard method. The present technique has not

incorporated any special considerations than that of a standard Two-Load method. The inclusion of convective terms in the wave number and use of aero acoustic variables enables the present method to be applicable in mean flow regime also. The transmission loss and absorption coefficient of acoustic elements by the present method have been calculated and compared with the standard method in order to demonstrate the capabilities of the simplified method. The method revealed good agreement with the Two-Load method for both flow and non-flow cases. As this method uses the same pressure measurements by four microphones as in the standard method, there is no practical restriction on the type of acoustic element to be tested using the proposed method. The comparative results are overlapping or in exact match, which reflects that the present method only simplifies the standard method. The present method does not point out any discrepancy and also does not point out any modification to the standard method. The new method presented agrees well with standard Two-Load method on the entire frequency range and may help designers to consider this an alternative to the standard Two-Load technique for being less complicated.

6. REFERENCES

- [1] M.L. Munjal, 1987. *Acoustics of Ducts and Mufflers. John Wiley and Sons.*
- [2] I.J. Hughes and A.P. Dowling, 1990. The absorption of sound by perforated linings. *J Fluid Mech.* 1990; 218:299-335. doi:10.1017/S002211209000101X
- [3] T.H. Melling, 1973. An impedance tube for precision measurement of acoustic impedance and insertion loss at high sound pressure levels. *J. Sound Vib.*; **28**(1), 23-IN1. doi:https://doi.org/10.1016/S0022-460X(73)80016-1
- [4] S.L. Yaniv, 1973. Impedance tube measurement of propagation constant and characteristic impedance of porous acoustical material. *J. Acoust Soc Am.* 1973; **54**(5), 1138-1142. doi:10.1121/1.1914360
- [5] A.F. Seybert and D.F. Ross, 1977. Experimental determination of acoustic properties using a two-microphone random excitation technique. *J. Acoust Soc Am.*; **61**(5), 1362-1370. doi:10.1121/1.381403
- [6] J.Y. Chung and D.A. Blaser, 1980. Transfer function method of measuring in-duct acoustic properties. I. Theory. *J. Acoust Soc Am.*; **68**(3), 907-913. doi:10.1121/1.384778
- [7] J.Y. Chung and D.A. Blaser, 1980. Transfer function method of measuring in-duct acoustic properties. II. Experiment. *J. Acoust Soc Am.*; **68**(3), 914-921. doi:10.1121/1.384779
- [8] To CWS and A.G. Doige, 1979. A transient testing technique for the determination of matrix parameters of acoustic systems, I: Theory and principles. *J. Sound Vib.*; **62**(2), 207-222. doi:https://doi.org/10.1016/0022-460X(79)90022-1
- [9] To CWS and A.G. Doige, 1979. A transient testing technique for the determination of matrix parameters of acoustic systems, II: Experimental procedures and results. *J. Sound Vib.*; **62**(2):223-233. doi:https://doi.org/10.1016/0022-460X(79)90023-3
- [10] T.Y. Lung and A.G. Doige, 1983. A time-averaging transient testing method for acoustic properties of piping systems and mufflers with flow. *J. Acoust Soc Am.*; **73**(3), 867-876. doi:10.1121/1.389056
- [11] ASTM E2611-09, Standard Test Method for Measurement of Normal Incidence Sound Transmission of Acoustical Materials Based on the Transfer Matrix Method. *ASTM International, West Conshohocken, PA*, 2009.
- [12] M.L. Munjal and A.G. Doige, 1990. Theory of a two source-location method for direct experimental evaluation of the four-pole parameters of an aeroacoustic element. *J. Sound Vib.*; **141**(2), 323-333. doi:https://doi.org/10.1016/0022-460X(90)90843-O
- [13] P. Bonfiglio and F. Pompoli, 2008. A single measurement approach for the determination of the normal incidence transmission loss. *J. Acoust Soc Am.*; **124**(3), 1577-1583. doi:10.1121/1.2951605

- [14] D. Das, U. Chhibber and R.N. Hota, 2019. Modification of Two-Load Method for Measuring Acoustic Properties with Mean Flow- *Advances in Interdisciplinary Engineering*. In: M. Kumar, R.K. Pandey, V. Kumar, eds. Singapore: *Springer Singapore*; pp. 579-587.
- [15] N.K. Jha, D. Das, A. Tripathi and R.N. Hota, 2019. Acoustic damping-: Analytical prediction with experimental validation of mixed porosity liners and analytical investigation of conical liners. *Appl Acoust.*; **150**, 179-189. doi:10.1016/j.apacoust.2019.02.006
- [16] U. Chhibber, R. Kumar, S. Haldar and R.N. Hota, 2018. Design and analysis of a compact acoustic filter for broad band noise absorption. *Appl Acoust.*; **140**, 30-38. doi:https://doi.org/10.1016/j.apacoust.2018.05.011

Performance evaluation and comparison of measured sound insertion loss of corrugated plates

S.S. Pathan¹ and D.N. Manik²

¹L.D. College of Engineering - Ahmedabad, Gujarat-380015, India

²Indian Institute of Technology, Bombay, Mumbai-400076, India

e-mail: pathan_ss@yahoo.co.in

[Received: 04-02-2020; Revised: 16-03-2020; Accepted: 17-03-2020]

ABSTRACT

To reduce structureborne sound radiated by machines such as generators, gas turbines and compressors, etc. external covers are used which are generally constructed from plates and shells. But these external covers also radiate airborne sound when excited by structureborne sound. In addition, depending on the insertion loss of these plate enclosures, a part of the airborne sound from the machines enclosed by them is transmitted across to the external sur-rounding. Providing local stiffeners on these covers improves their insertion loss and reduces their sound radiating capability to some extent. But that is not sufficient. Hence, in the present work, the flat nature of plates was changed by discontinuities introduced on flat bare plates through attaching stiffeners. To obtain various corrugated configurations, triangular stiffeners were attached on flat bare rectangular plates. Several test samples were fabricated by providing various geometric configurations of corrugations on flat plates for exploring the possibility of increasing sound insertion loss. This was verified through experiments performed in an anechoic room using a source of airborne sound. Initially, sound insertion loss was measured for a set of corrugated plates comprising of triangular prismatic cavities, formed between the flat surface of plates and inverted 'V' shaped stiffeners. Similar experiments were performed for another set of corrugated plates in which acoustic cavities were avoided, and sound insulation performance of both the set of corrugated plates was compared. The size of the plates for the experiments was kept small within manageable limits for ease in conducting experiments. Significant improvement in the sound insertion loss was observed for both sets of corrugated plates, as compared to a flat bare plate of the same overall dimension.

NOMENCLATURE

2A-10A	Set A corrugated plates 2A - 10A
2B-10B	Set B corrugated plates 2B - 10B
\bar{L}_p	Spatial average sound pressure level
\bar{L}_{p_i}	Local spatial average sound pressure level (With plate insertion)
\bar{L}_{p_n}	Local spatial average sound pressure level (Without plate insertion)
n_m	The number of measurements
t_c	Thickness of corrugation

ABBREVIATION

BEM	Boundary Element Method
FEM	Finite Element Method
IL	Insertion Loss
SEA	Statistical Energy Analysis
SPL	Sound Pressure Levels
STL	Sound Transmission Loss

1. INTRODUCTION

Most machine structures can be presented in terms of an assemblage of flat plates; for example, casings of machinery, automobiles, aerospace vehicles, ship hulls and decks, submarines, large industrial installations, etc. In these constructions, vibrating flat plates become the sound source when excited by external disturbances. Sound is radiated because of the action of solid vibrating plate surfaces upon the surrounding fluid which comes in contact with such vibrating plates. To study the vibro-acoustic behaviour of plates, accurate prediction and validation of sound transmission through them helps a designer to treat noise and vibration problems during the preliminary stages of design. Because of varying geometrical forms, constructional features and material properties, sound transmission prediction from such vibroacoustic structures becomes extremely difficult. This is due to the fact that the mathematical modelling techniques, such as finite element method and boundary element method, which are used to predict the dynamic behaviour of such structures, are uncertainty prone due to damping distribution, boundary conditions, tolerance and structural joint properties. Even with the availability of sophistication in respect of computational software and hardware, large amount of model preparation and computation time pose infeasibility of these methods requiring large amount of data to be handled and processed. Experimental investigation thus helps one to correlate theoretical outcomes and validate the prediction results.

Various theoretical and experimental investigations have been carried out on sound transmission through isotropic single and double panel constructions in the past. For example, for a transmission suite comprising of a room-panel-room, Crocker and Price presented general power flow relationships^[1]. The power flow between two rooms was defined as the flow between non-resonant modes, when there are no modes excited in the panel in the frequency band under consideration. The Sound Transmission Loss (STL) was predicted for the radiation resistance and the vibration amplitude of a partition using Statistical Energy Analysis (SEA). Renji proposed a direct non-resonant coupling loss factor between a source room and a partition, and suggested a modified-SEA model to predict the non-resonant energy transfer between rooms and partition, by considering the sound transmission through a single-leaf aluminum plate^[2]. Cheng and Shyu^[3] extended the work of Renji^[2] to further investigate sound transmission through double & triple leaves and estimated non-resonant energy transfer using a non-resonant coupling loss factor between a cavity and partition. Renji *et al.*^[4] verified the modified SEA, which they had developed earlier, by acoustically exciting an aluminum plate in a reverberation chamber and estimated the response of the panels. Later, Cheng *et al.*^[5] showed that the non-resonant response of the panel is insignificant at frequencies below the critical frequency, and through an experimental study, they suggested that the non-resonant response component should be included in the estimated response for enhancing prediction accuracy.

Sometimes, large panels are made out of thin sheets and they have very low bending stiffness. Hence, forming corrugations on thin flat plates is a very common practice to improve their static bending stiffness and buckling resistance. Many forms of partition or enclosures employed in practice differ from plain, homogeneous and uniform plates for reasons of weight, stiffness to weight ratio, static stiffness or sometimes noise control requirements. Also, ribs are directly attached to thin flat plate structures, or alternatively, beads are introduced to increase their stiffness. This makes them orthotropic, giving higher bending stiffness in the two orthogonal directions. The critical frequency for bending waves travelling in

the direction parallel to the corrugations is much lower in comparison to that of a uniform flat plate of equal thickness. Onsay *et al.*[6] have analysed the vibro-acoustic behaviour to predict radiation factor and STL of bead stiffened flat panels by altering the design parameters, using a hybrid FEA-SEA approach. In their investigation, they tried to change the bending stiffness of such beaded plates but the thickness of corrugation was not varied.

The influence of stiffening effect on corrugated steel structures was studied by Cordonnier *et al.*[7]. They determined critical frequencies of orthotropic corrugated plates and their STL was evaluated from intensity measurements.

The double-panel partition or double wall structures are sometimes used for various applications. The construction is based on an air cavity formed between two parallel plates and the cavity, either completely or partially filled with sound absorbing material. Such structures are found in aerospace applications, automotive industry and building constructions because of their lightness and high STL[8,9].

Recently, aerospace structures were modelled using composite sandwich constructions to provide strength to the base structure. However, such type of composite sandwich structures suffer from the disadvantage of poorer sound transmission properties than metals[9].

No rigorous work has been carried out thus far on the vibro-acoustic analysis of stiffened plates wherein geometrical parameters of stiffeners can be varied and tuned to investigate their effect on the dynamic nature of flat surfaces of plates. Nevertheless, the significance of studying the dynamic behaviour of stiffened plates is cited in many texts, but only in qualitative terms. Thus, the dynamic behaviour of flat rectangular bare plates can be altered by attaching stiffeners of varying thickness and included angles and tuning geometries of stiffened plates with a view to reduce sound radiation factor and to improve sound insulation performance. The present work is an attempt to alter the dynamic behaviour of flat rectangular plates by modifying them to obtain a corrugated configuration. Such designs of corrugations of various geometric configurations on flat bare plates were considered to get different corrugated plates. Several test samples were fabricated by providing various geometric configurations of corrugations on flat plates for exploring the possibility of increasing sound insertion loss which was verified through experiments performed in an anechoic room using a source airborne sound. Initially, sound insertion loss was measured for a set of corrugated plates comprising of triangular prismatic cavities, formed between the flat surface of plates and inverted 'V' shaped stiffeners. Similar experiments were performed for another set of corrugated plates in which acoustic cavities were avoided, and sound insulation performance of both the set of corrugated plates was compared with reference to the flat bare rectangular plates. The geometrical details of fabricated corrugated plates and procedure of conducting experiments for evaluating sound insulation performance is discussed in the next section.

2. EXPERIMENTAL SETUP AND PROCEDURE FOR INSERTION LOSS MEASUREMENT

This section outlines the methodology adopted to perform experiments for the measurement of sound insertion loss of plates. It begins with the description of fabricated corrugated plates. Then the experimental procedure is discussed followed by results and discussion on sound insulation performance.

With a view to capture an insight of the sound insulation behaviour of corrugated plates, a bare plate of size 0.48 m × 0.3 m × 0.0035 m was considered for the convenience of conducting experiments. Different corrugated configurations were fabricated, by modifying bare plates with the help of inverted triangular shaped fabricated stiffeners of varying included angles and thicknesses.

The corrugation configurations are enlisted in Table 1 for two different sets of plates. The plate parameters were so chosen as to get varied corrugation configurations in order to capture the wide range of insertion loss performance of plates. Figures 1(a) & 1(b) show set A & set B corrugated plates respectively, fabricated for performing experiments. The experiments consisted of separate measurements of sound insertion loss of total 19 plates (*i.e.* the flat bare plate 1 and all the set A & set B corrugated plates).

Table 1. Geometrical parameters of fabricated Set A corrugated plates used for experimentation.






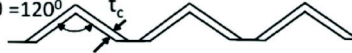
Plate	Stiffener included angle	Stiffener thickness (mm)	Geometrical configuration details of MS plates
1	Flat bare plate		
2A	700	1.5	 Plate 2A : $t_c = 1.5$ mm Plate 3A : $t_c = 2$ mm Plate 4A : $t_c = 3$ mm
3A	700	2	
4A	700	3	
5A	900	1.5	 Plate 5A : $t_c = 1.5$ mm Plate 6A : $t_c = 2$ mm Plate 7A : $t_c = 3$ mm
6A	900	2	
7A	900	3	
8A	1200	1.5	 Plate 8A : $t_c = 1.5$ mm Plate 9A : $t_c = 2$ mm Plate 10A : $t_c = 3$ mm
9A	1200	2	
10A	1200	3	

Table 2. Geometrical parameters of fabricated Set B corrugated plates used for experimentation.

Plate	Stiffener included angle	Stiffener thickness (mm)	Geometrical configuration details of MS plates
1	Flat bare plate		
2A	700	1.5	 Plate 2B : $t_c = 1.5$ mm Plate 3B : $t_c = 2$ mm Plate 4B : $t_c = 3$ mm
3A	700	2	
4A	700	3	
5A	900	1.5	 Plate 5B : $t_c = 1.5$ mm Plate 6B : $t_c = 2$ mm Plate 7B : $t_c = 3$ mm
6A	900	2	
7A	900	3	
8A	1200	1.5	 Plate 8B : $t_c = 1.5$ mm Plate 9B : $t_c = 2$ mm Plate 10B : $t_c = 3$ mm
9A	1200	2	
10A	1200	3	

Sound insertion loss measurements, on two sets (set A and set B) of corrugated plates and a flat bare plate for comparison, have been carried out in an anechoic chamber of size 3.6 m × 3.6 m as shown in Figs. 2 & 3. The inside of anechoic chamber consists of wedge blocks, on all six sides of the chamber, made of polyurethane having a density of 30 kg/m³.

As an airborne sound source, a marble cutter running on no load was positioned centrally inside a wooden enclosure and an arrangement was made to insert the plates at the opening of this enclosure. The wooden enclosure was properly sealed using a sealant. The sound in the test section was measured by using an array of four B & K 4939 free-field condenser type microphones of size 6.53 mm (1/4") having a flat frequency response of 4 Hz to 100 kHz.



Fig. 1. Fabricated plates for measuring insertion loss: (a) Set A corrugated plates, (b) Set B corrugated plates

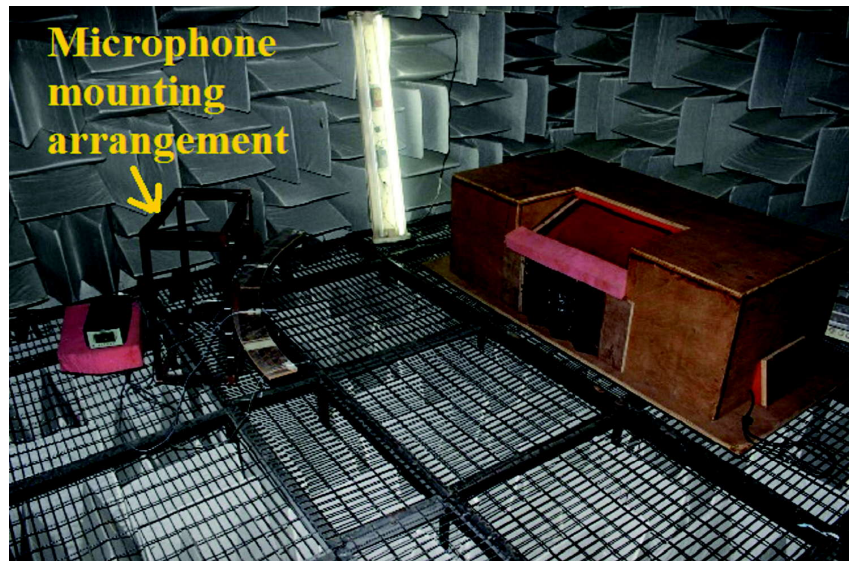


Fig. 2. Setup for insertion loss measurement

As shown in Fig. 3, the microphones were suitably placed on the curved wooden frame, which was then clamped on a pre-fabricated frame. The microphones were attached with a B & K type 2970 pre-amplifier and were powered by four channel NEXUS type 2690-OS2 signal conditioning amplifier. The output was then fed to the computer through a NI DAQ system PCI 4462. The plywood sheet of 12 mm thickness was placed underneath the wooden enclosure containing a marble cutter as sound source and the experiments were performed for the measurement of sound pressure level (SPL) for calculating the insertion loss of the plates. Sound Pressure Levels were calculated for the cases with and without inserting the plates.

The insertion loss was evaluated for one-third octave band frequencies for each plate using Eq. (1) given by Aygun and Attenborough^[10] and then with the help of standard A-weighting values for the one-third octave band centre frequencies, corrected A-weighted sound insertion loss (in dB) was calculated.

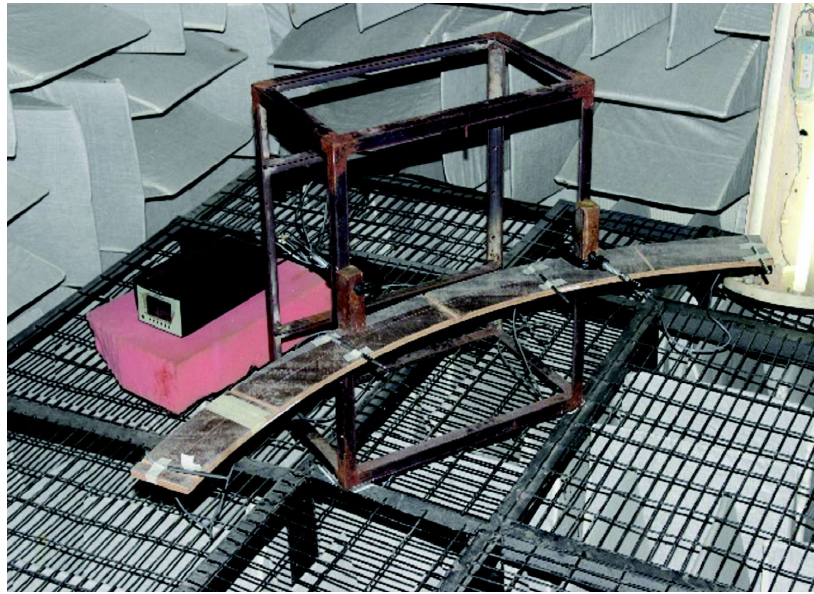


Fig. 3. Microphone mounting arrangement

$$IL = \bar{L}_{p_{ii}} - \bar{L}_{p_i} \quad (1)$$

In Eq. (1), \bar{L}_{p_i} is the spatial average sound pressure level in the frequency band in the test anechoic room, when the plates were inserted, and $\bar{L}_{p_{ii}}$ is the spatial average sound pressure level in the frequency band in the anechoic room, when no plate was inserted.

The spatial average SPL was calculated by measuring the local SPL for all plates at three different positions of the microphone array by varying the height of the curved wooden frame [shown in Fig. 3] which was repeatedly clamped on the fabricated frame placed in front of the wooden enclosure.

The spatial average sound pressure level, \bar{L}_p , in dB, was calculated from the local sound pressure levels, L_{p_i} , using Eq. (2) given by^[10]:

$$\bar{L}_p = 10 \log \left[\frac{1}{n_m} \sum_{i=1}^m 10^{\frac{L_{p_i}}{10}} \right] \quad (2)$$

where n_m is the number of measurements. The background noise inside the anechoic room at each measurement position was also measured by measuring the SPL with the noise source turned on and off. The calibration of microphones was carried out first and the microphone signals were captured using data acquisition system and later analysed in one-third octave band for all the set of experiments. Sound pressure levels were calculated from microphones for the cases when plates were inserted and also for the cases without inserting plates. The insertion loss was calculated for one-third octave band frequencies for each plate. With the help of standard 'A'-weighting values for the one-third octave band centre frequencies, corrected A-weighted sound insertion loss (in dB) was calculated.

2.1 Results and Discussion

Because of low frequency threshold of the anechoic chamber, the measured insertion loss for frequencies more than 200 Hz were plotted. The results of 'A'-weighted measured insertion loss were compared with the flat bare plate, which are presented in Figs. 4-12.

The theoretically calculated critical frequency of a flat bare plate is 3358 Hz. As the stiffeners are incorporated to the flat bare plate, the behaviour of the corrugated plate becomes orthotropic, *i.e.* there

are two critical frequencies corresponding to the direction of bending wave travel. Due to the effect of corrugation and added stiffness, the critical frequencies shift towards the low frequency which are clearly observed. Based on the expressions given by Cordonnier^[7] for evaluating critical frequency of the trapezoidal corrugation, bending stiffness were obtained for the principal x & y directions. The critical frequencies were calculated for Set A corrugated plates with some modifications incorporated corresponding to geometry of the present configuration, which are presented in details in the thesis^[12]. Similarly, for Set B corrugated plates, the critical frequencies were calculated using the "planification approach" presented by Piscoya *et al.*^[13].

The theoretical critical frequencies of set A plates lie between 916 Hz and 1409 Hz as the lowest critical frequency, whereas highest calculated critical frequency range lie between 1371 Hz and 2314 Hz. Similarly, the theoretical critical frequencies of set B plates lie between 1632 Hz and 1660 Hz as the lowest critical frequency, whereas highest computed theoretical critical frequency range lie between 3343 Hz and 3392 Hz. The critical frequency depends upon the flexural rigidity and surface mass density of the plates. The critical frequency will be lower in the direction of greatest stiffness. Set A plates have more variation in surface mass density and bending stiffness as compared to Set B plates. Hence, for Set A corrugated plates, wide variation between the lower and upper values of critical frequencies is observed, whereas a very little variation is found for Set B corrugated configurations. These variations in calculated critical frequencies of corrugated plates are due to changes in both stiffener thickness and included angles.

The critical frequency dips observed in the measured insertion loss curves are closely matching to the theoretically evaluated values. The results obtained clearly indicate that the stiffeners improve sound insertion loss at almost in the entire frequency range except at and just below the coincidence range, *i.e.* between 400 Hz and 1 kHz, where a little deterioration is observed. This behaviour can be well explained by the effect of introduced low wavenumber components due to the effect of boundaries of stiffeners, which then subsequently increase the sound radiation factor at the sub-critical frequency.

As the radiation factor is equivalent to a normalized sound power with respect to the specific acoustic impedance of the surrounding media, plate area and vibrating normal velocity of the plate, it can be seen as a measure of the sound radiation in dependence of the geometry of the stiffeners placed on plate and their relative spacing. Hence, while designing corrugated plate structures proper care must be taken to select stiffener, their geometry and placing.

The variation in corrugation configuration of two sets of plates signifies the role of the radiation efficiency, just below the coincidence. At the critical frequency, *i.e.* when the plate bending wavelength

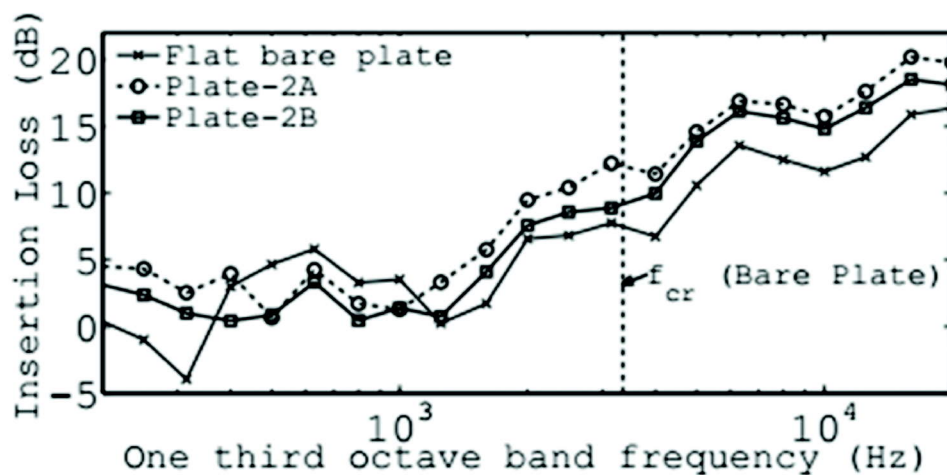


Fig. 4. Comparison of measured one-third octave band insertion loss of corrugated plates 2A and 2B with the flat bare plate

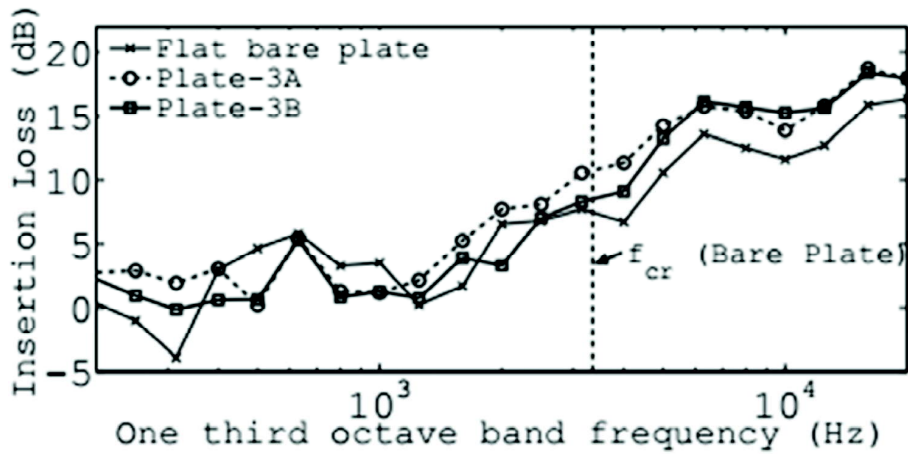


Fig. 5. Comparison of measured one-third octave band insertion loss of corrugated plates 3A and 3B with the flat bare plate

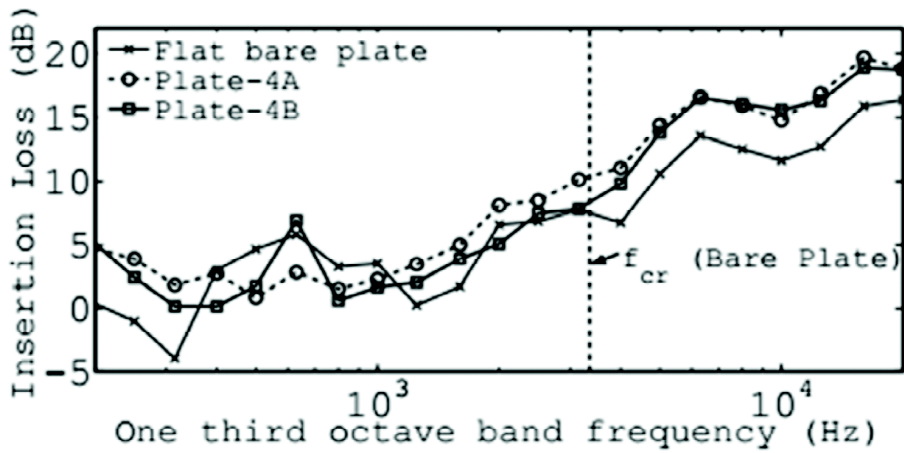


Fig. 6. Comparison of measured one-third octave band insertion loss of corrugated plates 4A and 4B with the flat bare plate

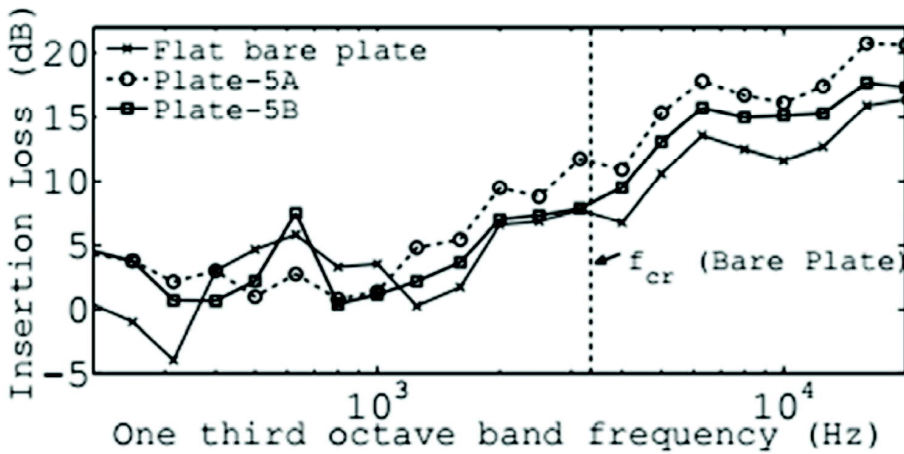


Fig. 7. Comparison of measured one-third octave band insertion loss of corrugated plates 5A and 5B with the flat bare plate

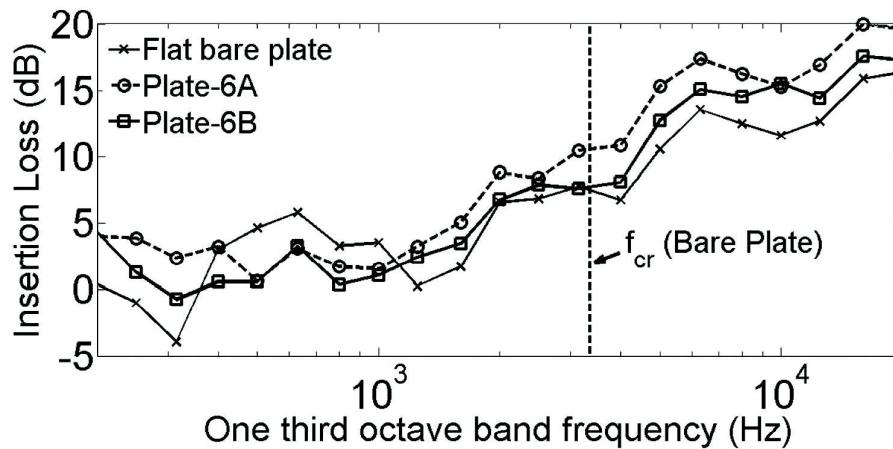


Fig. 8. Comparison of measured one-third octave band insertion loss of corrugated plates 6A and 6B with the flat bare plate

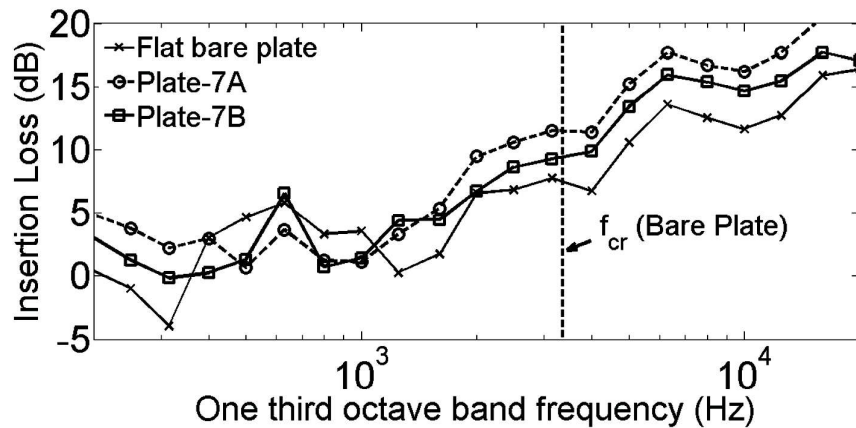


Fig. 9. Comparison of measured one-third octave band insertion loss of corrugated plates 7A and 7B with the flat bare plate

equals the trace wavelength of acoustic waves, the plate vibration amplitude increases and the radiation efficiency also increases. Thus, at the critical frequency the sound transmission is high due to resonant modes around a band centred at this coincidence frequency. This behaviour is dominant for set A plates than set B plates. This is due to the radiation efficiency of the former is relatively more than that of the latter due to extra edges in set A plates as compared to set B corrugated plates and subpanels type plate segments formed due to corrugation.

As the frequency range between 400 Hz and 1 kHz being the region where edge modes contribute to sound radiation, more sound is radiated by set A plates than set B plates and hence sound insulation performance is little poor for set A plates at and just below the coincidence region due to resonant sound transmission which is clearly seen in Figs. 4-12.

In the frequency region well below the coincidence, *i.e.* up to 400 Hz, it is found that the insertion loss of corrugated plates is more as compared to a flat bare plate. This is due to the modes which are not resonant in this frequency band. This is because the vibration amplitude of resonant modes is low and the radiation efficiency is also low because of stiffening effect. However, a little deterioration at 315 Hz one-third octave frequency band has been observed. This can be interpreted based on the fact that low

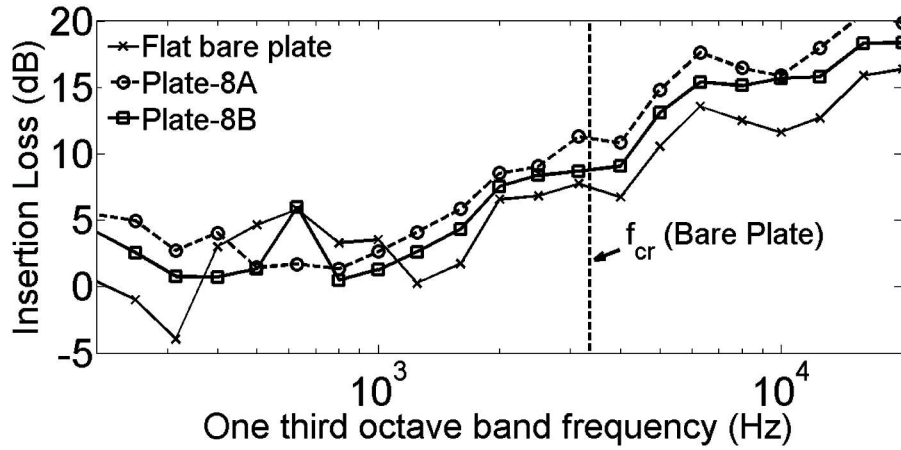


Fig. 10. Comparison of measured one-third octave band insertion loss of corrugated plates 8A and 8B with the flat bare plate

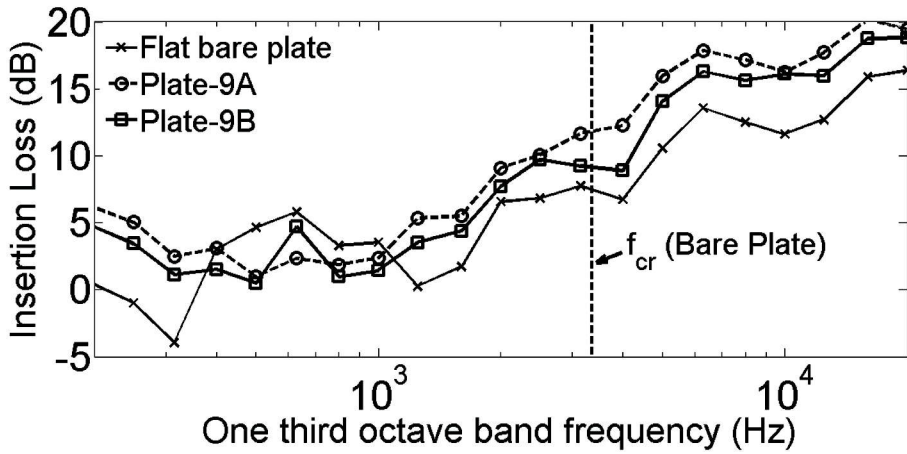


Fig. 11. Comparison of measured one-third octave band insertion loss of corrugated plates 9A and 9B with the flat bare plate

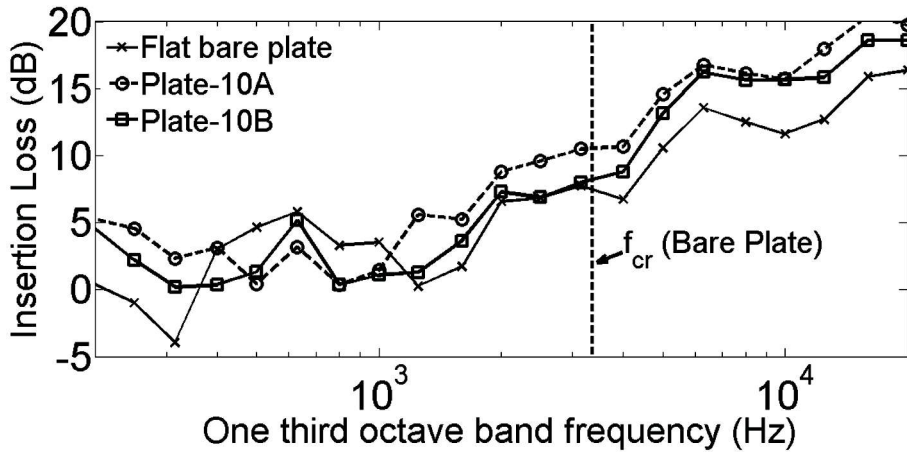


Fig. 12. Comparison of measured one-third octave band insertion loss of corrugated plates 10A and 10B with the flat bare plate

frequencies are governed by global modes and, medium and high frequencies are governed by periodic and local modes of corrugated plates. This transition is responsible for increased sound transmission, due to increased radiation efficiency of the small segments (formed due to stiffener placement) of corrugated plates at the so-called frequency of transition. Therefore, the dips observed in the insertion loss around 400 Hz frequency region may be due to this transition between global and local modes.

The enhancement of sound insertion loss due to corrugation is very distinctly observed at higher frequencies. Above 1 kHz frequency, all the set A plates show better sound insulation performance as compared to set B plates and even much better than a flat bare plate, due to reduced sound radiation efficiency of corrugated plates as compared to a flat bare plate. The insertion loss at higher frequencies is more dominant for set A plates than set B plates due to radiation efficiency of former being less at higher frequencies. Because of increase in stiffness of set A plates, the resonance frequencies shift to higher frequencies thus reducing the local resonance effect and hence improve sound insulation performance. Above 4 kHz frequency, the insertion loss separation between the set A plates and a flat bare plate increases.

In both sets of corrugated plates, the stiffeners are placed symmetrically and also this arrangement of stiffeners forms a periodic structure. A very significant effect of the periodicity of stiffeners is to divide the frequency range into a sequence of pass bands, where vibration can propagate, and stop bands, where it cannot. For the peaks and dips in the insertion loss, this pattern of stop and pass bands is responsible, which can be clearly seen in the results. Especially in the high frequency region, the oscillations above the coincidence are due to these pass-stop frequency bands. Similar results are also reported by Sylvia and Hull^[11] who developed a model for a flexural plate reinforced by an infinite equal spaced ribs and analysed stop-pass band behaviour of stiffened plates.

The periodically distributed stiffeners with relatively narrow separations restrict the deformation of the corrugated plates, offering therefore the corrugated plates a larger stiffness than that of those plates with stiffener spacing being wider. Better sound insulation performance can be clearly seen for the plate numbers in order: 2A-4A-3A (refer Figs. 4-6). Similar observations were made for the rest of the plates (refer Figs. 7-12), which signifies that not only the spacing between the stiffeners that plays role in sound insulation, but also the thickness of stiffener is important as far as vibro-acoustic behaviour is concerned.

An overall gain in sound insertion loss of 5 dB(A) is observed over a flat plate of the same overall dimensions for the corrugated plates. The vibro-acoustic simulation results based on SEA for the prediction of sound transmission loss and radiation efficiency are also confirming same behaviour of corrugated plates^[12].

3. CONCLUSION

By introducing discontinuities in the form of corrugations, the possibility of changing the flat nature of plates and their interaction with the surrounding air is attempted. Several designs of corrugations of various geometric configurations on plates were fabricated to conduct experiments to measure sound insertion loss. It is found that both low and high frequency behaviours of the corrugated plates are affected by suitable choice of the stiffener configuration and the spacing between the stiffeners as well. In the frequency range just below the coincidence, a little deterioration in sound insertion loss is observed due to additional edges incorporated because of using stiffeners. At low frequencies, due to relatively more sound radiation factor of set A than set B corrugated plates, the insertion loss of set B plates shows a little improvement. Sound radiation efficiency plays a significant role at coincidence. At the critical frequency, the plate vibration amplitude increases and the radiation efficiency also increases. Thus, at the critical frequency, the sound transmission is high due to modes resonant around a band centred at the coincidence frequencies. This behaviour is dominant for set A plates than set B plates due to extra edges in set A plates.

The size of the plates for the experiments was kept small within manageable limits for ease in conducting experiments. From practical application point of view, increase in size of the plates will further increase sound insertion loss to still higher values than observed in the present investigation.

To summarize the results of measured sound insertion loss, it can be said that stiffening the plate by placing stiffeners at proper position and selecting their proper geometry can significantly improve sound insulation performance of corrugated plates. Further, addition of stiffener at improper locations may lead to little deterioration in sound insulation performance. Hence, it is suggested that care must be taken for the selection of geometrical parameters of stiffeners and their relative placement while using the corrugated plate structures for reducing sound radiation from corrugated plates and sound transmission through them.

4. REFERENCES

- [1] M.J. Crocker and A.J. Price, 1969. Sound transmission using Statistical Energy Analysis, *Journal of Sound and Vibration*, **9**(3), 469-486.
- [2] K. Renji, 2001. On the effect of boundaries on radiation resistance of plates, *Journal of the Acoustical Society of America*, **110**(3), 1252-1255.
- [3] C.Y. Cheng and R.J. Shyu, 2006. Sound transmission of double and triple leafs using statistical energy analysis, *Journal of Taiwan society of naval architects and marine engineers*, **25**(1), 1-6.
- [4] K. Renji, P.S. Nair and S. Narayanan, 2002. Response of a plate to diffuse acoustic field using statistical energy analysis, *Journal of Sound and Vibration*, **254**(3), 523-539.
- [5] C.Y. Cheng, R.J. Shyu and D.Y. Liou, 2007. Statistical energy analysis of non-resonant response of isotropic and orthotropic plates, *Journal of Mechanical Science Technology*, **21**, 2082-2090.
- [6] T. Onsay, A. Akanda and G. Gregory, 1998. Vibroacoustic behaviour of bead stiffened flat panels: FEA, SEA and experimental analysis, *Society of Automotive Engineers*.
- [7] C.P. Cordonnier, S. Pautin and D. Biron, 1992. Contribution to the study of sound transmission and radiation of corrugated steel structures, *Journal of Sound and Vibration*, **157**(3), 515-530.
- [8] C.F. Ng and H. Zheng, 1998. Sound Transmission through Double-leaf Corrugated Panel constructions, *Applied Acoustics*, **53**(1-3), 15-34.
- [9] R. Zhou and M.J. Crocker, 2010. Sound transmission loss of foam-filled honeycomb sandwich panels using statistical energy analysis and theoretical and measured dynamic properties, *Journal of Sound and Vibration*, **329**, 673-686.
- [10] H. Aygun and K. Attenborough, 2008. The insertion loss of perforated porous plates in a duct without and with mean air flow, *Applied Acoustics*, **69**, 506-513.
- [11] J.E. Sylvia and A.J. Hull, 2013. A Dynamic Model of a Reinforced Thin Plate with Ribs of Finite Width, *International Journal of Acoustics and Vibration*, **18**(2), 86-90.
- [12] S.S. Pathan, 2019, Structural Dynamic Modification to Reduce Sound Radiation Factor, Ph.D. Thesis, I.I.T., Bombay.
- [13] R. Piscoya and M. Ochmann, 2011, Transmission loss of corrugated plates, *Forum Acusticum- European Acoustics Association*, pp. 211-215.

Acoustical properties of jute felt sintered with cotton shoddy

Manish Raj, Shahab Fatima and Naresh Tandon*

*Centre for Automotive Research & Tribology (Formerly ITMMEC),
Indian Institute of Technology Delhi, Hauz Khas, New Delhi-110016
e-mail: ntandon@itmmech.iitd.ac.in*

[Received: 28-10-2019; Revised: 03-03-2020; Accepted: 17-03-2020]

ABSTRACT

During the preparation of various jute components like bags and fabrics, a lot of waste jute fibers are generated in jute mills in large quantities for which some alternate application needs to be explored. Cotton shoddy is obtained from recycled clothes, and thus its supply is ensured in the long run at industrial levels. As reported in several studies, pure jute is a good sound absorber which has been studied in different forms like fibers, non-woven felts and composites. This study focuses on highlighting the acoustical properties of these waste jute fibers sintered with cotton shoddy. The felts are characterized for their physical parameters and acoustical properties like diameter, density, porosity, tortuosity, airflow resistivity, characteristic lengths, etc. Theoretical results are obtained using Miki model which is later validated with experimental results obtained. Effective airflow resistivity is obtained using inverse acoustical characterization in such a way that there is a minimum difference between measured and estimated results. This effective airflow resistivity is useful to estimate sound absorption coefficients at thickness values other than the measured one.

1. INTRODUCTION

The huge market, intense competition of acoustic materials, and stricter norms has motivated researchers to come up with low-cost alternatives. In this direction, many natural materials have been tested where the obtained results have been quite encouraging^[1-2]. This motivated the authors to explore green materials which are considered to be industrial waste. As presented in their earlier work in which waste jute fibers was reported as an effective sound absorber, this work reports the result on felts of waste jute sintered with cotton shoddy in different percentages^[3]. Cotton shoddy is mainly obtained from used clothes, and therefore its supply is long ensured. It is used as a filler material in low-cost pillows and mattresses. A detailed discussion on processing of shoddy is reported in earlier work of the authors⁴. The work is divided into four subparts, in which after establishing the problem statement in first part, it proceeds toward a brief discussion on materials and methods in the second subpart. The third section is devoted to discussions on results obtained which leads to conclusions in the fourth subpart.

NOMENCLATURE

m	mass	SAC	sound absorption coefficient
t	thickness of the sample	Z_c	characteristics impedance
ϕ	porosity of the sample	j	$\sqrt{-1}$
ρ_{felt}	density of the sound absorber	C_o	speed of sound in air
ρ_{fiber}	density of the nettle fibers	f	frequency
α_{∞}	tortuosity of the sound absorber	k	complex wavenumber
s	constant	Z_s	surface impedance
η	viscosity of air	α	sound absorption coefficient
Λ	viscous characteristics length	S	Free-flow cross section area
Λ'	thermal characteristics length	ρ_{air}	density of air
σ	airflow resistivity	R	complex reflection coefficient
Z_o	impedance of air	Z_c	characteristics impedance
WJ	waste jute	CS	cotton shoddy
M_1	Material 1	M_2	Material 2

2. MATERIALS AND METHODS

The felts of waste jute fibers and cotton shoddy fibers are sintered to create two types of felts, in which one fiber is used as the base fiber, and the other one the carrier fiber alternatively. The first felt (M_1) is 70% waste jute fibers (WJ), and 30% cotton shoddy (CS) fibers, and the second one (M_2) consists 30% waste jute, and 70% cotton shoddy. Their basic characterization consists of effective diameter, and density measurement which is performed by optical microscope and by floatation method respectively. These techniques have been explained in detail in their earlier reported work in reference^[3]. As reported in reference^[3], the best thickness of sound absorbers was found to be 70 mm and therefore in this study the felt of both the materials M_1 and M_2 are stacked to obtain sound absorbing samples of 70 mm thickness. The air-gap between the layers is removed by exposing them to a pressure of 12.5 kPa in a mould. The magnitude of pressure is estimated by hit and trial method, and the removal of air-gap between the individual felt layers is confirmed by sound absorption response achieved on samples prepared with different pressures. The removal of air-gap was ensured when the response of sound absorption spectrum is similar to that of a high pass filter, and not a band pass filter. The diameter of these samples were 100 mm, and their densities are 78 kg/m³ and 82 kg/m³ respectively. The prepared samples are shown in Fig. 1.



Fig. 1. Prepared samples with mould and dead weights used to apply pressure

Porosity, tortuosity and characteristics lengths are estimated empirically using Eq. (1) - (4). Airflow resistivity and sound absorption spectrum is measured experimentally on an indigenously developed experimental set up as per ISO 9053 and ASTM E-1050 respectively. The importance of these parameters is quite well known but for completeness, has been explained in detail in reference^[3].

$$\phi = 1 - \frac{\rho_{\text{felt}}}{\rho_{\text{fiber}}} \quad (1)$$

$$\alpha_{\infty} = 1 + \frac{1 - \phi}{2\phi} \quad (2)$$

$$\Lambda = \frac{1}{s} \sqrt{\frac{8\eta\alpha_{\infty}}{\phi\sigma}} \quad (3)$$

$$\Lambda' = 2\Lambda \quad (4)$$

Theoretical sound absorption spectrum can be suitably estimated by using empirical models which uses the characteristics of a sound absorber as an input. As only airflow resistivity has been experimentally measured in this work, the adopted model for theoretical absorption spectrum estimation is Miki model^[5]. This model has been time-tested for accurate result prediction, and happens to be the corrected version of the primitive Delany-Bazley model^[6]. The equations of Miki model are shown in Eq. (5) - (9)^[7]. The originally developed equations of Delany-Bazley and Miki were in terms of a dimensionless parameter $\left(\frac{\rho_{\text{air}}f}{\sigma}\right)$. However, for mathematical simplicity, and as observed from the literature^[7, 10], the density of air (ρ_{air}), is taken out and the equations (5) and (6) are considered in terms of $\left(\frac{f}{\sigma}\right)$.

$$z_c = \rho_0 c_0 \left[1 + .070 \left(\frac{f}{\sigma}\right)^{-.632} - .107j \left(\frac{f}{\sigma}\right)^{-.632} \right] \quad (5)$$

$$k = \frac{2\pi f}{c_0} \left[1 + .109 \left(\frac{f}{\sigma}\right)^{-.618} - .160j \left(\frac{f}{\sigma}\right)^{-.618} \right] \quad (6)$$

$$z_s = -jz_c \cot(kt) \quad (7)$$

$$R = \frac{z_s - \rho_0 c_0}{z_s + \rho_0 c_0} \quad (8)$$

$$\alpha = 1 - |R|^2 \quad (9)$$

As the sound absorption spectrum is measured only at 70 mm thick samples, the results at other thicknesses can be estimated by theoretical model, which happens to be Miki model in the present case. With an intention to accurately estimate the theoretical results, effective airflow resistivity is estimated by solving an optimization problem which minimizes the root mean squared difference between the experimentally measured and theoretically estimated sound absorption coefficients. The optimization problem is solved by genetic algorithm solver in MATLAB 2017a in parallel processing mode, and the estimated effective airflow resistivity is estimated.

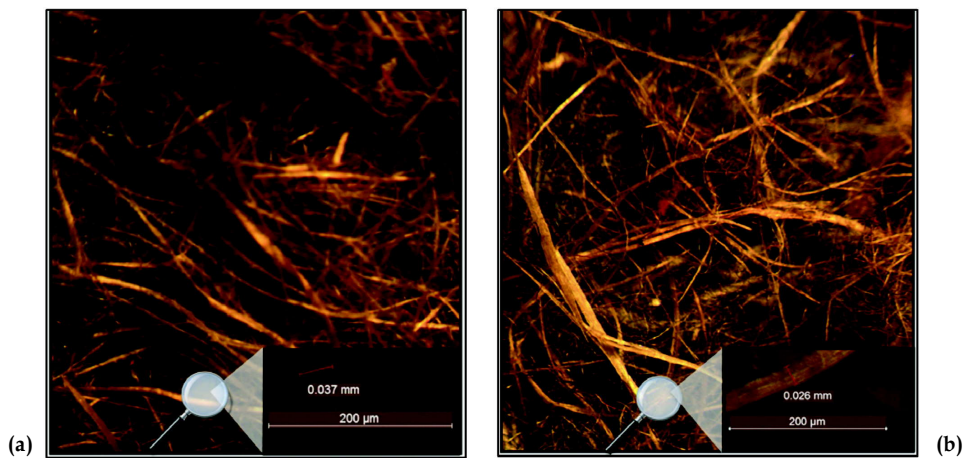
3. RESULTS AND DISCUSSIONS

The results of physical and acoustical characterization are summarized in Table 1. The density of the fiber assembly is between 1300-1500 kg/m³, which happens to be the densities of jute and cotton

Table 1. Physical and acoustical characteristics of the sound absorbers.

Characteristics	Material 1 (M_1) (70% WJ, 30% CS)	Material 2 (M_2) (30% WJ, 70% CS)
Sample Thickness (mm)	70	70
Fiber density (kg/m^3)	1458	1461
Average fiber diameter (μm)	39	31
Sample density (kg/m^3)	78	82
Porosity (ϕ)	0.9465	0.9438
Tortuosity α_∞	1.0282	1.0297
VCL (Λ) (μm)	92.06	87.75
TCL (Λ') (μm)	184.12	175.51
Measured airflow resistivity (N-s/m^4)	15200	16800
Effective airflow resistivity (N-s/m^4)	18240	19782
Average sound absorption	0.72	0.74

respectively. However, due to carding and other manufacturing processes during production of waste jute fibers, the matrix of lignin and wax etc. which hold individual fiber strands together gets removed and therefore their density increases. For this reason, the density of both the sintered fiber composition is inclined towards 1500 kg/m^3 , which happens to be the density of pure cotton. The average fiber diameter is estimated by statistical averaging of individual fiber diameters measured with microscopic images shown in Fig. 2. As observed from Table-1, increase in percentage of cotton shoddy has resulted in thinner average diameter, which is a favorable characteristics of a good sound absorber. For a fair comparison between both the materials, the porosity of both the materials as estimated from Eq. (1) is maintained approximately same by a slight variation in the sample density. The samples are having a porosity of 95%, which is very typical for sound absorbers of felt type sound absorbers, and thus these materials are expected to be a good sound absorber^[8-9]. Tortuosity which measures the curliness of pores is around 3%, is also approximately same for both the materials, which has been obtained from Eq. (2) directly linked with porosity. However, there is a significant difference between the characteristics lengths as observed from Table 1. An Increase in percentage of cotton shoddy has effectively reduced the characteristics length, and increased airflow resistivity, and the effect of which can be clearly observed from Fig. 3 which compares the measured sound absorption coefficient of both these materials. The increase in percentage of cotton shoddy has resulted in thinner average fiber, having a smaller pore size which has resulted in a slight increase of sound absorption coefficient.

**Fig. 2.** Microscopic images of materials (a) Material 1 (M_1) (b) Material 2 (M_2)

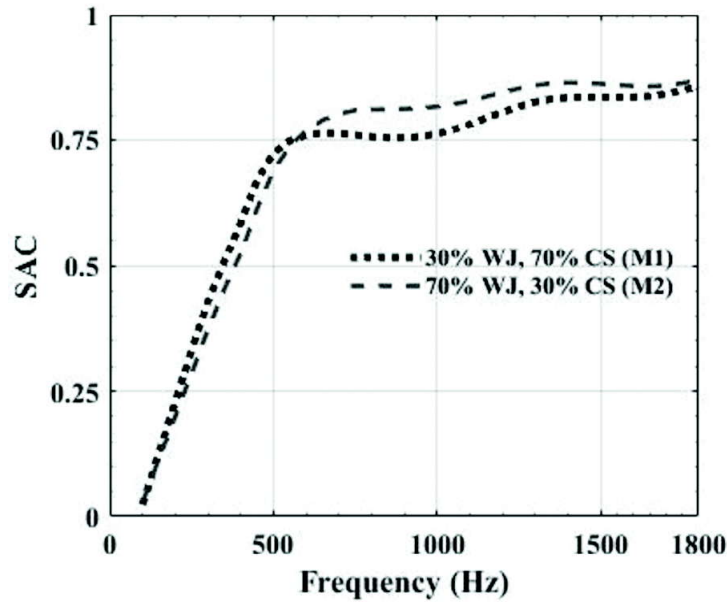


Fig. 3. Measured sound absorption coefficients of both materials

The convergence of optimization problem which minimizes the root mean squared difference between measured and predicted sound absorption coefficients are shown in Fig. 4. The response is amplified by 100 to achieve convergence up to an increased decimal places, and the results are obtained from MATLAB GA solver after 100 generations. The optimization has converged quite well as can be observed from Fig. 4a and 4b, for material 1 and material 2 respectively. The effective airflow resistivity as obtained from optimization problem is higher than the measured one as reported in Table 1. The experimentally measured sound absorption coefficient, and the theoretically measured ones using Miki model (Eq. (5) - (9)) by measured and effective airflow resistivity are compared in Fig. 5. As observed from Fig. 5a and 5b, though the theoretical result obtained after using effective airflow resistivity is slightly closer to the experimentally measured one, but still the difference is significant. This difference, even after nicely converged results of optimization, means the other acoustical characteristics are having a significant impact on the sound absorption spectrum and needs to be accounted for. However, as the average fiber diameter is quite thick in nature, this much difference always appears as can be observed in literature^[3, 10].

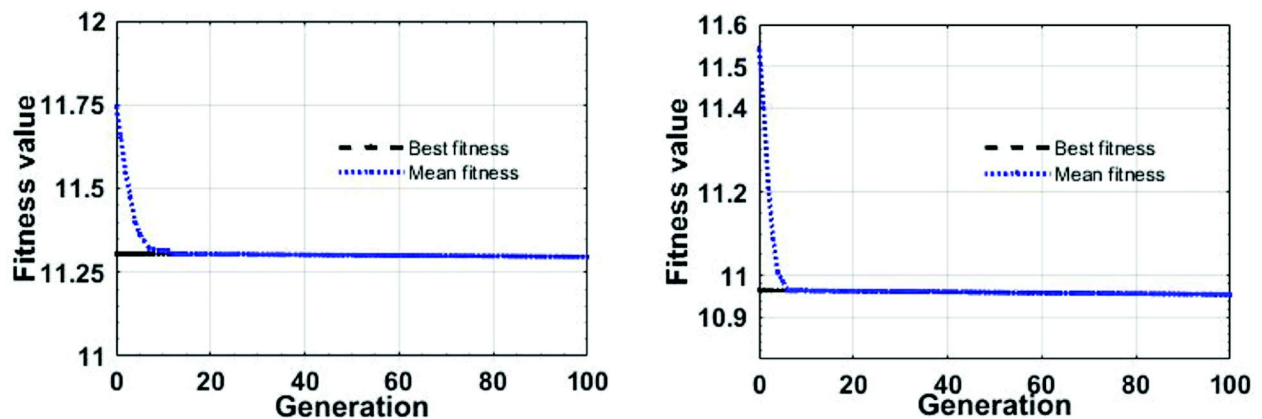
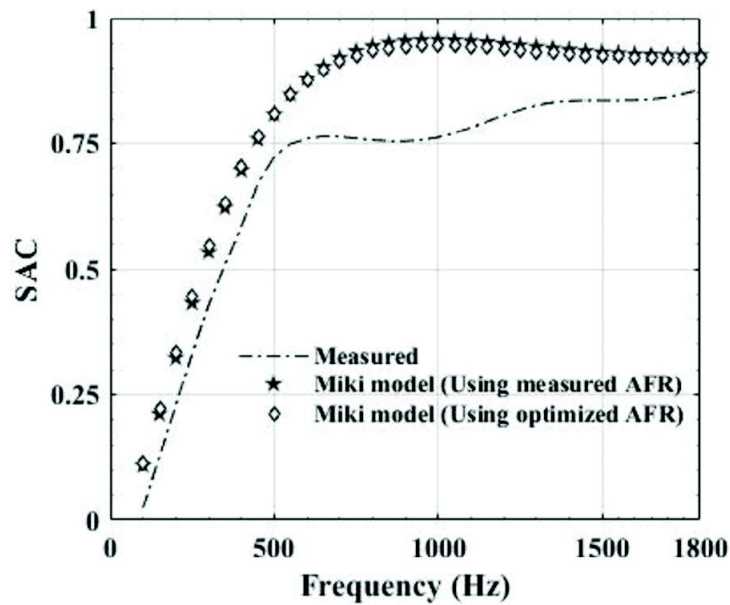
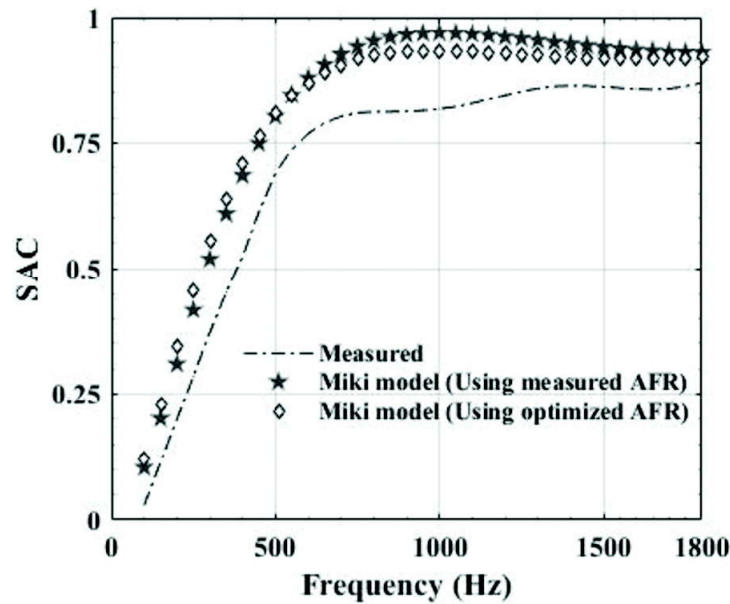


Fig. 4. Convergence of the optimization objective problem to estimate effective airflow resistivity by Miki model (a) Material 1 (M_1) (b) Material 2 (M_2)



(a)



(b)

Fig. 5. Comparison of experimentally measured and theoretically estimated sound absorption coefficients (a) Material 1 (M_1) (b) Material 2 (M_2)

4. CONCLUSION

The work aimed to explore the applications of abundantly available, low cost recycled material as a potential sound absorber. The measurements have shown both the materials in different composition of waste jute fibers and cotton shoddy as good sound absorbers with average sound absorption coefficient being greater than 0.7. In fact, the sound absorption coefficients greater than 0.75 beyond 500 Hz is achieved

for 70 mm thick samples. The effective airflow resistivity is obtained from optimization. Though there is a significant difference between the numerical values of effective airflow resistivity and measured airflow resistivity, its effect on sound absorption spectrum is not very significant at the tested thickness of the sound absorber. However, it will be useful to estimate the sound absorption spectrum at thicknesses where airflow resistivity plays a dominant role.

5. ACKNOWLEDGEMENT

The authors are thankful to the Department of Science and Technology (Government of India) for funding the project.

6. REFERENCES

- [1] D.J. Oldham, C.A. Egan and R.D. Cookson, 2011. Sustainable acoustic absorbers from the biomass, *Applied Acoustics*, **72**, 350-363.
- [2] F. Asdrubali, S. Schiavoni and K. Horoshenkov, 2012. A review of sustainable materials for acoustic applications, *Building Acoustics*, **19**, 283-312.
- [3] M. Raj, S. Fatima and N. Tandon, 2020. Recycled materials as a potential replacement to synthetic sound absorbers: A study on denim shoddy and waste jute fibers, *Applied Acoustics*, **159**, 1-13.
- [4] M. Raj, S. Fatima and N. Tandon, 2019. Acoustical Properties of Denim Shoddy based Recycled Material. In *INTER-NOISE and NOISE-CON Congress and Conference Proceedings*, **259**, 3528-3533.
- [5] Y. Miki, 1990. Acoustical properties of porous materials-Modifications of Delany-Bazley models, *Journal of the Acoustical Society of Japan*, **11**, 19-24.
- [6] M.E. Delany and E.N. Bazley, 1969. Acoustical properties of fibrous absorbent materials, *Applied Acoustics*, **3**, 105-116.
- [7] S. Rwawiire, B. Tomkova, J. Militky, L. Hes and B.M. Kale, 2017. Acoustic and thermal properties of a cellulose nonwoven natural fabric (barkcloth), *Applied Acoustics*, **116**, 177-183.
- [8] S. Fatima, and A.R. Mohanty, 2011. Acoustical and fire-retardant properties of jute composite material, *Applied Acoustics*, **72**, 108-114.
- [9] P.V. Bansod and A.R. Mohanty, 2016. Inverse acoustical characterization of natural jute sound absorbing material by the particle swarm optimization method, *Applied Acoustics*, **112**, 41-52.
- [10] C. Othmani, M. Taktak, A. Zein, T. Hentati, T. Elnady, T. Fakhfakh and M. Haddar, 2016. Experimental and theoretical investigation of the acoustic performance of sugarcane wastes based material, *Applied Acoustics*, **109**, 90-96.

Impulsive type acoustic source localization using time delay measurements

A. R. Mohanty* and Chinmayi Mahapatra

*Department of Mechanical Engineering,
Indian Institute of Technology Kharagpur, Kharagpur-721302 (WB)
e-mail: amohanty@mech.iitkgp.ac.in*

[Received: 20-12-2019; Revised: 03-03-2020; Accepted: 17-03-2020]

ABSTRACT

This paper presents various positioning algorithms based on Time Difference of Arrival (TDOA) for impulsive type acoustic source localization in both reverberant indoor and free-field outdoor environments. Time delay is estimated by cross-correlating the received signals from an array of microphones. The Cross-Correlation (CC) is calculated directly in the time domain for high sampling frequency, but for low sampling frequency, prefilters are applied before cross-correlation estimation in the frequency domain. A set of nonlinear hyperbolic equations are solved either iteratively by using an optimization function or by transforming them into a linear form. By solving the linear set of equations, a unique solution (source positions and source range) is obtained for both 2D and 3D space. To check the effectiveness and accuracy of each positioning algorithms, two experiments are conducted in different environments. The first experiment was conducted in a reverberant environment by generating a single bursting sound through an omnidirectional loudspeaker system. Secondly, a low explosive bomb was exploded in a free field outdoor environment. To validate the experimental results, true source positions, and time delay measurements are compared in both the environments.

1. INTRODUCTION

In the last two decades, source localization through time delay estimation method by using microphones are used in many applications like speech source recognition, battlefield acoustics, sniper localization, radar communication, underwater acoustics, teleconferencing, etc. Topically, the passive ranging technique involves the localization, detection, and targeting of an acoustic impulsive sound source using microphones that are spatially distributed in a stationary platform. The sound source can be localized by using many techniques such as Time of Arrival (TOA)^[1], TDOA^[2], Direction of Arrival (DOA)^[3] just to name a few. But for transient events like sniper localization, artillery fires, and mortar fires, muzzle blast, etc., the signal is usually detected and monitored by using TDOA and TOA.

The maximum likelihood technique is used to estimate the TDOA between signals in the presence of uncorrelated noise for a single stationary sound source in^[1,3]. Estimation of time delay by Cross-Correlation (CC) is sensitive to ambient noise for the whole class of stationary signals. So a mean square error expression for CC and optimum weight function associated with Generalized Cross-Correlation (GCC) function was used to investigate the problem of time delay estimation for stationary signal^[2]. GCC based

weighting estimators were used to compute the time delays in the field of passive sonar signal processing due to its simplicity and ease of implementation^[4]. For positioning of single and multiple sources, GCC function with PHAT estimator is popularly used to estimate the time delay of arrival and provide the relationship between the correlation method and source characteristics^[5]. In a noisy and reverberation environment, many reflections reach the sensors after the direct wavefront. Therefore, a comparative study has been carried out using Time Delay Estimation (TDE) algorithm in different adverse environmental conditions^[6]. To know the performance of time delay estimation, a theoretical analysis has been carried out to estimate the time delay for a multipath propagation in a room^[7, 8]. GCC based function can also be used in many applications like underwater sound source localization^[9], locate the point of burst of an artillery shell^[10], sniper localization, etc. Weighted GCC methods and Minimum Variance Distortion Less Response (MVDR) weights have been used for the accurate tracking of the signal^[11]. After estimation of time delay by using these approaches, acoustic source localization and tracking based on the 3-D approach has become the area of interest in the field of acoustics. The DOA, and steered power response algorithms have been used in order to improve the tracking of multiple sources^[12, 13].

There are many approaches available to localize an acoustic source, but among them, the TDOA method utilizing microphone array is a common approach for localization of a single impulsive source. As there are a large number of echoes present in a reverberant environment, it is difficult to achieve satisfactory precision in time delay estimation. Moreover, in a free-field environment, error arises in the time delay estimation, mainly due to meteorological conditions, terrain type, ground reflections, atmospheric absorption of sound, etc. The fundamental problem arises when the source is near the ground; the microphone array that is usually one or two-meter from the ground and source range is relatively large as compared to the altitude of the microphone above the ground, which significantly degrades the localization accuracy^[14]. After understanding these environmental parameters, the next step is to solve the nonlinear equations that are based on a hyperbolic concept to estimate the source coordinate. For a known relation between the microphone and source coordinates, closed-form position estimates are well suited for real-time implementations. However, the closed-form Spherical Interpolation (SI) estimator solves the linear equations directly via Least Squares (LS) by maintaining the relationship among time delay, isospeed sound propagation in air, and microphone coordinates^[15]. In this paper, the localization algorithm for the spherical wavefronts is described to localize an impulsive sound source.

Experiments are carried out in different environments, and then the measured data are utilized in positioning algorithms to ensure their effectiveness and accuracy in locating a single impulsive sound source. In this paper, the relevance of using the TDOA technique for the positioning of a single point source in the free and reverberant environment is evaluated. Two positioning algorithms are presented here. One is used for 2D positioning of a sound source in a reverberant indoor environment, and another one is for 3D positioning of a point source in a far-field outdoor environment. Nonlinear hyperbolic range equations are solved by using an optimization function to obtain 2D source coordinates. But, in LS estimation method, the 3D source localization is performed after linearizing the nonlinear equations. A comparative study is also performed among the time delay estimation techniques in order to improve the precision of source estimates.

The paper is organized as follows. Section 2 discusses estimation of time delay using cross correlation function and generalized cross correlation function. Section 3 presents position algorithms available to estimate the source range and source coordinates. Section 4 presents experimental setup details as well as experimental validations for both the experiment. Section 5 provides some concluding remarks.

2. TIME DIFFERENCE OF ARRIVAL ESTIMATION

Time Difference of Arrival (TDOA) is defined as the difference between two TOA measurements of the received signals. For estimating the TDOA, mathematical formulation for the received signal is the most important aspect. Considering that there is 'n' number of microphones present around a single omnidirectional sound source, as shown in Fig. 1. The general mathematical model of the received signal for i^{th} microphone can be represented as:

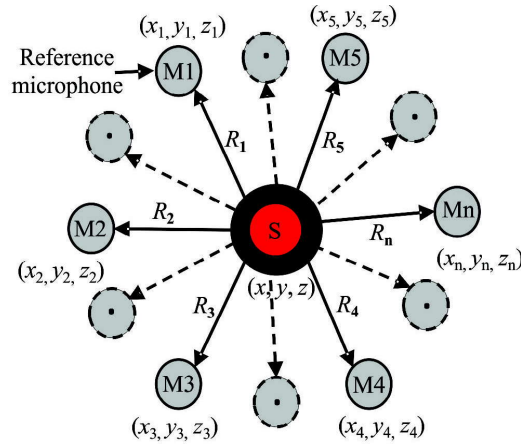


Fig. 1. Schematic diagram depicts a single acoustic source and 'n' number of microphones

$$M_i [t] = \alpha_i s(t - \delta_{i1}) + n_i [t] \quad (1)$$

where $M_i [t]$ is the received signal, $s(t)$ is the signal-of-interest assumed to be uncorrelated with noise $n_i [t]$ and α_i being the attenuation of the signals. δ_{i1} is the time delay between the received signals by taking microphone 1 as reference. For the case of microphone 1, the time delay is measured with respect to the same microphone, so δ_{11} is considered as zero.

For example, the mathematical received signal model for microphone 1 and 2 is given by

$$\begin{aligned} M_1 (t) &= \alpha_1 s(t) + n_1 (t) \\ M_2 (t) &= \alpha_2 s(t - \delta_{21}) + n_2 (t) \end{aligned} \quad (2)$$

Cross-correlation is a common approach, which correlates two independent random received signals among them one microphone is taken as a reference and time shift of τ is associated with another microphone in order to produce the desired result of time delay, which can be expressed as:

$$P_{M_1 M_2} (\tau) = E[M_1 (t) M_2 (t + \tau)] \text{ where } E \text{ denotes expectation.} \quad (3)$$

The time lag corresponding to the maximum peak provides the estimated time delay between the received signals that occur at $\delta = \tau$.

An alternative way to estimate CC function $P_{M_1 M_2} (\tau)$ from the cross-spectral density function $R_{M_1 M_2} (f)$ in the frequency domain by applying fast Fourier transform (FFT) is given as:

$$P_{M_1 M_2} (\tau) = \int_{-\infty}^{\infty} R_{M_1 M_2} (f) e^{j2\pi f\tau} df \quad (4)$$

$$\text{where, } R_{M_1 M_2} (f) = M_1^* (f) M_2 (f)$$

$M_1^* (f)$ is the complex conjugate of the Fourier transform of the signal $M_1 (t)$. The asterisk symbol (*) denotes a complex conjugate operation.

In a reverberation environment, due to high reflection from the wall, the peak appears in the time plot shifted slightly. Therefore, in the GCC method, different types of weighting estimators are generally applied whose function is to clean the signal and make it into a more useful form before passing into the correlator^[1]. The general expression for GCC function after applying prefilters is expressed as:

$$P_{M_1 M_2}^{(g)} (\tau) = \int_{-\infty}^{\infty} \phi(f) R_{M_1 M_2} (f) e^{j2\pi f\tau} df \quad (5)$$

The weighting function for Phase Transform (PHAT) is [1],

$$\phi_{PHAT}(f) = \frac{1}{|R_{M_1 M_2}(f)|} \quad (6)$$

Similarly, the weighting estimator for the Smoothed Coherence Transform (SCOT) is,

$$\phi_{SCOT}(f) = \frac{1}{\sqrt{R_{M_1 M_1}(f)R_{M_2 M_2}(f)}} \quad (7)$$

Here, $\phi_{PHAT}(f)$ and $\phi_{SCOT}(f)$ are the PHAT and SCOT weighting estimators. Finally, the delay δ_{21} can be expressed as:

$$\delta_{21} = \text{argmax} \left[P_{M_1 M_2}^{(g)}(\tau) \right] / F_s \quad (8)$$

where F_s is the sampling frequency.

3. ACOUSTIC SOURCE LOCALIZATION

Acoustic source localization is accomplished in two steps. In the first step, TDOA between the microphones is obtained through the use of various time delay estimation techniques. Then, the next step is to implement these time-delay measurements in various positioning algorithms to produce the desired result of the source position from the set of nonlinear equations. These nonlinear equations can be solved either iteratively or non-iteratively. An optimization function is utilized iteratively to obtain an unambiguous solution of source estimates from the set of nonlinear equations. In the standard LS method, source estimates are measured after being linearized the nonlinear equations.

3.1 Nonlinear Hyperbolic Positioning Algorithm (for 2D Space)

Acoustic source localization requires an efficient positioning algorithm to obtain an accurate result with a less percentage error. Therefore, hyperbolic concept based source localization is used where the intersection of hyperbola gives the desired source location, as shown in Fig. 2. A hyperbola consists of a set of all points in a plane, such that absolute difference of their distances from two-fixed point i.e., the position of the microphones, is always constant, which gives the path difference between the microphones. When a signal is radiated from the source (S), it reaches to each microphone in the form of a spherical wavefront. However, for 2D source localization, the sphere is replaced by a circle. From that, a set of nonlinear equations is formed. This is implemented in an efficient optimization algorithm to produce an unambiguous solution of source position. The estimated path difference between the rest of the microphones and reference microphone 1 (d_{i1}) can be obtained from the estimated time delay from the expression :

$$d_{i1} = c \times \delta_{i1} \text{ where } i = 2, 3, \dots, n \quad (9)$$

where c is sound speed in air.

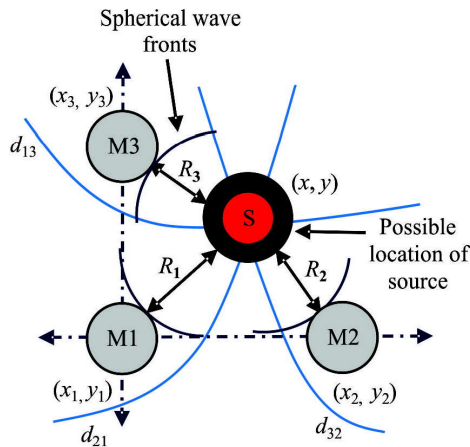


Fig. 2. Hyperbolic positioning of three microphones

From the known coordinates of the microphones (x_i, y_i) , the path difference measurements from i^{th} microphone to microphone 1 predicted by a assumed source location (x, y) can be written as :

$$D_{i1} = R_i(x, y) - R_1(x, y) = \text{constant} = \sqrt{(x_i - x)^2 + (y_i - y)^2} - \sqrt{(x_1 - x)^2 + (y_1 - y)^2} \quad (10)$$

The source position is on the hyperbola if it follows the above Eq. (10), which is based on hyperbolic concept.

In Eq. (10), there are two terms in the right hand side (RHS). First-term represents the value of range difference between the source and the i^{th} microphone *i.e.*, (R_i) and the second term represents the value of range difference between the source and thereference microphone *i.e.* (R_1) . For $i = 1$, as we are finding the path difference between the same microphone, $D_{11} = 0$. By equating Eq. (9) and Eq. (10), *i.e.*, $D_{i1} \approx d_{i1}$, the unknown source position can be measured using an iterative optimization algorithm.

$$d_{i1} = \sqrt{(x_i - x)^2 + (y_i - y)^2} - \sqrt{(x_1 - x)^2 + (y_1 - y)^2} \quad (11)$$

where d_{i1} is the measured path difference, and D_{i1} is path difference predicted from the source location estimates.

For the case of three microphones, it is observed that the set of nonlinear hyperbolic equations equals the number of unknown coordinates of the source, which is found to be consistent, and a unique solution. However, it cannot be solved easily because the solutions of nonlinear hyperbolic range difference (HRD) equations of the higher-order can be found only after squaring both sides of Eq. (11). Similarly, for the case of four microphones, the number of HRD equations are more than the number of unknown coordinates of the source in 2D space, which indicates the system is purely inconsistent. So, an iterative MATLAB function 'fsolve' is used to solve a system of nonlinear equations. The algorithms repeatedly work for improving an initial guess at each step of the solution. Moreover, it is possible that an initial guess, which is far away from the vicinity of an optimal solution, can cause the algorithm to fail.

3.2 Least Square Estimation (LSE) (for 3D Space)

In the LS method, a set of nonlinear hyperbolic equations are transformed into linear equations. A unique LS solution is obtained after linearization, which not only provides the source coordinates but also provides source range in one step.

Let 3D microphone coordinates are (x_i, y_i, z_i) , where $i = 1, 2 \dots n$. Let 3D source position is denoted as (x, y, z) . Eq. (9) can be rewritten as:

$$d_{i1} = c \times \delta_{i1} = R_i - R_1 \quad (12)$$

From the Pythagorean theorem, R_i can be written as :

$$R_i^2 = r_i - r_s^2 = (x_i - x)^2 + (y_i - y)^2 + (z_i - z)^2, \quad i \in [1, \dots n] \quad (13)$$

We have :

$$d_{i1} = R_i - R_1 \Rightarrow d_{i1} + R_1 = R_i \Rightarrow (d_{i1} + R_1)^2 = R_i^2 \quad (14)$$

After solving the above Eq. (14), we get

$$\Rightarrow (xx_i + yy_i + zz_i + d_{i1} R_1) = 0.5(K_i - d_{i1}^2) \text{ where } K_i = x_i^2 + y_i^2 + z_i^2 \quad (15)$$

This above Eq. (15) is a linear equation for unknown parameters x, y, z and R_1 . By using 'n' microphones measurements, the linear equation in matrix form can be written as^[15]

$$\mathbf{A}\theta = \mathbf{B} \quad (16)$$

where

$$\mathbf{A} = \begin{bmatrix} x_2 & y_2 & z_2 & d_{21} \\ x_3 & y_3 & z_3 & d_{31} \\ \cdot & \cdot & \cdot & \cdot \\ \cdot & \cdot & \cdot & \cdot \\ x_n & y_n & z_n & d_{n1} \end{bmatrix}, \quad \theta = \begin{bmatrix} x \\ y \\ z \\ D_1 \end{bmatrix}, \quad \mathbf{B} = 0.5 \begin{bmatrix} K_2 - d_{21}^2 \\ K_3 - d_{31}^2 \\ \cdot \\ \cdot \\ K_n - d_{n1}^2 \end{bmatrix} \quad (17)$$

The least square solution θ is

$$\theta = \mathbf{A}'\mathbf{B}' \quad (18)$$

where $\mathbf{A}' = (\mathbf{A}^T \mathbf{A})^{-1} \mathbf{A}^T$ is the pseudo-inverse of the matrix \mathbf{A} . The above Eq. (18) is not only providing the information regarding source coordinates but also helpful in estimation of the source range. In addition, the source range information redundancy can be exploited to improve this estimate. Otherwise, the corresponding ordinary LS problem is solved by adopting a linear minimization approach

$$\mathbf{J} = \min_{\theta} (\mathbf{A}\theta - \mathbf{B})^T (\mathbf{A}\theta - \mathbf{B}) \quad (19)$$

The ordinary LS criteria for source coordinates measurements are solved either by Eq. (18) or Eq. (19) to perturbing the observation vector \mathbf{A} and \mathbf{B} . The basic assumption considers here that the error only present on one side of the Eq. (16) *i.e.*, in the vector \mathbf{B} and the matrix \mathbf{A} contains exactly the known coordinates. However, the noise is always associated with the TDOA measurements; that is, d_{i1} is always disturbed by environmental noise. Hence, the measurements of d_{i1} are present in both the side of the Eq. (16) leads inaccuracy in source localization.

4. EXPERIMENTAL VALIDATION

The passive source localization operation was conducted in two different environments to check the relevance of using TDOA techniques as well as proposed positioning algorithms to locate an impulsive sound source. Real acoustic data were collected from a set of the microphone array. Initially, the experiment was carried out in a reverberant indoor environment by using a minimum of three microphones. If one microphone is considered as the reference among the microphone array, then in 2D, the source is found by the intersection of two lines; whereas in 3D, the source is localized by the intersection of three sets of hyperboloids; therefore at least four microphones are necessary to locate a source in 3D source positioning. In the next phase, for a low explosive case, localization was carried in a free-field outdoor environment. Eight microphones were arranged in a 3D box-shaped pattern to capture the signal emanated from the explosive acoustic source.

4.1 2D Source Positioning in Reverberant Indoor Environment

An experiment was conducted in a 10m × 5m × 6m reverberant room by using two or more spatially separated microphones of different configurations and a single omnidirectional sound source. In order to generate a pulse waveform, an arbitrary function generator (Tektronix AFG3000C) has been used. The

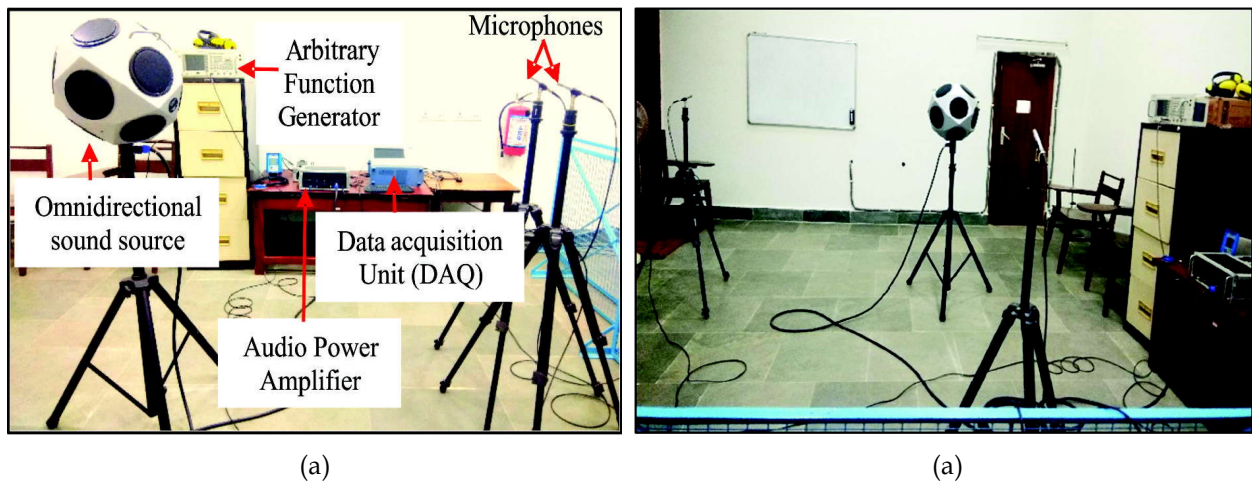


Fig. 3. Experimental setup of (a) two microphones arranged in the same place for zero time delay estimation (b) random orientation of two microphones

arbitrary function generator was regulated with different frequencies to generate bursting sound. In the current experiment, a 500 Hz frequency has been adjusted with an amplitude of 10V. The generated signal was supplied into an audio power amplifier (B&K 2734) through a BNC cable. Here, the audio power amplifier was used to drive a high power omnidirectional loudspeaker (B&K 4292) with an attenuation of -2dB and 0dB. Firstly, the experiment was conducted by taking attenuation of -2dB. Then in order to know the changes after decreasing the attenuation, another set of experiments was conducted at the attenuation of 0dB. Attenuator in power amplifier is used to reduce or attenuate the voltage level of a signal while introducing little or no distortion and insertion loss. After generating the sound signal in the omni directional sound source, the signals were acquired at different sampling frequencies of 10 kHz, 20 kHz, 50 kHz, and 100 kHz in a high speed 16 input channels data acquisition system (Yokogawa DL850). The acquired signals were later implemented for CC processing in the frequency domain using the fast Fourier transform (FFT).

In the first stage of the experiment, two microphones were placed near an omnidirectional sound source of the same distance to receive the sound signal, as shown in Fig. 3(a). The time delay between these two microphones was estimated by taking any one of the microphone as the reference microphone. As it is placed in the same distance from the source, the time delay obtained by using GCC method is zero at all sampling frequencies. Figure 3(b) shows the random arrangement of two microphones around the sound source. By keeping the source location constant, the position of microphones was changed under the sphere of 2m radius from the source. Similarly, the experiment was conducted by placing three microphones of a triangular and L-shaped configuration by applying the same test conditions.

In the next stage of the experiment, the coordinates of the microphones were taken by keeping one microphone as a reference for localizing a sound source. Thus, from the known values of co-ordinates of the microphones, the point of the bursting of an omnidirectional sound source was estimated by using the hyperbolic range difference equation.

4.1.1 Validation of indoor source positioning results

To calculate the source coordinates, it is necessary to estimate the TDOA among the received signals. So, in the initial phase of the experiment, two microphones were arranged randomly around the source in order to check the effectiveness of the proposed prefilers. Then, the experiment was proceeded by taking three microphones. Triangular and L-shaped pattern were chosen to arrange these three microphones, as shown in Fig. 4. In the triangular and L shaped pattern, M1 is preferred as a reference

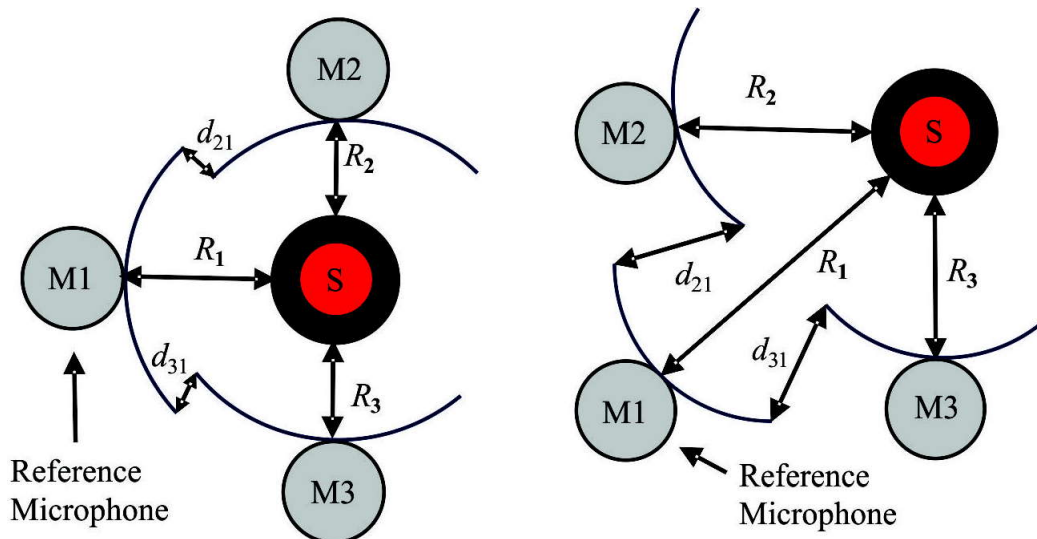


Fig. 4. Triangular and 'L' shaped configurations

microphone with coordinate (0, 0). The coordinates of M2 and M3 were (-0.06, 1.59) and (1.42, 0.73) m, whereas, in the L-shaped pattern, the respective coordinates were (-0.075, 1.72) and (1.42, -0.144) m. But instead of taking random orientations, triangular and L shaped pattern were followed to measure the TDOA. For two microphones, experimental data has been taken at a sampling rate of 100 KS/s for a total time length of 10s whereas for three microphones, experimental data has collected at a sampling rate of 50 KS/s for a total time length of 20s. After taking the experimental data, TDOA was estimated by using CC and GCC method. In MATLAB, xcorr function was used to estimate time delay for the cross-correlation method. Whereas, in GCC method, a weighting estimator or prefilter was multiplied before cross-correlation in order to attenuate the surrounding noise. Then, the theoretical results were calculated from the following expression.

$$\delta_{21} = \frac{R_2 - R_1}{c} \quad (20)$$

where δ_{21} is the time difference of arrival of the acoustic wave front at microphone 1 and microphone 2.

The result obtained from the experimental data has validated with the theoretical result, which is depicted in Table 1 for two microphones. Then after a comparison study, it was observed that GCC-PHAT provides satisfactory performance in the estimation of time delay. Hence, in Table 2, source localization operation was carried out using three microphones by utilizing GCC-PHAT time delay measurement data as well as microphone array geometry.

Table 1. Time delay estimation in CC and GCC method using two microphones

Microphones location from the source (d_{S1}, d_{S2}) (m)	Attenuation	TDOA	Theoretical time delay (ms)	Experimental Time Delay (ms)		
				CC	GCC-PHAT	GCC-SCOT
(1.09,1.28)	-2dB	δ_{12}	0.553	54.4	0.524	0.512
(2.30,2.70)	-2dB	δ_{12}	1.166	20.7	1.160	1.160

In Table 1, the experimental time delay measurements were validated with the theoretical result. After a comparison study, it was observed that the GCC-PHAT and SCOT weightings are giving a satisfactory result as compared to CC. In the attenuation of -2 dB and 0 dB, there is no such large difference present in the estimated time delays. All methods are giving nearer results at -2 and 0 dB attenuation. For lower sampling frequencies like 10 kHz and 20 kHz, the results don't match with theoretical results and give a large percentage of error in time delay. For the better localization of a stationary sound source, it is necessary to estimate the time delay accurately at a high sampling rate. Then the source was localized

Table 2. Source localization using three microphones

Pattern	Attenuation	TDOA	GCC-PHAT Time delay (ms)	Actual Source Location (x, y) (m)	Experimental Source Location (m)	% Error
Triangular	-2dB	δ_{12}	0.125	(0.570, 0.858)	(0.512, 0.841)	(10.10,1.90)
		δ_{13}	0.205			
	0dB	δ_{12}	0.125	(0.570, 0.858)	(0.547, 0.849)	
		δ_{13}	0.267			
L-shaped	-2dB	δ_{12}	1.991	(1.255,1.960)	(1.185,1.557)	(5.57,20.56)
		δ_{13}	0.702			
	0dB	δ_{12}	1.991	(1.255,1.960)	(1.185,1.557)	
		δ_{13}	0.702			

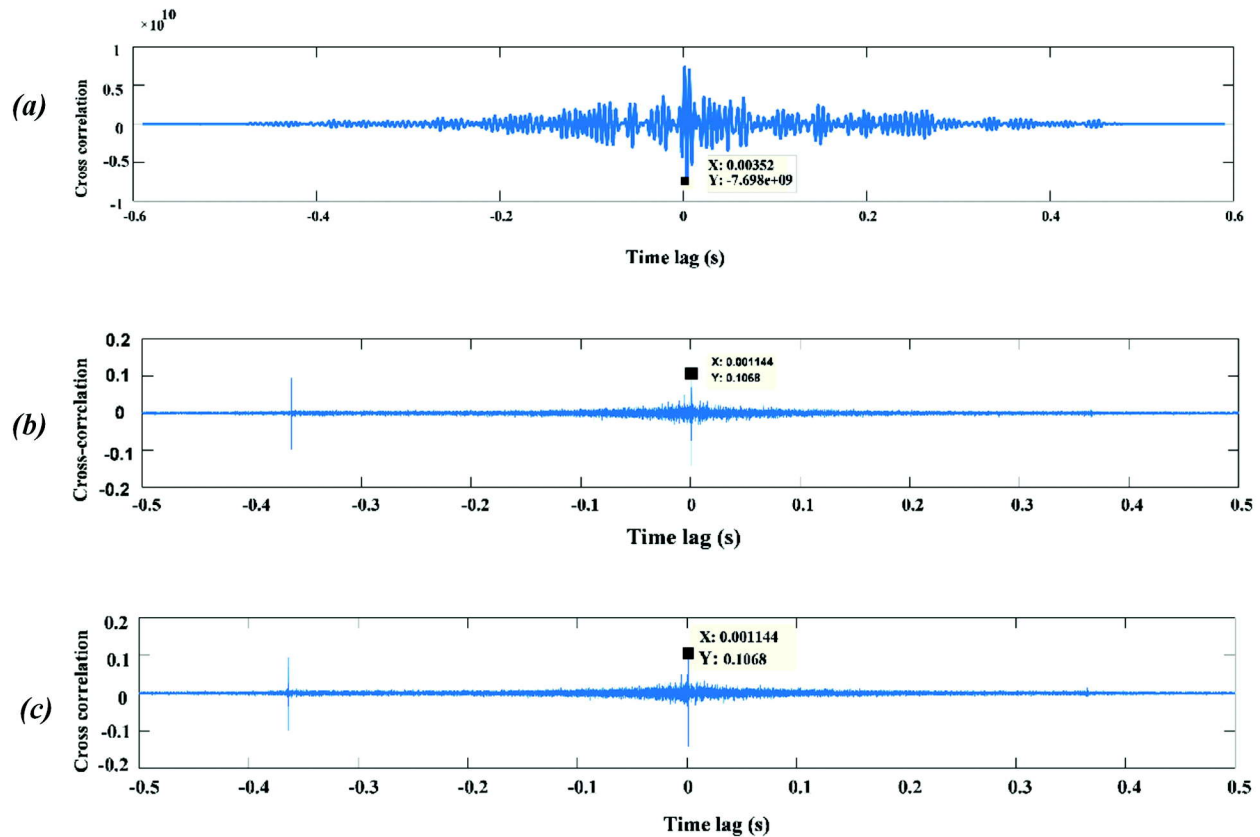


Fig. 5. Obtained signals in (a) CC (b) GCC-PHAT (c) GCC-SCOT in a reverberant environment

from the experimental time delay obtained from the GCC-PHAT method. From the known coordinates of the microphones, the source location was estimated in Table 2 by using the hyperbolic range difference equation.

Using MATLAB software, the time delay estimation of the signals is carried out for the microphones 1 and 2 and the microphones 1 and 3 by taking the CC, PHAT, and SCOT weighting estimators. The corresponding results obtained from MATLAB are represented in Fig. 5. The above curves are plotted between time lag and correlation sequence at the different lag position to obtain the maximum peak, which gives the estimated time delay between the signals. The GCC weighting estimators sharpen the peaks at the correct time delay compared to the CC results in an actual real-time signal at the low sampling frequency. Sidebands appear in the estimated signal due to the boundary reflection in the reverberation environment. Time lag corresponding to the maximum peak in the estimated signals gives the estimated time delay.

4.2 3D Source Positioning in Outdoor Free-Field Environment

Another set of experiment was carried out at Helipad, IIT Kharagpur using low explosive bomb. The x-, y- and z-coordinates of eight microphones (M1 to M8) are (0,0,1.4), (20,0,1.4), (20,23,1.4), (0,20,1.4), (0,0,2.16), (20,0,2.16), (20,23,2.16) and (0,20,2.16) m respectively which are arranged in a 3D box-shaped configuration shown in Fig. 6.

Each microphone data was sampled at a frequency of 1 MHz at 24-bit resolution by 12 channel data acquisition unit (DAQ) (DEWETRON). The set of equipment used for free field source localization is represented in Fig. 7. Traditional equipment such as thermometer and anemometer were utilized to

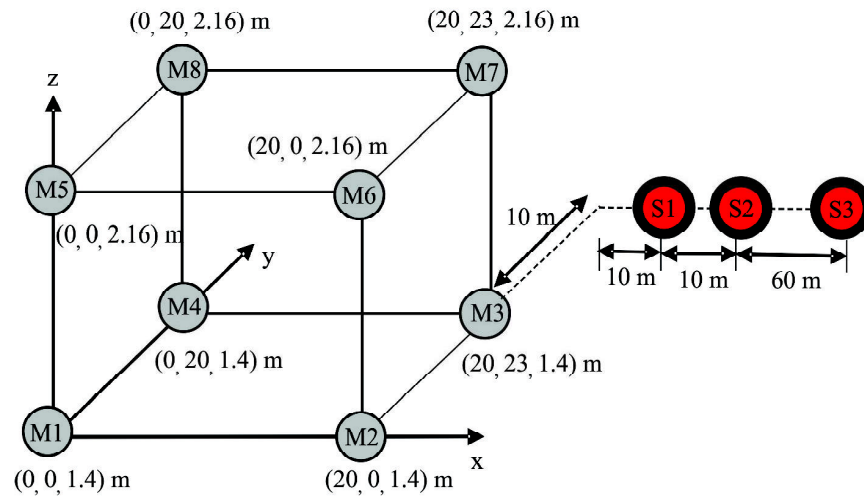


Fig. 6. 3D Arrangement of Microphones and source

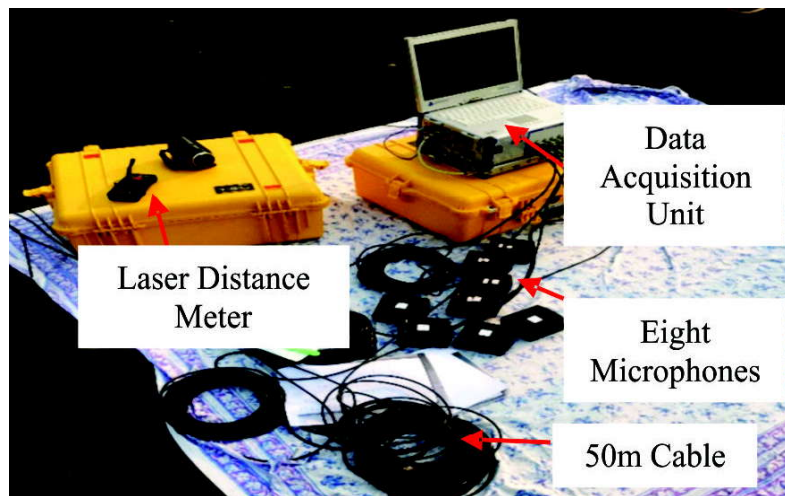


Fig. 7. View of the Measurements setup

measure the temperature and wind speed of 30°C and 0.7 m/s over the period of 4h in 55°NE direction to update the speed of the sound. GPS measuring unit was used to record the GPS coordinates. After getting the output in a data acquisition unit, the CC operation was performed in the time domain. Then, to examine the effect of the proposed methodology, the blasting experiment was carried out repeatedly over the ground at a distance of 10 m, 20 m and 80 m from the microphone 3 in the x-direction.

4.2.1 Validation of outdoor source positioning results

In this section, the path difference results and source localization results were discussed to show the performance of the proposed algorithm. Here, the CC algorithm is used to estimate corresponding TDOA measurements for seven microphone pairs. If there is no significant effect of temperature, wind speed, and wind direction present, then from Eq. (9), it is easy to get a path difference between the microphones by considering the speed of the sound as 343 m/s. But in the free field outdoor environment, there is fluctuation present in acoustical effects due to atmospheric turbulence. Hence, based on ambient temperature, wind direction, and wind speed, the velocity of the sound was measured. According to Kinsler, speed of sound (c), at a temperature of $T^{\circ}\text{C}$ is calculated from^[16]

$$c = 331.15 \times \sqrt{(1 + T / 273)} \tag{21}$$

After estimation of the speed of the sound at 30°C, the next step is to calculate the resultant speed of the sound in air as according to the wind speed and wind direction as follows

$$V_R = c + (V_w \cos\theta) \tag{22}$$

From Eq. (22), the resultant speed of the sound was obtained as 349.377 m/s. The experimental path difference between the microphones is given by

$$r_{i1} = V_R \times \delta_{i1} \tag{23}$$

The next step is to solve the source coordinates using data obtained from Eq. (23), and microphone coordinates applying least square estimation criteria.

Table 3. Comparison between the true and estimated value of path difference between the microphones

Path Difference	Actual path difference from GPS unit (m)			Estimated path difference from TDOA (m)		
	10m (S1)	20m (S2)	80m (S3)	10m (S1)	20m (S2)	80m (S3)
Mic1-Mic2	9.407	12.750	18.327	9.172	12.072	19.401
Mic1-Mic3	30.683	30.497	27.928	29.106	28.468	25.815
Mic1-Mic4	14.823	12.880	9.2860	11.068	9.537	8.749
Mic1-Mic5	0	0	0	-0.143	-0.123	-0.246
Mic1-Mic6	9.407	12.750	18.327	8.954	11.870	19.377
Mic1-Mic7	30.683	30.497	27.928	29.005	28.271	25.888
Mic1-Mic8	14.824	12.880	9.286	11.052	9.507	8.881

Table 4. Source coordinates results obtained from estimated path difference measurements

Experiment Details	Technique	Source co-ordinates from M1 (m)	Estimated source Coordinate (m)	True Source range (D ₁) (m)	Estimated source range (m)	% Error
1	Least square	(27, 33, 0)	(25.208, 27.979, -0.452)	42.472	38.583	9.156
2		(38, 33, 0)	(33.994, 29.717, -0.580)	50.175	45.724	8.870
3		(98, 33, 0)	(82.140, 39.549, -2.945)	106.668	94.228	11.660

In Table 3, the experimental result of path difference, which is obtained from TDOA measurements and resultant speed of the sound in air, was validated with the actual measurements. Then, the second table depicts the source coordinates results obtained by changing the blasting location from S1 to S3 from the stationary microphone configuration. From Table 4, it is observed that with an increase in the source range from the microphone configuration, the ability of the system reduced to capture the real signal. This occurs because of terrain type, surrounding background noise, and meteorological effects. As a result, error in time delay measurements reduces the performance of sound source localization. Moreover, it can also be noticed that the precision of source coordinates measurement gradually decreases in the z-direction with an increase in the source range. This is because the distance between source and microphone is relatively large as compared to the elevation of the microphone and source from the ground. Due to this basic problem, the microphones which are one or two meters near the ground is received the directed as well as the reflected sound emitted by a sound source.

Figure 8 displays the acoustic signatures of eight microphones captured by using the data acquisition unit during the period of an explosion. Figure 9 demonstrates that while the present method provides a

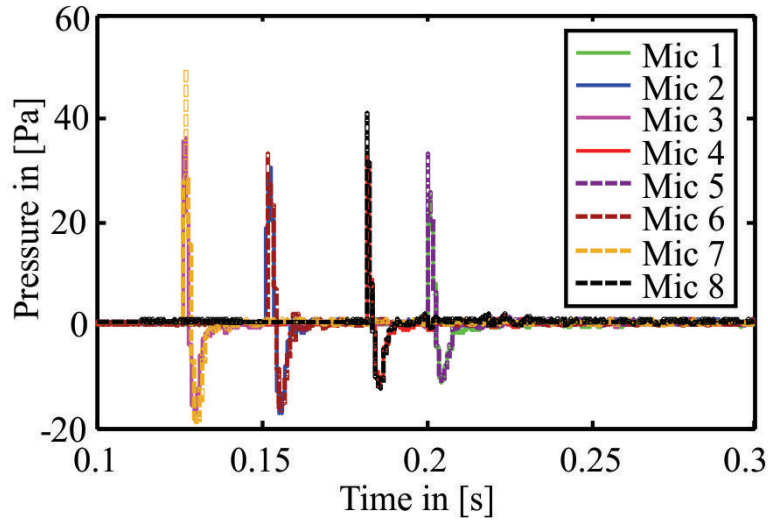


Fig. 8. Responses obtained from eight microphones

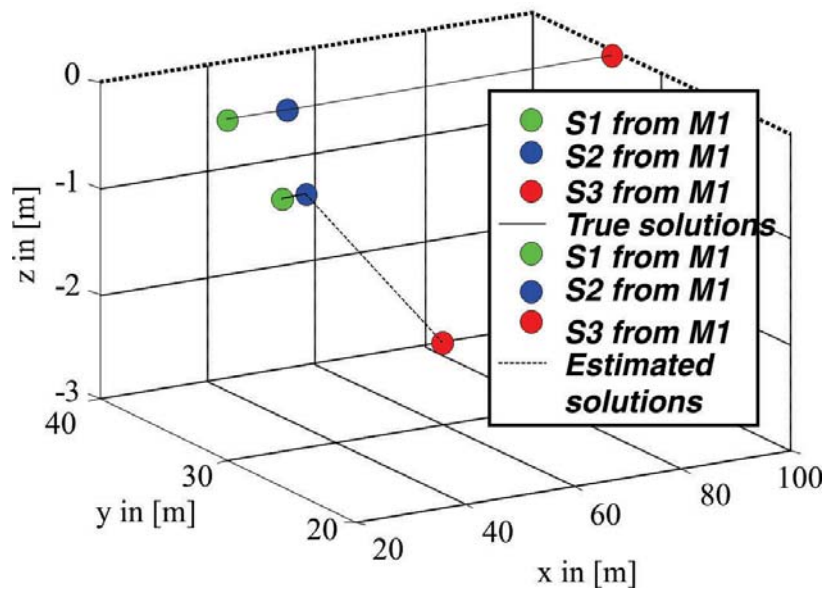


Fig. 9. True and Estimated source locations

satisfactory result when the source lies within the range of magnitude of microphone spacing. When the source range increases as compared to the altitude of the microphone from the ground, due to meteorological conditions, the effect of sound propagation in the air was affected, which results in the poor estimation of source coordinates measurement.

5. CONCLUSIONS

Localization of the sound source in a reverberant indoor and free field outdoor environment is carried out by using positioning algorithms through the use of estimated time delays. This paper mainly focuses on CC and GCC based functions to estimate the TDOA. From the comparison study among CC and GCC, it is concluded that, at the low sampling frequency, GCC based Prefilter such as PHAT produces more

sharp cross-correlation peaks inside a reverberant indoor space that leads to more precise and robust source localization. Since the algorithms are highly dependent on estimated path difference measurements, the solution is more sensitive towards the error in TDOA measurements and estimated sound speed in the air, which has a significant influence on 2D and 3D source positioning algorithms. Moreover, due to reflection from the boundary and floor, terrain condition, microphone position, a significant difference in source range and altitude of microphones from the ground, localization accuracy is expected to be degraded. Therefore, the perfect solution won't be possible in the real environment.

6. REFERENCES

- [1] C. Knapp and G. Carter, 1976. The generalized correlation method for estimation of time delay, *IEEE transactions on acoustics, speech, and signal processing*, **24**(4), 320-327.
- [2] M. Azaria and D. Hertz, 1984. Time delay estimation by generalized cross correlation methods, *IEEE Transactions on Acoustics, Speech, and Signal Processing*, **32**(2), 280-285.
- [3] N.M. Kwok, J. Buchholz, G. Fang and J. Gal, 2005. Sound source localization: microphone array design and evolutionary estimation, *IEEE International Conference on Industrial Technology*, pp. 281-286.
- [4] G.C. Carter, 1981. Time delay estimation for passive sonar signal processing, *IEEE Transactions on Acoustics, Speech, and Signal Processing*, **29**(3), 463-470.
- [5] Q. Zou and Z. Lin, 2002. Measurement time requirement for generalized cross-correlation based time-delay estimation, *IEEE International Symposium on Circuits and Systems. Proceedings (Cat. No. 02CH37353)*, **3**, III-III.
- [6] B. Kwon, Y. Park and Y.S. Park, 2010. Analysis of the GCC-PHAT technique for multiple sources, *ICCAS*, pp. 2070-2073.
- [7] J. Chen, Y. Huang and J. Benesty, 2005. A comparative study on time delay estimation in reverberant and noisy environments, *IEEE Workshop on Applications of Signal Processing to Audio and Acoustics*, pp. 21-24.
- [8] M. Jian, A.C. Kot and M.H. Er, 1998. Performance study of time delay estimation in a room environment [microphone arrays], In *ISCAS'98, Proceedings of the 1998 IEEE International Symposium on Circuits and Systems (Cat. No. 98CH36187)*, **5**, 554-557.
- [9] B.M.R. Bharathi and A.R. Mohanty, 2018. Underwater Sound Source Localization by EMD-Based Maximum Likelihood Method, *Acoustics Australia*, **46**(2), 193-203.
- [10] V. Sreeramamurthy, S. Dutta, S. Padhy and A. Bose, 2014. Determining Point of Burst of Artillery Shells using Acoustic Source Localization, *Defence Science Journal*, **64**(6), 517-523.
- [11] M. Imran, A. Hussain, N.M. Qazi and M. Sadiq, 2016. A methodology for sound source localization and tracking: Development of 3D microphone array for near-field and far-field applications, *13th International Bhurban Conference on Applied Sciences and Technology (IBCAST)*, pp. 586-591.
- [12] J. Tuma, P. Janecka, M. Vala and L. Richter, 2012. Sound source localization, In *Proceedings of the 13th International Carpathian Control Conference (ICCC)*, pp. 740-743.
- [13] T. Wang and Y. Choy, 2015. An approach for sound sources localization and characterization using array of microphones, *International Conference on Noise and Fluctuations (ICNF)*, pp. 1-4.
- [14] T.F. Embleton, 1996. Tutorial on sound propagation outdoors. *The Journal of the Acoustical Society of America*, **100**(1), 31-48.
- [15] Y. Huang, J. Benesty and G.W. Elko, 2000. Passive acoustic source localization for video camera steering, In *2000 IEEE international conference on acoustics, speech, and signal processing. Proceedings (Cat. No. 00CH37100)*, **2**, II909-II912.
- [16] Kinsler, E. Lawrence and Austin R. Frey, 1962. *Fundamentals of acoustics*, New York, Wiley.

A simplified model for predicting breakout noise from a rectangular duct

Yoganandh M.*, Nagaraja Jade and B. Venkatesham

*Department of Mechanical and Aerospace Engineering,
Indian Institute of Technology, Hyderabad, Telangana- 502285
e-mail: me16mtech11005@iith.ac.in*

[Received: 31-12-2019; Revised: 10-03-2020; Accepted: 17-03-2020]

ABSTRACT

In this paper, a simplified model is proposed to predict the breakout noise from a rectangular duct in terms of transverse transmission loss (TTL) using the modal radiation efficiency of a simple plate mode. Transverse transmission loss is the ratio of radiated sound power from the duct surface to the input power to the duct. Firstly, the radiated sound power from rectangular duct surface is predicted using two different models such as equivalent plate model (EPM) with total radiation efficiency and finite-length source model. The predicted TTL from the two sound power radiation models are in good agreement. However, EPM with total radiation efficiency model involves solving complex mathematical equations. Hence, a simplified model is proposed to predict total radiation efficiency of the duct using modal radiation efficiency of a simple plate mode. Major contributing mode for sound radiation in the duct is the breathing mode, i.e., dominant symmetric mode on duct's four walls. This mode is equivalent to (4, 1) mode of the simple plate. Modal radiation efficiency of the simple plate mode (4, 1) is used for TTL calculations. From this comparison study, it is observed that within the cut-on frequency, predicted results from the proposed simple model are in reasonable agreement with the literature data.

1. INTRODUCTION

Generally, rectangular ducts are largely used in air-handling units in which breakout noise is dominant at lower frequencies. Many research papers have been published on the study of breakout noise using wave based methods. Cummings^[1] developed a one-dimensional prediction model to calculate transverse transmission loss (TTL) of rectangular duct assuming common axial wave number in duct cavity and duct walls. Venkatesham *et al.*^[2] improvised the method by considering standing waves in finite duct length for different end terminal conditions.

Both, Cummings¹ and Venkatesham^[2] predicted the sound radiation from duct wall by assuming duct as a finite line source. Radiation efficiency of duct walls is predicted by an equivalent line source. Cummings^[1] developed an equivalent cylinder method to predict radiation efficiency. Venkatesham *et al.*^[3] developed an equivalent plate model (EPM) to predict total radiation efficiency and modal radiation efficiency of different modes. The mathematics involved in the EPM method is very complex. So, it motivate us to develop a simplified formulation to calculate the radiated sound power from rectangular duct.

In the present paper, transverse transmission loss (TTL) of rectangular duct is calculated using total radiation efficiency resulting from the EPM method. Then, TTL is calculated by using radiation efficiency of the breathing mode, being the major contributor to acoustic radiation. A simplified equation for modal radiation efficiency of a simple plate is used to predict total radiation efficiency. The results obtained are used to predict TTL. All these results are compared to the finite-length line source model available in the literature.

2. METHODOLOGY

2.1 Finite-length line source model

Transverse transmission loss of the rectangular duct is defined as^[1],

$$TTL = 10 \log \left(\frac{W_{in}}{W_{rad}} \right) \quad (1)$$

where, W_{in} is incident power on duct walls, W_{rad} is radiated power from duct walls. Radiated power W_{rad} is a function of radiation efficiency of the duct. Venkatesham *et al.*^[2] defined radiated power as,

$$W_{rad} = \frac{C_r \omega \rho_e (|C|^2 + |D|^2)}{8} \quad (2)$$

where, C_r is radiation factor, ω is circular frequency and ρ_e is density of external medium. The volume velocity is calculated by integrating the normal surface velocity amplitude around the duct walls and it may be expressed in terms of the wall admittance. C and D represent amplitude of forward and reflected wave volume velocity. The detail expressions and description of terms C and D is given by Venkatesham *et al.*^[2]. C_r was calculated by assuming that duct radiates similar to finite-length source.

2.2 Equivalent plate model (EPM)

Venkatesham *et al.*^[3] developed an equivalent plate analytical model(EPM), to predict sound radiation characteristics like total radiated sound power level, modal radiation efficiency, and directivity of radiated sound from duct walls. In this model, an unfolded equivalent plate representation is used to model the rectangular duct. Figure 1 shows equivalent plate representation of a rectangular duct. The rectangular duct is unfolded as an equivalent plate where folded joint is modelled as rotational spring (K_r), and adjacent wall joints are modelled as linear springs (K_l). A simply supported (S-S) boundary condition is applied to equivalent plate boundaries along the axial direction. Dimensions of the plate are $L_c \times L_a$, where, $L_c = 2(L_2 + L_3)$ is the perimeter of cross-section and L_a is length of duct, respectively.

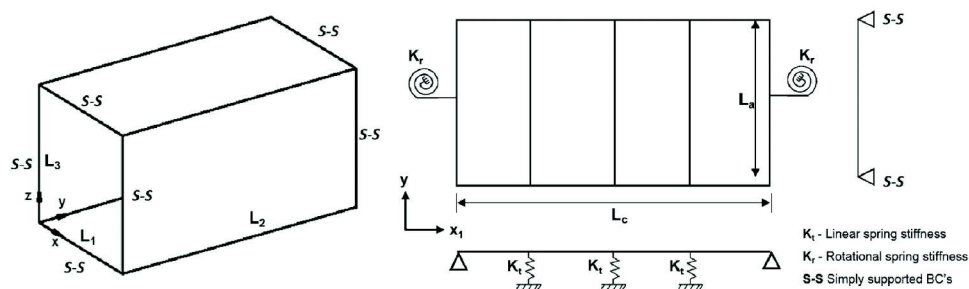


Fig. 1. Equivalent plate representation of rectangular duct

Radiation efficiency of a rectangular plate is defined as^[4],

$$\sigma = \frac{W_{rad}}{W_{in}} \quad (3)$$

A simplified model for predicting breakout noise from a rectangular duct

$$W_{in} = \rho_0 c_0 S \langle v^2 \rangle \quad (4)$$

where, ρ_0 and c_0 are density and speed of sound in that medium. W_{in} is plane wave sound radiation power by a piston source having surface area similar to duct structure and vibrating with same root mean square velocity as the structure $\langle v^2 \rangle$

In the EPM method, W_{rad} is calculated by equivalent plate representation and is explained in detail by Venkatesham *et al.*[3]. The expression for W_{rad} is given by,

$$W_{rad} = \sigma \times \rho_0 c_0 S \langle v^2 \rangle \quad (5)$$

From Eqs. (2) and (5), the radiation factor (C_r) and radiation efficiency (σ) are related as,

$$C_r = \frac{8\sigma c_0}{\omega S L_a} \quad (6)$$

Here, S is an equivalent plate area ($L_c \times L_a$).

Praveena *et al.*[4] showed that amongst all modes of the duct, breathing mode is the major contributor of total radiation efficiency. At the breathing mode, all duct walls vibrate out of plane with same phase as shown in Fig. 2.

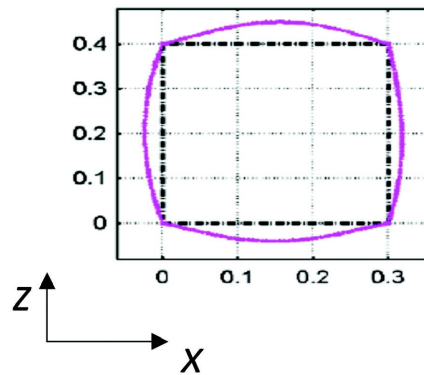


Fig. 2. Breathing mode of a rectangular duct

2.3 Simple plate model

Calculation of radiation efficiency using EPM method involves solving quadruple integrals, which requires time consuming computational work. Thus, a simplified model is required to reduce the complexity. As mentioned earlier, breathing mode of the duct is a major contributor to radiation efficiency. In the simple plate model, breathing mode of the duct is assumed to be represented as (4, 1) mode of rectangular plate as shown in Fig. 3.

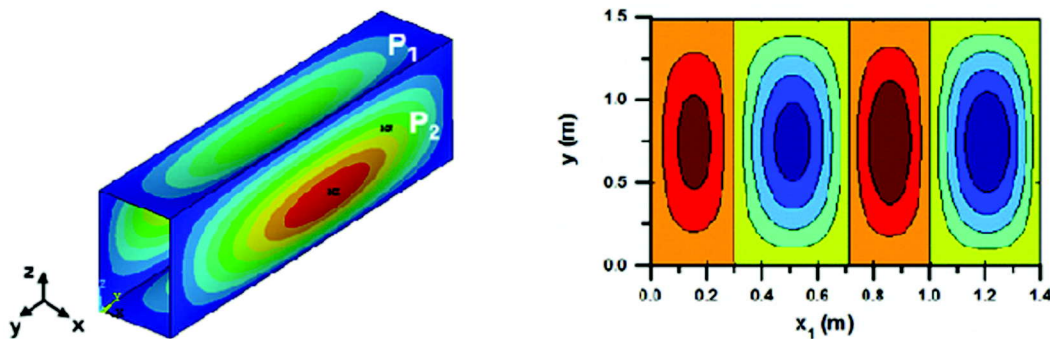


Fig. 3. Breathing mode of duct is visualized as (4, 1) mode of the plate

Modal radiation efficiency (σ_{mn}) of rectangular plate is calculated using equation of Wallace^[5].

$$\sigma_{mn} = \left(\frac{64k^2 L_c L_a}{\pi^6 m^2 n^2} \right) \times \int_0^{\pi/2} \int_0^{\pi/2} \left[\frac{cs(\alpha/2)cs(\beta/2)}{[(\alpha/m\pi)^2 - 1][(\beta/n\pi)^2 - 1]} \right]^2 \times \sin\theta d\theta d\phi, \quad (7)$$

where, $cs(\alpha/2) = \cos(\alpha/2)$ when m is odd and $cs(\alpha/2) = \sin(\alpha/2)$ when m is even.

Similarly, $cs(\beta/2) = \cos(\beta/2)$ when n is odd and $cs(\beta/2) = \sin(\beta/2)$ when n is even.

$$\alpha = kL_c \sin\theta \cos\phi \quad (8)$$

$$\beta = kL_a \sin\theta \sin\phi \quad (9)$$

where, L_c and L_a are dimensions of rectangular plate, k is wave number of acoustic media, m, n are mode numbers and θ, ϕ are the vertical and horizontal co-ordinate angles for the acoustic pressure measurement position in the far-field.

3. DUCT MODEL

Transverse transmission loss (TTL) from rectangular duct is calculated using three different methods as explained in Section-2. The model chosen for calculation is an unlined rectangular duct of cross section $0.3 \text{ m} \times 0.4 \text{ m}$, and length being 1.5 m . It is open at both ends of the cross sections as shown in the Fig. 4.

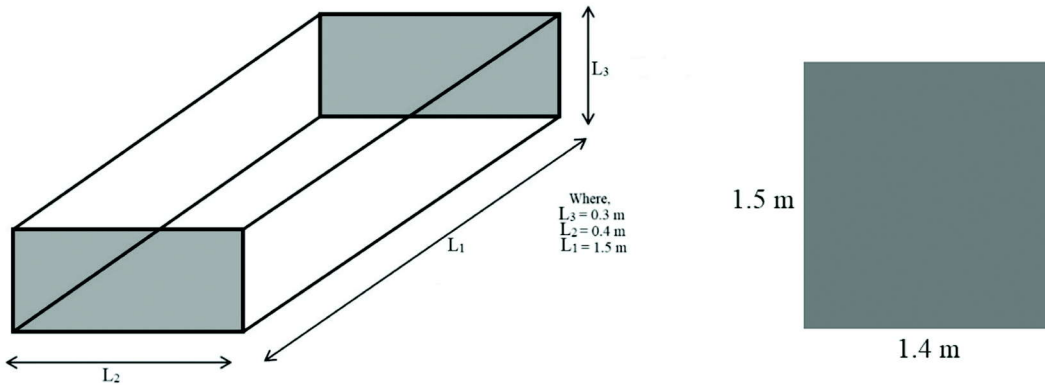


Fig. 4. Rectangular duct and its equivalent plate dimensions

The duct wall panels are constructed using aluminium material having modulus of elasticity $E = 71 \text{ GPa}$, Poisson's ratio $\mu = 0.33$, and density $\rho = 2700 \text{ kg/m}^3$. Thickness of duct wall panel, h , is 5 mm . From Section 2.2, dimensions of the plate used for equivalent plate method and simple plate method are $1.4 \text{ m} \times 1.5 \text{ m}$. 1.4 m is circumference of duct cross-section and 1.5 m is length of the duct.

W_{rad} is calculated by determining radiation factor (C_r) from given three methods. From W_{rad} , TTL is eventually calculated. C_r is calculated from radiation efficiency (σ) of the plate using Eq. (6).

4. RESULTS AND DISCUSSIONS

Transverse transmission loss calculated by EPM method using total radiation efficiency of duct and modal radiation efficiency of breathing mode are compared to TTL values obtained from finite-length line source model. It is observed from Fig. 5, up to cut-on frequency (f_{co}), values obtained using finite-length line source model are in good agreement with EPM method.

Cut-on frequency of the rectangular duct is defined as frequency where, the higher order mode transmission starts. It is calculated by expression^[6],

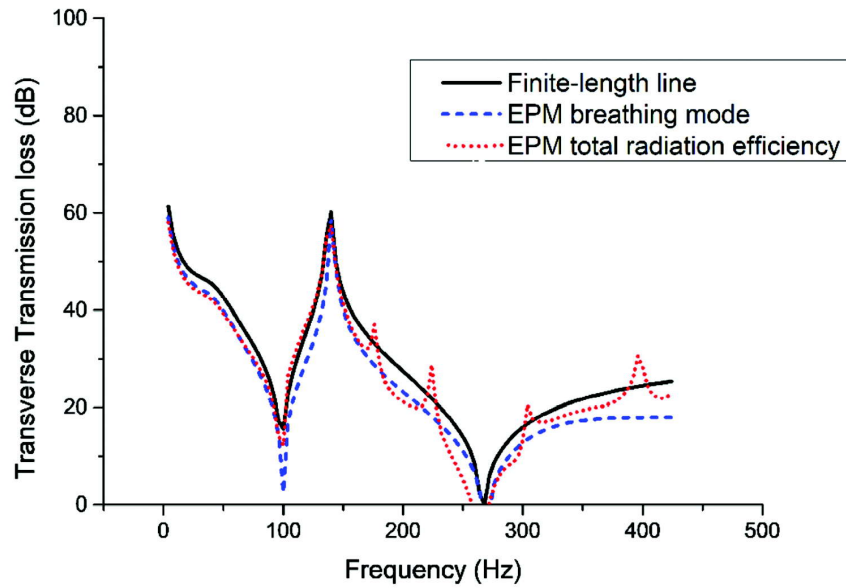


Fig. 5. Comparison of the TTL values calculated by EPM method with Finite-length line source

$$f_{co} = \frac{0.5 * c_0}{\max(L_2, L_3)} \text{ Hz} \quad (10)$$

Where, c_0 is speed of sound in propagating medium. The model used to calculate transverse transmission loss doesn't include higher order mode transmission and works only up to cut-on frequency (f_{co}). For the chosen duct dimensions, cut-on frequency is 425 Hz.

Using simple plate model with dominant breathing mode radiation efficiency, transverse transmission loss is calculated, and results are compared to values obtained from finite-length line source model. Both these results are in reasonable agreement.

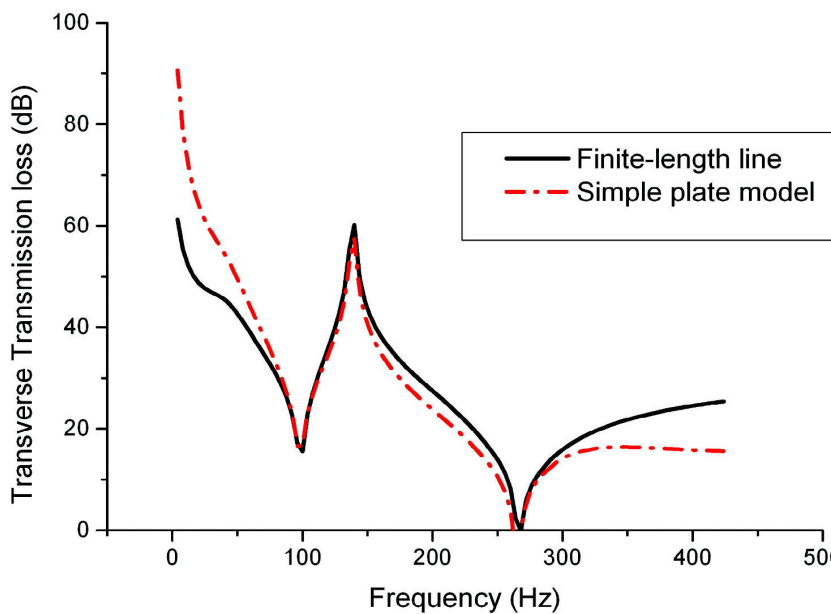


Fig. 6. Comparison of the TTL values calculated by simple plate model with finite-length line source

In Fig. 6, comparison is performed up to f_{co} . It can be observed that at lower frequencies, TTL values are over predicted as radiation efficiency (σ) obtained is under-predicted. From engineering point of view, maximum interest is towards the trough (in the graph), i.e. minimum values of TTL, where the predicted results are in good agreement.

5. CONCLUSION

Transverse transmission loss (TTL) of rectangular duct is predicted using total radiation efficiency calculated by equivalent plate method (EPM). A simple model is proposed to calculate TTL based on modal radiation efficiency of plate mode (4, 1) which is equivalent to dominant breathing mode of the duct. Transverse transmission loss results obtained from both the models are compared with finite-length source model, and all three models are in good agreement. From the comparison study, it is observed that within cut-on frequency, predicted results from the proposed model are in reasonable agreement with literature data.

6. REFERENCES

- [1] A. Cummings, 1978. Low frequency acoustic transmission through the walls of rectangular ducts, *Journal of Sound and Vibration*, **61**, 27-45.
- [2] B. Venkatesham, G.P. Ardhendu and M.L. Munjal, 2007. A One-dimensional Model for Prediction of Breakout Noise from a Finite Rectangular Duct with different Acoustic Boundary Conditions, *International Journal of Acoustics and Vibrations*, **12**, 91-98.
- [3] B. Venkatesham, Mayank Tiwari and M.L. Munjal, 2011. Prediction of Breakout Noise from a Rectangular Duct with Compliant Walls, *International Journal of Acoustics and Vibration*, **16**(4), 180-190.
- [4] R. Praveena, Jade Nagaraja and B. Venkatesham, 2016. Sound Radiation Characteristics of a Rectangular duct with Flexible Walls, *Advances in Acoustics and Vibrations*, pp. 1-15.
- [5] C. Wallace, 1972. Radiation resistance of a rectangular panel, *Journal of the Acoustical Society of America*, **51**, 946-952.
- [6] M.L. Munjal, 1987. *Acoustics of Ducts and Mufflers*, John Wiley & Sons, New York.

Structure Borne Noise — Structural excitation by turbo charger while noise radiation by vehicle components

Bhushan Singh Gautam*

Department of Mechanical Engineering

School of Studies, Guru Ghasidas Central University, Koni, Bilaspur (C.G)

e-mail: bhushan.gautam@ggu.ac.in

[Received: 30-10-2019; Revised: 06-03-2020; Accepted: 17-03-2020]

ABSTRACT

This article presents a discussion on the behavior and visualization of structural vibration transfer and structure borne noise in an automotive turbocharger. Structural vibrations are generated in a turbocharger due to various rotor modes and imbalance present in rotating assembly (rotor-bearing system) which are further transferred to vehicle components through different transfer paths. Along the vibration transfer path, this excitation may be radiated as noise by some sensitive vehicle components in specific frequency ranges. This behavior is captured and analyzed using acoustic source localization techniques by means of a commercially available tool that implements beam forming technique and acoustic holography.

1. INTRODUCTION

Over the years, automobiles have undergone a great extent of refinement in pursuit of improved design, higher fuel efficiency, lower emissions and increased user comfort. From the perspectives of user comfort and government regulations, reduced noise emissions and improved interior acoustics in vehicles have become a priority as original equipment manufacturers (OEMs) and component suppliers have made great strides in providing products with reduced vibro-acoustic response.

Turbocharging has become increasingly common in all categories of automobiles to achieve downsizing of engines, increase in power rating, improvement of fuel efficiency and reduction in emissions. However, a turbocharger is also a source of considerable vibro-acoustic excitation and can potentially emit high frequency noise and cause other vehicle components to radiate high frequency noise. In the early days of turbocharging, particularly in passenger vehicles, sound from turbocharger was desirable, as it helped to distinguish a more powerful turbocharged engine from a similar, naturally aspirated version. However, as turbocharging has become more common, sound due to turbocharging considered as undesirable (noise), resulting in an annoyance to passengers within the vehicle and external observer. *'Indeed, a great example of definition of noise, it all depends on perception'*. The frequency content of several types of turbocharger noise is often in a range in which the human ear is very sensitive (1000-6000 Hz). Hence, increased efforts

*Earlier with Garrett Motion Engineering Solutions Pvt. Ltd., Bangalore

have been made to not only improve vibro-acoustic behavior of turbochargers but also to design vehicles that are less sensitive to turbocharger excitation, both structural and aerodynamic.

2. TURBOCHARGER NOISE

Noises resulting from the turbocharger are of different types. While some of them are due to structural excitation of turbocharger and connected components on the vehicle, others are aerodynamically generated by various flow behaviours in the turbocharger. Figure 1 illustrates a typical turbocharger system and the types of noise and vibrations associated with it.

Structurally radiated noise due to unbalance of the turbo rotor-bearing group is the most commonly encountered noise type. These noises are affected by the type and geometry of the rotor-bearing system, extent of unbalance, and lubricant properties. Two common varieties of this kind are as follows:

- **Turbo whine** - Also referred to as synchronous noise, in reference to its frequency being equal to the rotational speed of the turbocharger. This noise originates from a once-per-revolution excitation owing to the system imbalance
- **Howling** - Also referred to as sub-synchronous, in reference to its frequency content being lower than the rotational frequency of the turbocharger. This excitation is caused by the phenomena of oil whirl and oil whip.

Aerodynamically generated noises are the second most commonly occurring noise related to turbochargers. Commonly encountered aero noises include the following:

- **Hiss** - broadband noise due to turbulent flow and efficiency drop in the compressors.
- **Kreischen** - High amplitude, narrowband noise in compressors, occurring close to surge due to impeller rotating stall.
- **Blade passing noise** - tonal noise occurring at blade passing frequency (rotating speed * number of blades on the wheel) in compressor and turbine wheels due to periodic disturbance in the flow caused by passing of blades.
- **Pulsation** - Whining noise occurring at turbo rotating frequency due to asymmetry in the compressor wheel, resulting in once-per-revolution disturbance in flow.
- Other aero noises such as harmonics, cavity resonances in recirculation valve, side branch noise, etc

In the present article, the focus is on Turbo whine noise in vehicles.

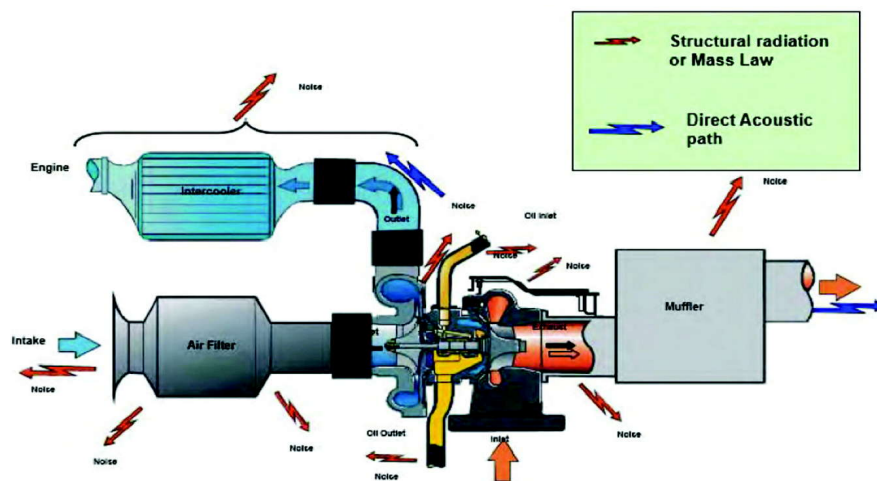


Fig. 1. Schematic of a turbocharger connected to air-intake, outlet and exhaust system, indicating common vibroacoustic sources, transfer paths and radiating surfaces

3. TURBO WHINE NOISE - SOURCE AND MECHANISM

Turbo whine also referred as synchronous noise is mainly due to the presence of unbalance in the Rotating Assembly (RA). RA consists of Turbine wheel (TW) + Shaft + Compressor wheel (CW).

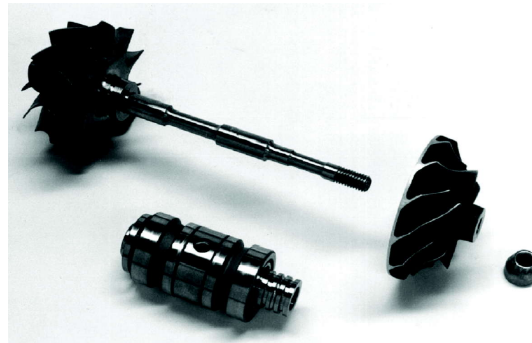


Fig. 2. Image of Rotating Assembly

Unbalance - Unbalance in the system arises when the center of mass doesn't coincide with the geometric center, which -actually lies on the axis of rotation. Unbalance in the system is characteristic of rotating system 'in real world ' due to manufacturing limitation. It could occur in any stage of manufacturing, starting from casting/forming/machining of shaft to assembly of TW/CW on shaft.

As RA has axial length, unbalance is not on single plane, but it exists on multiple planes. Also as turbo runs at high speeds (upto 300,000 rpm), shafts are no longer rigid hence makes it more complex to eliminate the unbalance completely.

During mass production RA are balanced to keep the unbalance in limit and not for perfect balancing (zero unbalance) of the RA. Moreover, lower unbalance improves/amplifies the natural modes of the shaft of RA.

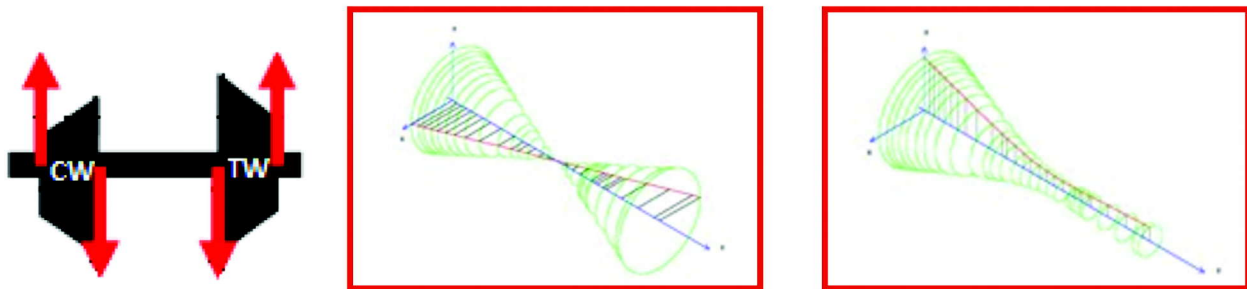


Fig. 3. Schematic of Unbalance in rotating assembly and Bending modes

Synchronous Vibration - Generation, Transfer and Noise Radiation : Excitation force due to unbalance excites the system once-per-revolution. So the frequency of excitation force would always be same as turbo speed and hence the vibration caused due to unbalance is also referred as synchronous vibration.

While synchronous vibration travels through the vehicle system and passes through various vehicle component, in case any component achieves enough surface velocity on account of low stiffness (or other possible reasons), that it starts transferring structural vibration energy to surrounding medium (air in this case) through the surface. We know that disturbance in the air is observed as 'SOUND' and the phenomenon of transferring vibration energy of the structure to the air is termed as noise radiation.

Resonance of components could also be the reason of noise radiation. Referring resonance phenomenon, every component has natural frequencies, while synchronous vibration travels through the vehicle system & in case the frequency of synchronous vibration matches with natural/modal frequency of any component on the transfer path, vibration amplitude intensifies on the component and once the component achieves enough surface velocity to transfer vibrational energy to the air, one could start hearing the noise radiated through the surface.

Synchronous noise which is tonal in nature can be distributed over a large frequency range, typically in the turbo speed range 800 -5000 Hz. Several parameters which potentially influence the presence and extent of synchronous noise:

- **Unbalance in rotating assembly** : High speed balancers are used to control the unbalance present in the RBS. However perfect balancing is not possible in mass production due to manufacturability and cost.
- **Transmissibility of unbalance from rotating assembly to Housing (via. bearing)** : This is taken care during design of bearing by controlling pad lengths and clearances.
- **Isolating vehicle components from turbo synchronous vibration** : Components having large and low stiffed surface area are recommended to kept isolated from the vibration transfer path.

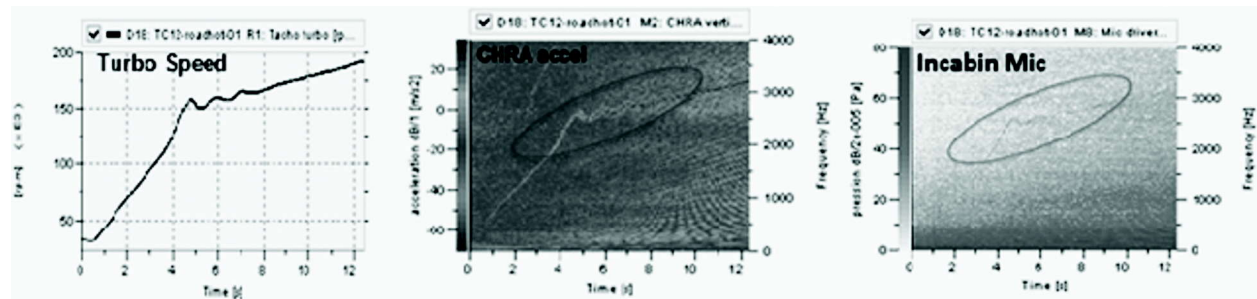


Fig. 4. TC speed profile, Synchronous vibration measured on turbo charger and synchronous noise in the driver illustrating frequency content of synchronous vibration/noise

4. SOUND SOURCE LOCALIZATION TECHNIQUES

Finding out the exact source of a sound is a tough challenge for any acoustics engineer. Beam forming technique uses arrays of microphone arranged in a specific way to locate the Noise source. The acoustic beamforming technique was first developed for submarines and environmental applications. In the far field, sound waves hitting the array are planar waves. Under these conditions, it is possible to propagate the measured sound field directly to the test object. All microphone signals measured by the acoustic beamforming array are added together, taking into account the delay corresponding to the propagation distance. The pressure can be calculated at any point in front of the array, allowing propagation to any kind of surface. Acoustic beamforming is sometimes called "sum and delay" since it considers the relative delay of sound waves reaching different microphone positions. Acoustic beamforming requires that all data is measured simultaneously in the far field.

The main disadvantage is that acoustic beamforming does not perform well in the low frequency range and it is suitable only for far field measurement. Over the years, we have more matured process 'Near-field focalization' which basically is a beamforming technique that uses measurements in the near field, whereas classical acoustic beamforming is measured in the far field. In the near field, the sound waves no longer arrive at the microphone as planar waves, but as spherical waves. The original beamforming back propagation is reformulated to deal with these waves.

The array consists of camera as well to overlap the estimated location of noise source with the actual image. There are many commercially available tools which uses beam forming technique for Noise source localization.

5. TEST SETUP AND MEASUREMENT

Test setup & measurement are done considering below points:

- Understand the layout clearly, the vibration source and the possible transfer paths.
- Feasible several camera positions so that it would cover all possible noise radiating components.
- Carry out measurement in suitable test cycles (% load and engine speed combination) such that noise of interest (synchronous noise, in this case) is clearly audible and stands out over the background noise (engine noise). Make sure to cover the full operating frequency range of noise of interest.

For the present study, to cover the wide operating speed of turbo, engine was run in following conditions:

- Test Condition 1: 25% Load, 900-1500 engine rpm: To capture noise in the range 1000-1500 Hz.
- Test Condition 2: 25% Load, 1500-4000 engine rpm: To capture noise in the range 1800-3200 Hz.

A single camera position has been used to capture the possible noise radiators. However, below configurations have been studied to exposed the covered surfaces and locate the actual noise radiator:

- Configuration 1: With all Heat shields.
- Configuration 2: Without Turbo Heatshield
- Configuration 3: Without Elbow Heatshield.
- Configuration 4: Without Cat-con Heatshield.
- Configuration 5: No Heat Shield.

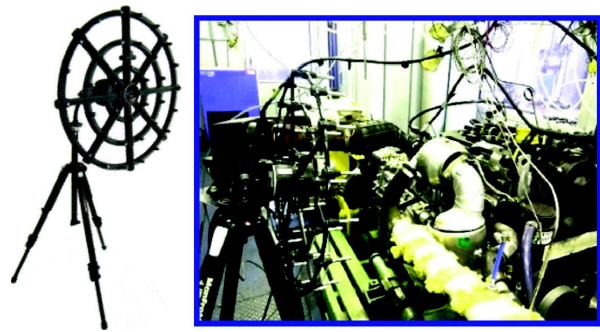


Fig. 5. Sound source localization hardware (Microphone array + camera at the center)

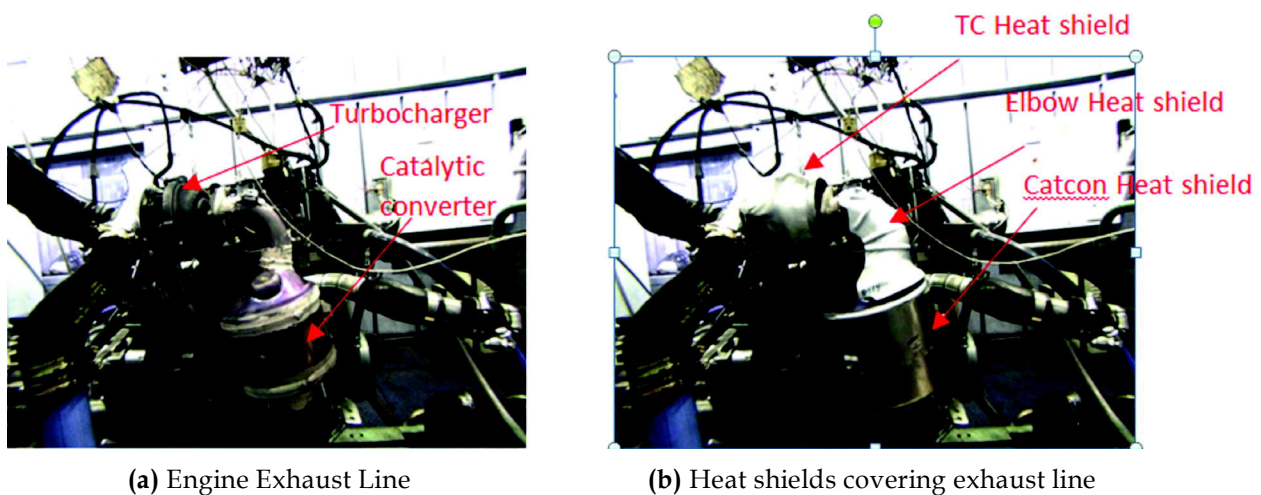


Fig. 6. Possible noise radiators for turbocharger vibration

6. RESULTS AND VALIDATION

The Frequency ranges chosen for study, are based on observed audible noise from the vehicle level measurement, which are 1300-1400 Hz, 2000-2500 Hz and 3000-3500 Hz.

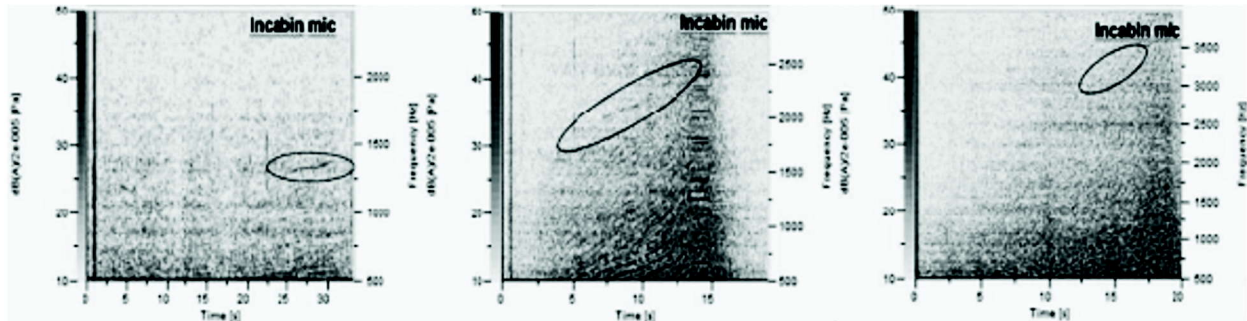


Fig. 7. Noise occurred at different driving condition

Result : In this study, as explained earlier, turbocharger is the source of vibration, but the noise radiator are various vehicle components, which is captured perfectly by the sound source localization technique. Refer images in Figure 8.

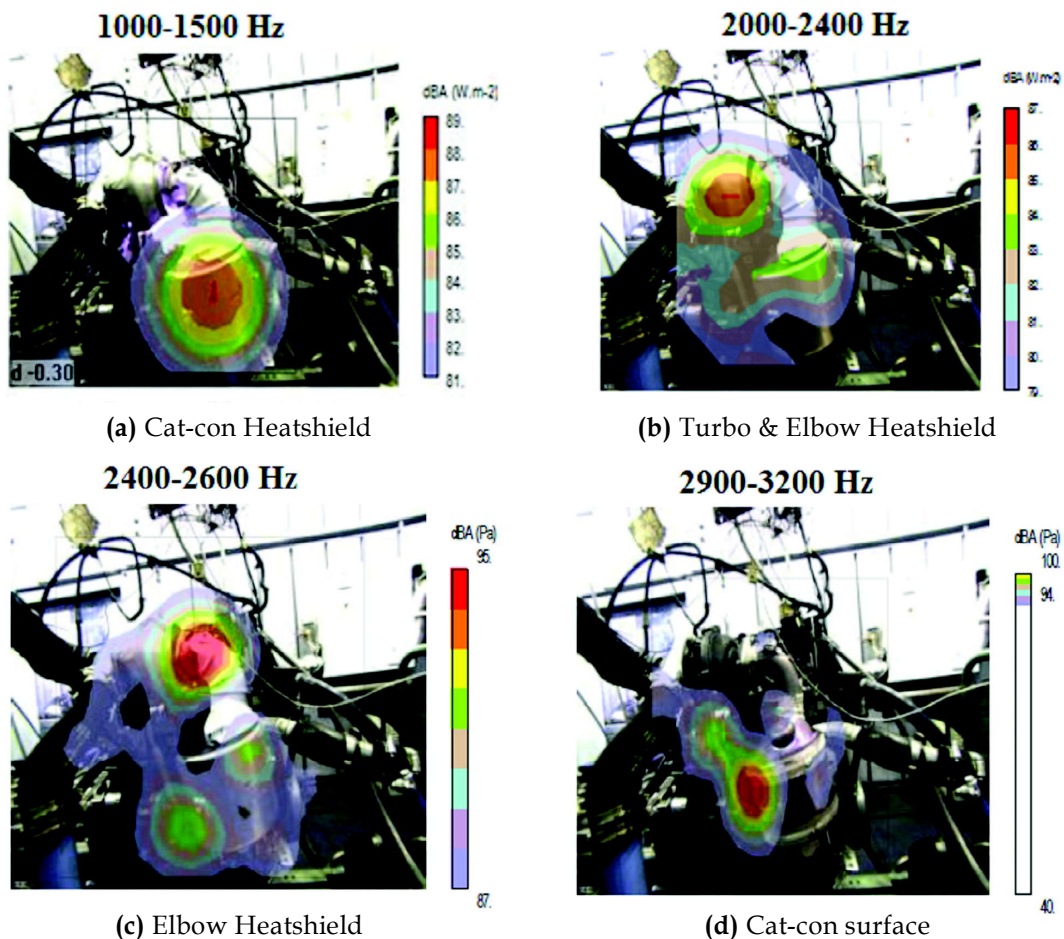


Fig. 8. (a) to (d) shows noise radiator for TC synchronous vibration for different frequency range

Validation : To validate the noise radiators captured using sound source localization technique, similar measurements have been carried out for configurations 1-5 (mentioned in section 5) and noise level has been compared to verify the noise radiator.

Validation for 1000-1500 Hz Noise Range : For validation of noise source in the range 1000-1500 Hz, the engine is run at Test Condition 1, and the synchronous noise level extracted and compared for configurations 1-5. Referring Figure 9, there is significant decrease of 6 dB in the sound level with the removal of Cat-con Heatshield, which is the primary noise radiator.

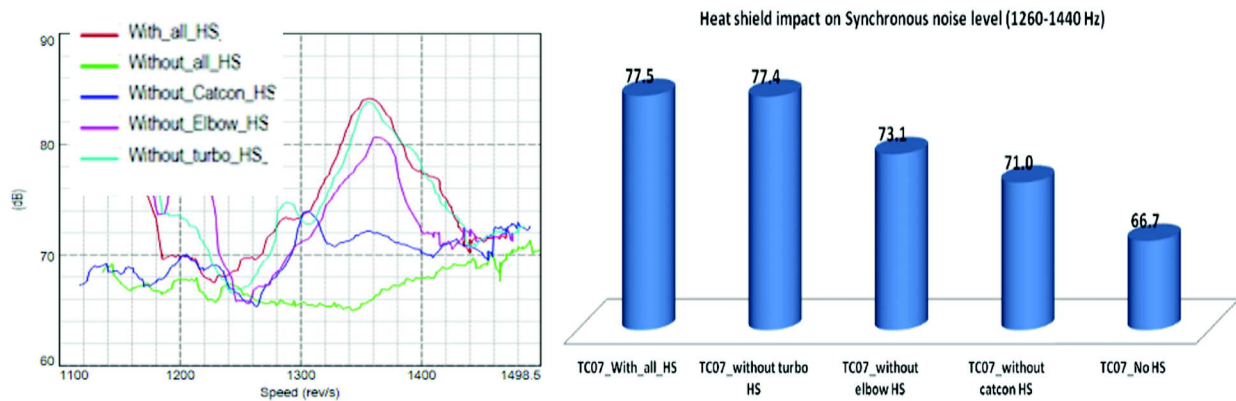


Fig. 9. (a), (b) Noise level comparison with different configuration

Also, sound source localization shows the noise disappears with the removal of Cat-con Heatshield, refer Figure. 10.

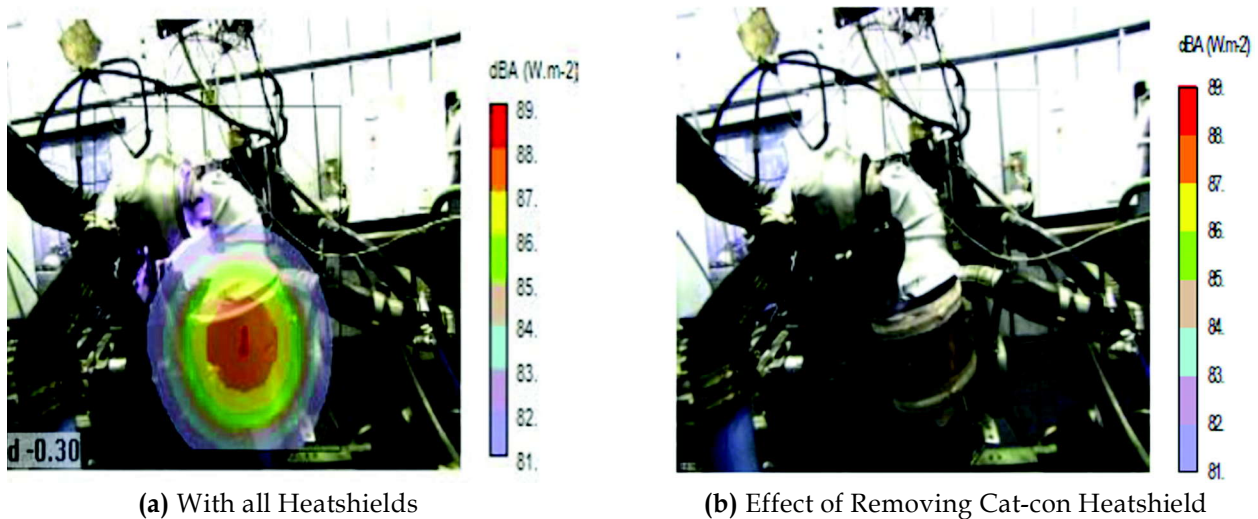


Fig. 10. Source localization measurement before and after removal of Noise Radiator

Validation for Noise Range > 1800 Hz : For validation of noise source in the range >1800 Hz, the engine is run at Test Condition 2, and the synchronous noise level extracted and compared for configurations 1-5.

Noise Range 2200-2400 Hz : Referring Figure. 11, in the zone 2200-2400 Hz, there is contribution from both Turbo Heat shield and Elbow Heat shield, and a decrease of 3 dB and 4 dB is observed, respectively, upon testing without these heat shields.

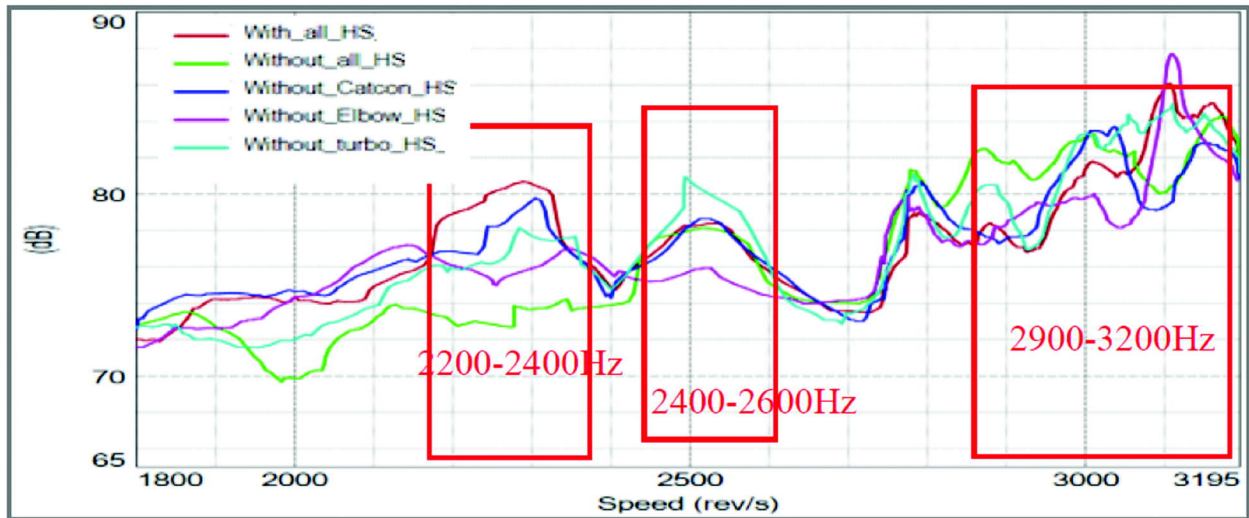
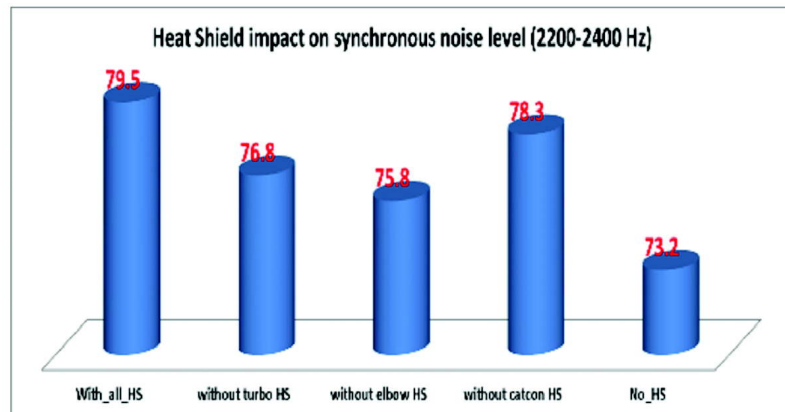


Fig. 11. Turbo Synchronous Noise Level

Also, the source localization technique (Figure 12) identifies the turbo-heatshield and elbow-heatshield as the noise radiators, and the effect of removal of these noise radiators can be seen in Figure. 12(c).



(a) Synchronous Noise Level 2200-2400 Hz

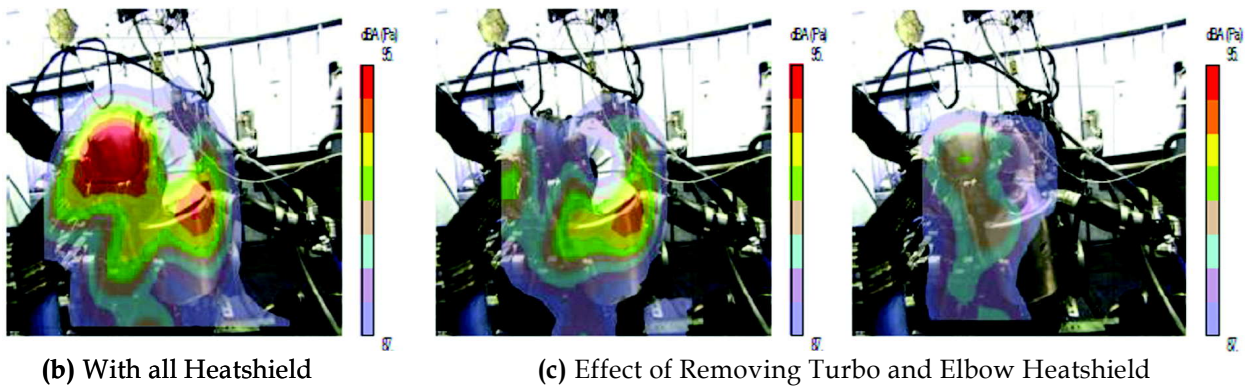
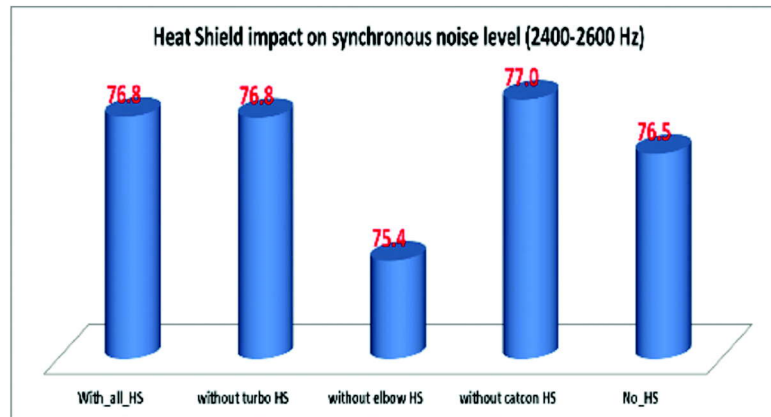
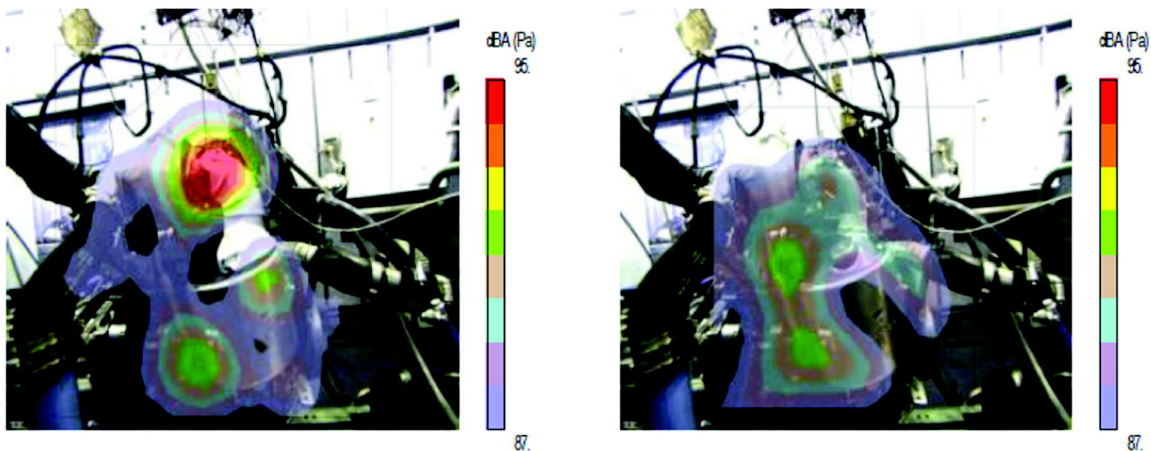


Fig. 12. Effect on synchronous noise level on removal of predicted noise radiator

Noise Range 2400-2600 Hz : Referring Figure. 13(a), contribution to noise by Elbow Heat shield can be seen. Sound source localization technique shows images in-line with the observation.



(a) Synchronous Noise level 2400-2600Hz.



(b) With all Heatshield

(c) Effect of Removing Elbow Heatshield

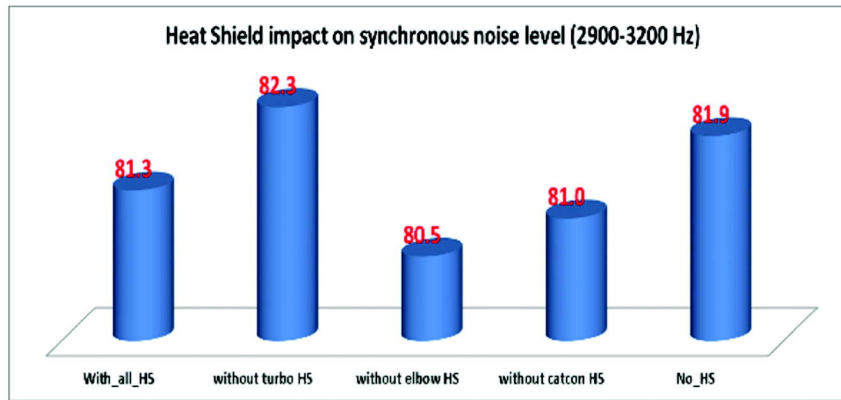
Fig. 13. Effect on synchronous noise level on removal of predicted noise radiator

Noise Range 2900-3200 Hz : Referring Figure 14 (a), Noise level doesn't vary much with the removal of heat shields. Indeed, a minor increase in noise level is observed after removal of heat shield.

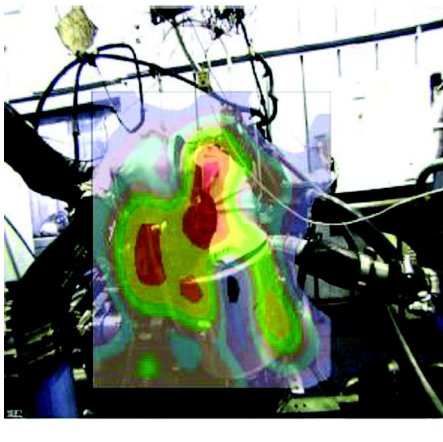
The sound source localization technique captures the phenomenon perfectly and identifies the cat-con surface as the noise radiator. The cat-con heat-shield acts as a noise barrier for the noise radiated by the cat-con surface, which also explains the reason for a little increase in sound level with the removal of heat shield.

Validation at Vehicle Level : Above observations have been validated by vehicle-level noise measurements. Figure.15 (a) and (b) show the effect of Heat shield on the noise present in the 1300-1500 Hz range. There is no trace of noise observed after the removal of heat shields.

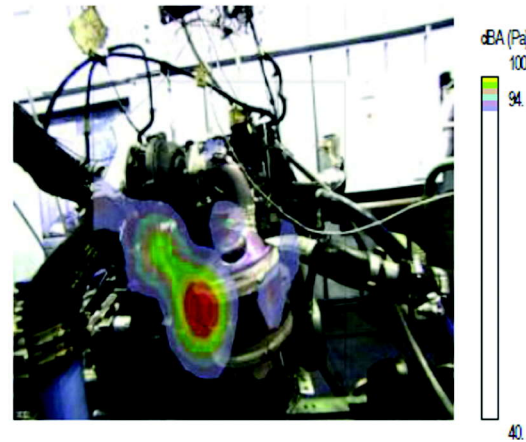
Referring to figure 15 (c) and (d), similar absence of noise trace till 2500 Hz can be noticed. However, noise traces above 3000 Hz can still be seen without heat shield, which is consistent with the earlier observation that noise in this frequency range is radiated by the Cat-con surface and not by the Heat shields.



(a) Synchronous noise level 2900-3200 Hz



(b) With all Heatshield



(c) Effect of Removing all Heatshield

Fig. 14. Effect on synchronous noise level on removal of predicted noise radiator

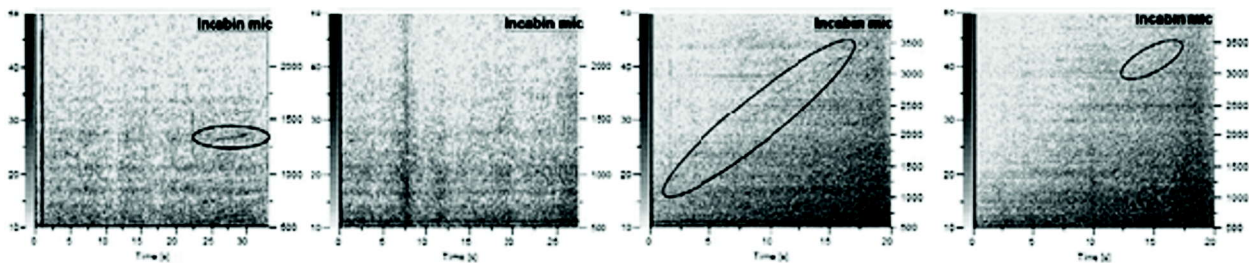


Fig. 15. Effect on synchronous noise level on removal of predicted noise radiator

7. CONCLUSION

The study visualizes noise radiations from various components, due to structural vibration transfer from a vibration source, using acoustic beam forming technique in near field.

While the source localization hardware helps in identifying the noise radiator for particular frequency range, the noise has been correlated with the vibration of turbocharger which has certain unbalance and

is rotating at its operating speed (~800-5000 rps). This has been explained by a case study of an automotive application where the turbocharger acts as a vibration source and different components along the exhaust system, are excited by this vibration transferred, thus resulting in audible noise radiation.

So, we could see many noise radiators resulting from a single source of vibration. A typical characteristic of 'Structure Borne Noise'.

8. REFERENCES

- [1] B.P. Hildebrand, 1981. Acoustic Holography: *Methods in Experimental Physics*, **19**, 533-562.
- [2] Sabih I. Hayek, Nearfield Acoustical Holography: Handbook of Signal Processing in Acoustics, *Narosa Publishing House*, p. 172.
- [3] Tshilidzi Mukwevho, Jaco Jordaan and Guillaume Noel, 2009. *Advanced beamforming techniques for acoustic source localization-* AFRICON.
- [4] Lewis H. Bell, 1994. 2nd Ed., *Industrial Noise control: Fundamentals and Applications*, New York MarcelDekker, Inc, ©1994.
- [5] Test Data and test setup images (figure 1, 4 & 5) from field testing & lab facility Garrett, Bangalore.

INFORMATION FOR AUTHORS

ARTICLES

The Journal of Acoustical Society of India (JASI) is a refereed publication published quarterly by the Acoustical Society of India (ASI). JASI includes refereed articles, technical notes, letters-to-the-editor, book review and announcements of general interest to readers.

Articles may be theoretical or experimental in nature. But those which combine theoretical and experimental approaches to solve acoustics problems are particularly welcome. Technical notes, letters-to-the-editor and announcements may also be submitted. Articles must not have been published previously in other engineering or scientific journals. Articles in the following are particularly encouraged: applied acoustics, acoustical materials, active noise & vibration control, bioacoustics, communication acoustics including speech, computational acoustics, electro-acoustics and audio engineering, environmental acoustics, musical acoustics, non-linear acoustics, noise, physical acoustics, physiological and psychological acoustics, quieter technologies, room and building acoustics, structural acoustics and vibration, ultrasonics, underwater acoustics.

Authors whose articles are accepted for publication must transfer copyright of their articles to the ASI. This transfer involves publication only and does not in any way alter the author's traditional right regarding his/her articles.

PREPARATION OF MANUSCRIPTS

All manuscripts are refereed by at least two referees and are reviewed by the Publication Committee (all editors) before acceptance. Manuscripts of articles and technical notes should be submitted for review electronically to the Chief Editor by e-mail or by express mail on a disc. JASI maintains a high standard in the reviewing process and only accept papers of high quality. On acceptance, revised articles of all authors should be submitted to the Chief Editor by e-mail or by express mail.

Text of the manuscript should be double-spaced on A4 size paper, subdivided by main headings-typed in upper and lower case flush centre, with one line of space above and below and sub-headings within a section-typed in upper and lower case understood, flush left, followed by a period. Sub-sub headings should be italic. Articles should be written so that readers in different fields of acoustics can understand them easily. Manuscripts are only published if not normally exceeding twenty double-spaced text pages. If figures and illustrations are included then normally they should be restricted to no more than twelve-fifteen.

The first page of manuscripts should include on separate lines, the title of article, the names, of authors, affiliations and mailing addresses of authors in upper and lower case. Do not include the author's title, position or degrees. Give an adequate post office address including pin or other postal code and the name of the city. An abstract of not more than 200 words should be included with each article. References should be numbered consecutively throughout the article with the number appearing as a superscript at the end of the sentence unless such placement causes ambiguity. The references should be grouped together, double spaced at the end of the article on a separate page. Footnotes are discouraged. Abbreviations and special terms must be defined if used.

EQUATIONS

Mathematical expressions should be typewritten as completely as possible. Equation should be numbered consecutively throughout the body of the article at the right hand margin in parentheses. Use letters and numbers for any equations in an appendix: Appendix A: (A1, (A2), etc. Equation numbers in the running text should be enclosed in parentheses, i.e., Eq. (1), Eqs. (1a) and (2a). Figures should be referred to as Fig. 1, Fig. 2, etc. Reference to table is in full: Table 1, Table 2, etc. Metric units should be used: the preferred form of metric unit is the System International (SI).

REFERENCES

The order and style of information differs slightly between periodical and book references and between published and unpublished references, depending on the available publication entries. A few examples are shown below.

Periodicals:

- [1] S.R. Pride and M.W. Haartsen, 1996. Electro seismic wave properties, *J. Acoust. Soc. Am.*, **100** (3), 1301-1315.
- [2] S.-H. Kim and I. Lee, 1996. Aeroelastic analysis of a flexible airfoil with free play non-linearity, *J. Sound Vib.*, **193** (4), 823-846.

Books:

- [1] E.S. Skudrzyk, 1968. *Simple and Complex Vibratory Systems*, the Pennsylvania State University Press, London.
- [2] E.H. Dowell, 1975. *Aeroelasticity of plates and shells*, Nordhoff, Leyden.

Others:

- [1] J.N. Yang and A. Akbarpour, 1987. Technical Report NCEER-87-0007, Instantaneous Optimal Control Law For Tall Buildings Under Seismic Excitations.

SUBMISSIONS

All materials from authors should be submitted in electronic form to the JASI Chief Editor: B. Chakraborty, CSIR - National Institute of Oceanography, Dona Paula, Goa-403 004, Tel: +91.832.2450.318, Fax: +91.832.2450.602, (e-mail: bishwajit@nio.org) For the item to be published in a given issue of a journal, the manuscript must reach the Chief Editor at least twelve week before the publication date.

SUBMISSION OF ACCEPTED MANUSCRIPT

On acceptance, revised articles should be submitted in electronic form to the JASI Chief Editor (bishwajit@nio.org)